U.PORTO

FEUP FACULDADE DE ENGENHARIA
UNIVERSIDADE DO PORTO

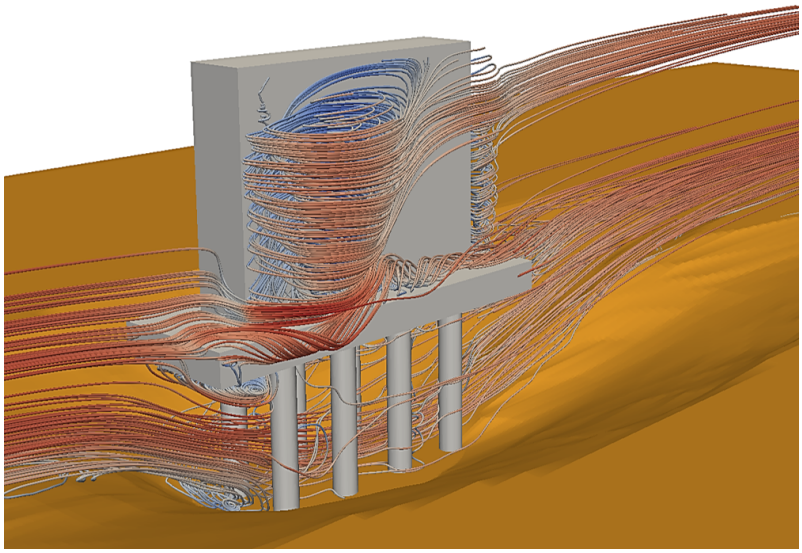

NUMERICAL SIMULATION OF THE FLOW BEHAVIOR AROUND BRIDGE PIERS

MAHDI ALEMI

Supervisor: Doctor Rodrigo Jorge Fonseca de Oliveira Maia

Co-Supervisor: Doctor João Pedro Gomes Moreira Pêgo

PORTO, 2018

Faculty of Engineering, University of Porto (FEUP)

NUMERICAL SIMULATION OF THE FLOW BEHAVIOR AROUND BRIDGE PIERS

MAHDI ALEMI

Dissertation submitted to Faculdade de Engenharia da Universidade do Porto to obtain the degree of

Doctor of Philosophy (Ph.D.) in Civil Engineering

President: Dr. Francisco de Almeida Taveira Pinto, University of Porto, Portugal

Referee: Dr. Michael Breuer, Helmut Schmidt University, Hamburg, Germany

Referee: Dr. Paulo Alexandre de Avilez Rodrigues de Almeida Valente, University of Porto, Portugal

Referee: Dr. Rui Miguel Lage Ferreira, Instituto Superior Técnico, Lisbon, Portugal

Referee: Dr. Fernando Francisco Machado Veloso Gomes, University of Porto, Portugal

Referee: Dr. Rodrigo Jorge Fonseca de Oliveira Maia, University of Porto, Portugal

---

PORTO, 2018

Abstract

Modern bridges are usually built over piers with complex geometries, although relatively few experimental studies exist on complex bridge piers. In fact, for a systematic and complete study, many experiments are required to be performed because of the variety in shape, size and configuration of the complex pier elements. In addition, the corresponding physical measurements are time-consuming and expensive. Nowadays, due to the availability of powerful computers, computational methods can be used to obtain further results at a lower cost compared to the use of physical models. Hence, this study was aimed to investigate computational methods and to develop a proper numerical model to predict the flow characteristics around bridge piers on a scoured bed in a simple, fast and accurate way.

The numerical model was developed in three main steps: finding solution algorithms for the flow equations set (continuity and Navier-Stokes equations), modeling of the turbulent flows and modeling of the complex geometries. The accuracy of the numerical model was evaluated in each step by comparing the corresponding numerical results with available reference data for different cases. Finally, the numerical model was applied to simulate the flow features around two different complex bridge piers on different stages of the scour hole development process.

The developed numerical model solves the space-filtered Navier-Stokes and continuity equations (LES Smagorinsky model) in the Cartesian grid system using a fractional-step method. In addition, a wall function was incorporated into the model that provides the approximate wall boundary conditions, helping to reduce the computational cost compared to the sole use of the LES model. Since the numerical model uses a Cartesian grid, the pier and bed geometries were described by means of a porosity technique (Fractional-Area-Volume-Obstacle-Representation method). The implicit equation for the pressure is solved with the successive over-relaxation method and the parallelization of the calculations is achieved by using the FORTRAN OpenMP library. Temporal discretization was performed by the second-order Adams-Bashforth scheme.

Concerning the spatial terms, the convection terms were approximated by the QUICK scheme (for the stability reasons) and all remaining spatial terms were approximated by the second-order central difference scheme. Overall, the numerical model is second-order accurate in both space and time.

The corresponding numerical results were found to be in good agreement with the ones obtained from the referenced bibliography. In addition, the numerical model enabled to characterize the most relevant flow features of the studied bridge pier cases. Overall, the obtained numerical results were most encouraging and further development of the numerical model was planned.

Keywords: Complex bridge piers; Scour hole; Large Eddy Simulation; Wall function; Turbulent flow

Resumo

As pontes modernas são, normalmente, construídas sobre pilares com geometrias complexas, embora existam poucos estudos relativos a pilares de pontes complexos. Na realidade, para um estudo sistemático e completo, é necessário realizar variados ensaios devido à diversidade em termos de forma, tamanho e configuração dos pilares. Além disso, as correspondentes medições em modelo físico são demoradas e caras. Atualmente, dada a disponibilidade de computadores potentes, os métodos computacionais podem ser considerados como alternativa para obter mais resultados a um custo menor, comparativamente com os modelos físicos. Como tal, o presente estudo foi estruturado no intuito de investigar métodos computacionais e desenvolver um modelo numérico capaz de prever as características de escoamento na zona adjacente a pilares de pontes, com leito erodido, de forma simples, rápida e precisa.

O modelo numérico foi desenvolvido em três passos principais: encontrar algoritmos para resolução do conjunto das equações de conservação consideradas (equações de continuidade e de Navier-Stokes), modelar escoamentos turbulentos e modelar geometrias complexas. A precisão do modelo numérico foi avaliada, em cada etapa, através da comparação entre os resultados numéricos correspondentes e os obtidos por bibliografia de referência, para diferentes casos. Por fim, o modelo numérico foi aplicado por forma a simular as características do escoamento em redor de dois pilares de ponte complexos e diferentes entre si, em fases diferentes do desenvolvimento temporal da cavidade de erosão.

O modelo numérico desenvolvido resolve as equações de continuidade e de Navier-Stokes filtradas no espacialmente (modelo LES Smagorinsky) no sistema de coordenadas Cartesianas, empregando um designado método de fractional-step. Além disso, foi incorporada uma função de parede nas soluções LES com o intuito de providenciar uma aproximação das condições-fronteira da parede, reduzindo o custo computacional, quando comparado com o uso isolado do LES. Como o modelo numérico usa uma malha Cartesiana, as geometrias dos pilares e do leito foram de-

scritos por intermédio de uma técnica de porosidade (método Fractional-Area-Volume-Obstacle-Representation). A equação implícita para a pressão foi resolvida através do método successive over-relaxation, com a paralelização dos cálculos a ser Obtida por intermédio da interface FORTRAN OpenMP. A discretização temporal foi realizada por um esquema Adams-Bashforth, de segunda ordem. Relativamente aos termos espaciais, os termos convectivos foram aproximados por um esquema QUICK (por razões de estabilidade) e os restantes termos espaciais foram aproximados pelo esquema da diferença central, de segunda ordem. Em geral, o modelo numérico tem uma precisão de segunda ordem, tanto em termos espaciais como temporais.

Por fim, os resultados numéricos correspondentes estão de acordo com os obtidos a partir das referências bibliográficas. Além disso, o modelo numérico permite a obtenção das características mais relevantes do escoamento junto aos pilares de ponte estudados. Em geral, os resultados numéricos obtidos foram bastante encorajadores e propostos desenvolvimentos futuros para o modelo numérico.

Palavras-Chave: Pilares de pontes complexos; Buraco de erosão; Large Eddy Simulation; Função de parede; Escoamento turbulento.

Acknowledgments

First and foremost, I am thankful to the Almighty God for holding my hands to complete this work.

I would like to thank my academic advisor, Doctor Rodrigo Maia. During my PhD study, he contributed to a rewarding experience by giving me intellectual freedom in my work, supporting me in every step of my work and demanding a high quality of work in all my endeavors. I also thank my academic co-advisor, Doctor João Pedro Pêgo, for all supports and fruitful suggestions.

I also would like to thank the various members of the Hydraulics, Water Resources and Environment Division (SHRHA) at FEUP, with whom I had the opportunity to work, especially Doctor Fernando Veloso Gomes and Doctor Paulo Avilez-Valente, as I greatly benefited from their keen scientific insight and knowledge. In addition, I am thankful to Doctor Francisco Taveira Pinto, director of SHRHA.

I acknowledge the financial supports provided by Islamic Azad University (Iran) and by University of Porto (Portugal) during my PhD study.

I am also thankful to my colleagues and friends: Ana-Margarida Bento, Pedro Ramos, Tiago Fazeres Ferradosa, Vanessa Ramos, Daniel Ruben, Eliamin Rosendo, Luís Brandão, António Pinto, Hélder Magalhães, Cristina Silva and Arlon André. Many thanks to all of them for their helps and friendly talks during my stay out of my home country, to feel like home.

Last but not least, I would like to acknowledge my dear wife, Mobina, and my family members who supported me during my study with their constant love and words of encouragements.

Mahdi Alemi

"Pedras no caminho? Guardo todas, um dia vou construir um castelo."

Stones in the road? I save every single one, one day I will build a castle.

(Fernando Pessoa, 1888-1935)

Contents

List of Figures

List of Tables

List of Symbols

a_1	Horizontal size of the first cells close to the square cylinder faces (Chapter 3)
A_x	Fractional cell face area open to the flow in the x-direction
A_y	Fractional cell face area open to the flow in the y-direction
A_z	Fractional cell face area open to the flow in the z-direction
C_D	Drag coefficient
$C_{D\ r.m.s.}$	Root-Mean-Square of the drag coefficient fluctuations
$\overline{C}_D$	Time-averaged drag coefficient
C_L	Lift coefficient
$C_{L\ r.m.s.}$	Root-Mean-Square of the lift coefficient fluctuations
$\overline{C}_P$	Time-averaged pressure coefficient
Cs	Smagorinsky coefficient
d_{50}	Mean particle diameter
D	Circular pier/pile diameter or square side length
D_f	Wall damping function
f	Frequency of the vortex shedding
F_D	Drag force
F_L	Lift force
F_P	Pressure force
Fr	Froude number
h	Channel half-height (section 5.3.1), the hill height (section 5.3.2) and water depth (rest of the thesis)
h_{cap}	Pile cap height/thickness
h'	Bed layer height
k	Sub-step number

k	Von Kármán constant (k = 0.4)
k_s^+	Normalized equivalent sand roughness
K	Turbulent kinetic energy
L_{col}	Length of the column
L_r	Recirculation length
L_s	Mixing length
L_z	Length of the computational domain in the z-direction
n	Time-step counter
p	Pressure
p_∞	Free stream pressure
r	Radial direction
R_D	Radius of the computational domain (O-type mesh)
$\mathrm{Re_b}$	Reynolds number based on the bulk velocity and hill height, $\mathrm{Re_b} = U_\mathrm{b}h/\vartheta$
Re_D	Reynolds number based on the approach velocity and pier diameter, Re_D=$U_\infty D/\vartheta$
Re_h	Reynolds number based on the approach velocity and water depth, Re_h=$U_\infty h/\vartheta$
Re_τ	Reynolds number based on the friction velocity
R_P	Pile or cylinder radius
S_1	Source term in the momentum equation (x-direction)
S_{ij}	Strain rate tensor
St	Strouhal number, St = fD/U_∞
t	Time
T	Vortex shedding period
u	Flow velocity in the x-direction (Cartesian coordinate system)
u_r	Flow velocity in the radial direction (cylindrical system)
u_t	Wall tangential velocity
u_z	Flow velocity in the vertical direction (cylindrical system)
u_θ	Flow velocity in the azimuthal direction (cylindrical system)

u'	u-velocity fluctuation
u_i^*	Intermediate velocity field (i = 1, 2 and 3 representing u^*, v^* and w^*, respectively)
u_i^{**}	Intermediate velocity field
u_*	Friction velocity or shear velocity
$\|U\|$	Velocity magnitude
U_b	Bulk velocity at the crest of the hill
U_∞	Approach flow mean velocity
v	Flow velocity in the y-direction
v'	v-velocity fluctuation
V	Average cross-sectional flow velocity
V_F	Volume fraction of the fluid in a grid cell
w	Flow velocity in the z-direction
w'	w-velocity fluctuation
W_cap	Pile cap width
WS_i	Wall shear stress component (FAVOR method)
x	Longitudinal direction
x_{2C}	Normal distance from the first tangential velocity node to the wall surface
X_{DOWN}	Distance from the cylinder/pile center to the outlet boundary section
X_{UP}	Distance from the cylinder/pile center to the inlet boundary section
y	Transverse or lateral direction
y_c	Cell center normal distance to the wall
y^+	Non-dimensional wall distance
z	Vertical direction
ρ	Fluid density
μ	Dynamic viscosity
ϑ	Kinematic viscosity, $\vartheta = \mu/\rho$
ϑ_t	Eddy viscosity
ω	Vorticity

ψ	Stream-function
ϕ	Pseudo-pressure: a scalar quantity that contains the pressure and some additional terms
θ	Azimuthal direction
ε	Turbulent dissipation rate
τ_{ij}	Subgrid-scale stress tensor
τ_w	Wall shear stress
Δ	Spatial filter width
Δr_1	Radial cell width close to the circular cylinder surface
Δt	Time-step size
$\Delta\theta$	Grid points spacing in the azimuthal direction (O-type mesh)
δ	Approach boundary layer thickness
δ_{ij}	Kronecker delta
δx	Grid cell size in the x-direction
δy	Grid cell size in the y-direction
δz	Grid cell size in the z-direction
$<\ >$	Flow quantity inside the symbol was averaged either in the longitudinal or vertical direction.
$<<\ >>$	Flow quantity was averaged in the both longitudinal and transverse directions.
$\bar{}$	Flow quantity below the overbar was averaged over time.

List of Abbreviations

AB	Adams-Bashforth
CBC	Convective Boundary Condition
CD	Central Differencing
CFD	Computational Fluid Dynamics
CFL	Courant-Friedrichs-Lewy
CN	Crank-Nicolson
DES	Detached Eddy Simulation
DNS	Direct Numerical Simulation
FAVOR	Fractional Area-Volume Obstacle Representation
LES	Large Eddy Simulation
QUICK	Quadratic Upwind Interpolation for Convective Kinematics
RANS	Reynolds Averaged Navier-Stokes
RK	Runge-Kutta
SC	Stability Criterion
SOR	Successive Over-Relaxation
TR	Turbulence Resolution
2-D	Two-Dimensional
3-D	Three-Dimensional

CHAPTER 1

Introduction

1.1 Motivation

Bridges are important and vital structures, which are exposed to many natural hazards such as local scouring. Due to its direct impact on the stability of bridge piers, local scour plays a key role in bridge failure (some examples are presented in Figure 1.1). Hence, the scouring process is very important for the bridge pier stability studies and must be carefully investigated, as under-prediction of the scour depth may lead to the bridge failure while its over-prediction may lead to waste of economic resources. Therefore, a good understanding of the scour process and a better estimation of the scour-hole dimensions are of utmost importance in civil engineering.

Figure 1.1: Examples of bridge failures: a) Jahrom-Iran, 2017, reported by IRNA (http://www.irna.ir/fa/News/82430384); b) Gafanha-Portugal, 1994, photo adopted from Moreno (2016).

Local pier scour is a complex three-dimensional phenomenon, which occurs as a result of the flow-sediment-pier interaction. So far, numerous experimental and numerical studies have been performed to investigate the flow mechanism and scouring process around a single pier (Dargahi, 1989; Graf & Istiarto, 2002; Kirkil et al., 2008; Diab, 2011; Khosronejad et al., 2012; Alemi & Maia, 2018 among others), mostly with a circular cross-section geometry. Nevertheless, most modern bridges are supported by piers with complex geometries because of geotechnical and economic considerations. Few studies focused on the investigation of complex bridge piers, which is a consequence of the fact that physical study of complex piers is time-consuming and expensive (Beheshti & Ataie-Ashtiani, 2010). In fact, due to the variety in shape, size and configuration of the pier elements, a systematic and complete study on complex piers requires many experiments to be performed. In contrast, using powerful and affordable computers, Computational Fluid Dynamics (CFD) analysis is able to present further results (e.g., flow velocity field around the complex bridge piers) and with lower costs compared to the physical models. Furthermore, CFD analysis enables to overcome problems due to disturbances caused by measuring instruments and simultaneously avoids issues related to scaling of experimental results.

Considering above explanations, this study was aimed to contribute to the numerical investigation of the flow field around complex bridge piers, having in attention that a good understanding of the flow mechanism is a fundamental step to estimate the accurate scour depth around bridge piers.

1.2 Aim and Scope

In general, the turbulent flow past a bridge pier is complex, including flow separation, reattachment, and vortices. Therefore, a challenging subject for this PhD study was selecting adequate numerical methods to simulate these flow phenomena in a simple, fast and accurate way. A preliminary bibliographic survey on related works resulted in having in mind to address some key features for the present numerical study as follows:

- Kirkil et al. (2009) noted that, ideally, a Large Eddy Simulation (LES) without wall function should be used to investigate such turbulent flows. Nevertheless, some restrictions due to the grid resolution and time-step size requirements, for a sufficiently resolved LES, make

LES applicable only for relatively small Reynolds numbers ($\sim 10^4$). At very large Reynolds number flows, LES together with a wall function can be considered for the solution. The present study attempts to investigate if it is possible to obtain adequate numerical results using a wall function on the bridge pier flow predictions. For that, a wall function, as used in many studies on local pier scour predictions (Roulund et al., 2005; Stahlmann, 2013 among others), was adopted for the present study. In addition, a Two-Layer approach was also selected for the wall modeling; by that, the LES domain is the core of the flow and in the wall layer a simplified set of flow equations is considered and solved by means of a grid that is refined in the wall-normal direction. That approach has given reasonable accurate predictions in complex flows such as the flow past the backward-facing step and trailing edge as reported by Piomelli & Balaras (2002).

- One difficulty in solving the set of flow equations, continuity and Navier-Stokes equations, is that there is no explicit equation for the pressure. One way to overcome this difficulty is to employ the fractional-step or projection method that removes the implicit pressure dependence in the Navier-Stokes equations. That method has been extensively applied in Large Eddy Simulations (Sohankar et al., 2000; Mahesh et al., 2004; Kirkil et al., 2008; Meyer et al., 2010; Einian, 2012 among others), possibly due to its efficiency in computational time at high Reynolds numbers (Majander & Siikonen, 2002; Hines, 2008).

- Tessicini et al. (2002) noted that structured grids with orthogonal grid lines allow flow simulations to be performed in a simple way with high efficiency and accuracy. In this case, flow obstacles are immersed into a Cartesian grid which can be easily generated compared to a body-fitted grid. A difficulty in using the Cartesian grid is that the physical boundary of a body may not conform to a grid line. In order to overcome this difficulty, the immersed-boundary method (as reported by Tessicini et al. (2002) and Posa & Balaras (2014)) or a porosity technique known as the Fractional Area-Volume Obstacle Representation (FAVOR) method (Hirt & Sicilian, 1985) is desirable for the definition of the flow obstacles. In the immersed-boundary method, the effect of the obstacle on the flow is usually accounted for by estimation of an appropriate body-force term in the Navier-Stokes equations. In contrast,

the FAVOR method uses open volume and area fractions of the grid cells for incorporating geometry effects into the flow equations.

In the literature, there are some numerical models used to predict fluid-structure interaction. Nevertheless, most of them are private or proprietary, usually without access to the source code for implementation of the required methods. In contrast, for example, OpenFOAM is a free and open-source toolbox, but the key features mentioned above are not apparently addressed in it, meaning that many changes/implementations would be required to be performed in OpenFOAM to consider it adequate for the present numerical study. Better than investing on that, it was decided to develop an in-house CFD model based on the required features for the bridge pier flow predictions.

Developing a numerical model, in addition to the key features mentioned above, requires investigation on the spatial and temporal discretization of the governing equations and also on parallel computing, which are important factors in accuracy and efficiency of a numerical model. Thus, those investigations were also adopted as objectives for this study.

By achieving the aforementioned objectives, the numerical model can be used in engineering practice as a tool to assess the flow behavior around any structure in the river. In the present study, the application of the numerical model to predict the turbulent flow around two complex bridge piers for different stages of the local scour process is presented. It should be noted that, to the author's knowledge, available numerical and experimental studies on the flow field around complex bridge piers are mostly limited to the fixed flat-bed cases and few studies have been performed to investigate the flow field around a complex pier on a scoured bed. The work presented here will serve as a basis for a future broader analysis of the local scour hole around complex bridge piers. In summary, the main objectives of the present study are as follows:

- Developing a numerical model for complex geometries flow predictions by:

    1. Investigating different schemes for the spatial and temporal discretization of the governing equations;
    2. Employing a parallelization technique for numerical calculations, especially to solve the implicit Poisson equation;
    3. Evaluating the applicability of the LES model with a wall function;

4. Employing the immersed-boundary or FAVOR method to model complex geometries.

- Applying the numerical model developed to predict the flow around complex bridge piers on the scoured bed.

1.3 Synopsis

The present thesis is organized into seven chapters. In this first chapter, the motivation and objectives of this study were presented. The rest of the thesis is organized as follows:

Chapter 2 presents a summary of the background knowledge on the flow field around single circular piers and the complex bridge piers selected for this study.

Chapters 3 to **5** describe the numerical model development and validations. The numerical model was developed in three main steps (each corresponding to one of Chapters 3, 4 and 5), meaning that the model development was started by considering a simple case in a first step and then by adding required features to the model in each new step. The accuracy of the numerical model was also evaluated in each step by comparing the corresponding numerical results with available reference data for different benchmark cases. Details of the Chapters 3, 4 and 5 are as follows:

- In Chapter 3, the study was aimed at finding an adequate solution procedure for the continuity and the Navier-Stokes equations (flow equations set) based on the fractional-step method. Different schemes were employed to approximate the spatial and temporal derivative terms and the corresponding numerical results were compared taking into account available reference data. In addition, the effects of the computational time-step size on the accuracy of the results were investigated. Moreover, the optimization of the computational time on solving the implicit equations (e.g., Poisson equation) by parallel computing was also addressed. For simplicity in the solution, calculations were performed under the laminar flow condition. Overall, the results of Chapter 3 served as a basis for the development of an adequate numerical model for the study of the turbulent flow in the following chapter.

- In Chapter 4, this study attempted to contribute to modeling turbulent flows using the LES together with a simple wall model (the so-called Two-Layer approach). In this chapter, at

first, a review of different turbulence models is presented and then details of the numerical model are summarized. In the LES model, a filtering procedure is used to decompose each flow quantity into large-scale and small-scale components. The large-scales are calculated directly and the effect of the small-scales is modeled by using a subgrid-scale model. In this study, the standard Smagorinsky model with a constant coefficient was used as a subgrid-scale model that is computationally inexpensive compared to a dynamic approach. Therefore, the applicability of the Smagorinsky subgrid-scale model was evaluated by considering turbulent flow past square and circular cylinders, using different values of the Smagorinsky coefficient and different definitions to compute the spatial filter width.

- In Chapter 5, this study was aimed at enhancing the numerical model for modeling the complex geometries in a Cartesian grid system. In addition, a rough wall function was also incorporated in the numerical model to take into account the bed roughness effects in the predictions. The accuracy of the numerical model was evaluated by considering different case studies (turbulent channel flow over flat-bed, turbulent flow in a channel with periodic hill constrictions and turbulent flow around a single and compound piers on the eroded bed) and comparing the corresponding numerical results with available reference data. The turbulent channel flows mentioned above have been widely investigated experimentally and numerically during last years, which enabled to consider those as benchmark cases for the present study. In addition, a realistic inflow condition for bridge pier flow predictions can be provided by the channel-flow calculations. The single pier case was particularly selected to assess the capability of the numerical model to capture the main flow features around the single pier, which are already well known. Further, the experimental bed shear stress results, available for the single pier case, enabled to control the accuracy of the numerical results. The compound pier case (a circular pier on a circular foundation) was also selected for validation purposes, because the corresponding experimental velocity profiles are available, making the accuracy study straightforward.

Chapter 6 presents the application of the numerical model to simulate the flow around two complex bridge piers on the scoured bed. The pier cases (referred to as case I and II) consist of a column and a pile cap supported by a group of piles, a common geometry of complex bridge piers.

The two pier cases differ in the number of the piles and also nose shape of the column and pile cap. Moreover, all pier elements in case I were exposed to the approaching flow, while in case II, the pile cap was positioned in such a way that only half of its height was above the initial channel bed level. The detailed bathymetry of the local scour holes were obtained from experiments conducted by Beheshti & Ataie-Ashtiani (2016) and Ramos et al. (2016). Beheshti & Ataie-Ashtiani (2016), pier case I, also measured velocity components around the complex pier at the equilibrium stage of the scour hole process using acoustic-Doppler velocimeter. Their laboratory measurements could not be performed inside the scour hole and at points closer than 3.5 cm to the pier elements, as the measuring instrument imposed limitations. The present numerical study provided further details about the flow field compared to the experimental study, helping to understand better the flow mechanism around the complex pier on the scoured bed. Concerning the case II, Ramos et al. (2016) conducted a series of experimental tests at the Hydraulics Laboratory in the University of Porto to study the time development of local scour around a complex pier and presented the scour hole geometries at different stages of the local scouring process. However, the characterization of the flow field was not experimentally investigated by Ramos et al. (2016). Therefore, the present numerical study investigated the flow field changes around the complex pier case II during the local scour process. For that, numerical predictions were performed for different bed configurations, namely, initial flat-bed condition, intermediate stages and equilibrium condition of scour holes.

Chapter 7 presents the main conclusions and recommendations for future works.

CHAPTER 2

Background of the Flow around Studied Pier Cases

2.1 Introduction

This chapter makes a review of the relevant literature for the studied pier cases. Firstly, the flow behavior around single bridge piers is summarized and some of the significant works are presented. Then, background knowledge of the flow structure around the complex bridge piers, the ones selected for this study, is presented. The corresponding information are useful for verification and validation of the present numerical model.

2.2 Single bridge piers

The flow structure around single bridge piers has been studied in the last few decades experimentally and numerically, mostly by considering a circular cross-section geometry (e.g., Raudkivi, 1986; Dargahi, 1989; Melville & Coleman, 2000; Roulund et al., 2005; Kirkil et al., 2008; Ataie-Ashtiani & Aslani-Kordkandi, 2013; Baykal et al., 2015). The main reported flow features are the surface roller (also known as the bow wave) and down-flow at the front of the pier, the horse-shoe vortex at the base of the pier and the wake vortices downstream of the pier as shown in Figure 2.1.

When a unidirectional flow is partially obstructed by a single pier, the flow is deflected in the vertical direction in front of the pier, resulting in two vertical jets (up-flow and down-flow).

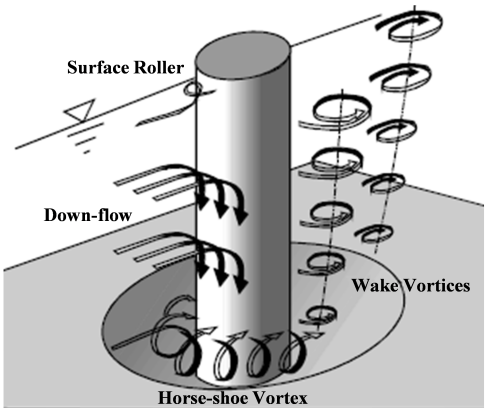

Figure 2.1: Flow pattern around a circular pier, adopted from Melville & Coleman (2000).

The flow deflection occurs near the water surface where the stagnation pressure ($0.5\rho u^2$, in which ρ denotes the fluid density and u represents the flow velocity) is the highest and that pressure decreases downwards, generating the down-flow. Raudkivi (1986) reported that the maximum value of the down-flow for a flat-bed case is about 40% of the approach flow mean velocity (U_∞) and occurs at 0.05 to 0.02 pier diameters (D) upstream of it, being closer to the pier bottom. For a scoured bed, that value increases with increasing scour depth up to $0.8U_\infty$, for a position located about $1D$ below the initial channel bed level, when the maximum scour depth is about $2.3D$.

The down-flow separates at the pier's base and rolls up to form an initial rotational flow system, known as the horse-shoe vortex system, by interaction with the incoming flow. In other words, for the flat-bed case, a horse-shoe vortex system is generated when the approaching boundary layer separates from the bed (see Figure 2.2 a)). Roulund et al. (2005) reported that the separation point location, for a flat-bed case, depends mainly on the bed roughness, the Reynolds number ($\mathrm{Re}_D = U_\infty D/\vartheta$, in which ϑ is the kinematic viscosity) and ratio of the approach boundary layer thickness to the pier diameter (δ/D). In summary, for a flat-bed case, the separation point moves towards the pier with increasing the bed roughness, increasing Re_D (when $\mathrm{Re}_D > 500$) and decreasing δ/D. As the scour hole grows, the approach flow separates at the upstream rim of the scour hole and the horse-shoe vortex system forms inside the scour hole (see Figure 2.2 b)), leading to the maximum down-flow velocity to occur inside the scour hole. Generally, the horse-shoe system consists of a main/major vortex associated with several small secondary vortices, all of those wrapping around the pier's base (see Figure 2.2 c)) and extending downstream for a few

pier diameters before losing their identity and becoming part of the general turbulence field. In fact, the horse-shoe vortices transport eroded sediment particles downstream of the pier. Dargahi (1989) experimentally investigated the flow structure around a circular pier mounted vertically on a fixed flat-bed for Re_D ranging from 6600 to 65000 and noticed that the number of vortices formed upstream of the pier depends on Re_D, while the dimensions of the vortex system were found to be independent of Re_D and primarily can be determined by the pier diameter. Later, Muzzammil & Gangadhariah (2003) experimentally studied the time-averaged characteristics of the horse-shoe vortex system along the scouring process. The corresponding measurements showed that the main horse-shoe vortex (V2 in Figure 2.2 b)) has an elliptical shape in the vertical symmetry plane. Therefore, Muzzammil & Gangadhariah (2003) evaluated its size as the average of the maximum and minimum diameters of the corresponding ellipse (see Figure 2.2 d)) and concluded that in the case of a flat-bed, the size of the main vortex is about $0.2D$ for Re_D ranging from 10^4 to 1.4×10^5 and that size increases linearly with the scour depth.

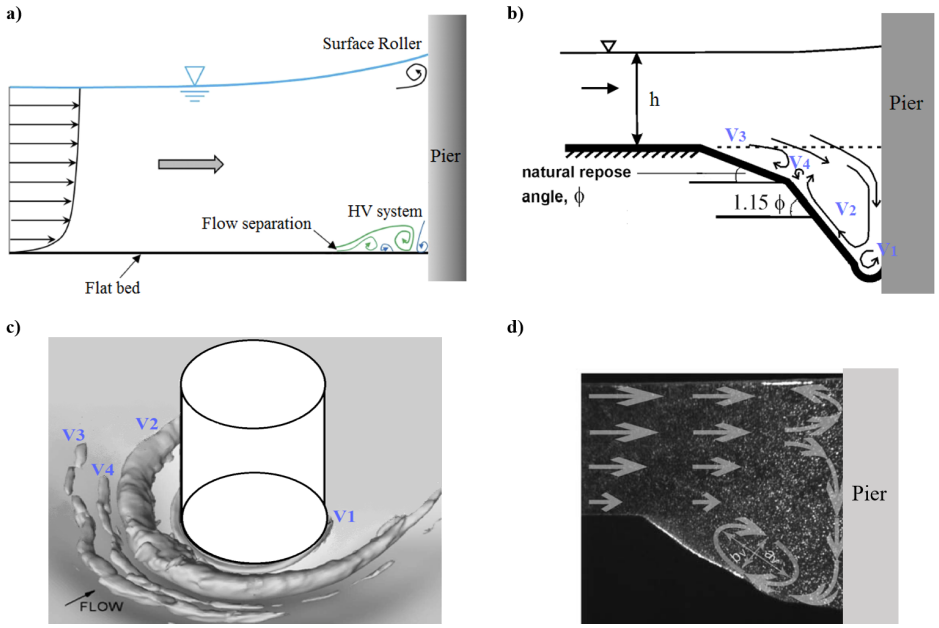

Figure 2.2: The horse-shoe vortex (HV) system formed at the front of a circular pier: a) sketch for a flat-bed, adopted from Chen et al. (2017); b) sketch for a scoured bed, adopted from Link et al. (2008); c) distribution inside the scour hole, visualized by Kirkil et al. (2008); d) schematic flow pattern for a scoured bed, adopted from Unger & Hager (2007).

The horse-shoe vortex system formed at the initial of the scouring process causes a significant increase in bed shear stress around the base of the pier. In fact, scour does occur when the local

bed shear stress is bigger than a critical value. Moreno (2016) reported that as the scour depth increases over time, the strength of the horseshoe vortex weakens, leading to a reduction of the scouring rate. In general, the critical bed shear stress is estimated based on the shields diagram (Shields, 1936), not taking into account the effect of bed slope. Kirkil et al. (2008) computationally obtained the time-averaged bed friction velocity values around a circular pier for the equilibrium scour-hole bathymetry and normalized it by the local slope adjusted critical friction velocity as shown in Figure 2.3. Although, inside the scour hole, larger values were predicted over the whole region beneath the main horse-shoe vortex and over most of the regions close to the junction line of the pier and bed surface (see also vortices V2 and V1 in Figure 2.2 c)), those values are smaller than the local critical values and that is consistent with the equilibrium scour-hole condition.

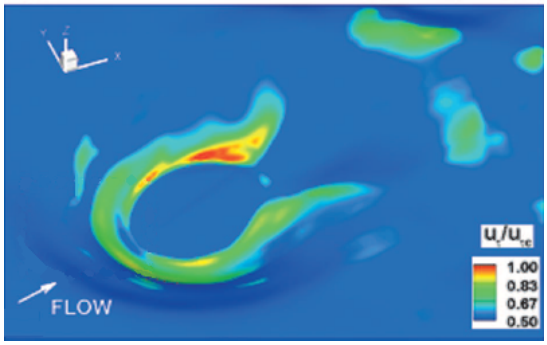

Figure 2.3: Distribution of the time-averaged friction velocity (normalized with respect to local slope adjusted critical friction velocity) over the scoured bed formed around a circular pier, adopted from Kirkil et al. (2008).

The so-called up-flow in front of the pier is directed to the water surface, resulting in increasing the water depth and consequently in the formation of the surface roller that rotates in the opposite direction of the main horse-shoe vortex. When the water depth is deep enough ($D/h < 0.7$, h the approach water depth, as reported by Melville & Coleman (2000)), the local scour depth depends on the pier diameter in contrast to the water depth. As the flow depth decreases, the surface roller becomes important and the local scour depth reduces due to interference between the surface roller and the horse-shoe vortex. Subsequently, in a very shallow flow ($D/h > 5$), the local scour depth is independent of the pier diameter and mainly depends on the water flow depth.

Stagnation pressure in front of the pier also accelerates the flow along the pier sides, resulting in the water-surface drawdown on each side of the pier. Roulund et al. (2005) presented an

equation to estimate the difference in the surface elevation between the front and side edges of the pier (Δh): $\Delta h/h = \mathrm{Fr}^2/2$, which is valid for small Froude numbers (Fr). Therefore, according to Roulund et al. (2005), Δh is very small for small Froude numbers. Moreover, at the sides of the pier, the boundary layer over the pier's surface separates due to the imposed adverse pressure gradient. For a circular bridge pier, the separation points positions change over the height of the pier because the approach velocity is not uniform over the flow depth (Baykal et al., 2015). In addition, Ataie-Ashtiani & Aslani-Kordkandi (2012) attributed that fact to the effect of bed roughness on the turbulence near the bed. The separation of the flow at the sides of the pier creates wake vortices downstream of the pier. Ataie-Ashtiani & Aslani-Kordkandi (2012) reported that the longitudinal extension of the wake region (for the time-averaged flow field) in the scoured-bed case is smaller than that in the flat-bed case, attributed to the geometrical conditions of the bed and the corresponding flow pattern. The wake vortices cause lifting of bed sediments and those are transported downstream by the flow. A deposition then takes place downstream of the pier as the intensity of the wake vortices reduces with distance from the pier. The frequency of the wake vortices, f, is usually presented in terms of the Strouhal number ($\mathrm{St} = fD/U_\infty$). In case of a circular cylinder with an infinite length and smooth surface, St is about 0.2 for a Reynolds number range of 10^4 to 10^5. In case of a wall-mounted cylinder (i.e., single pier on a flat-bed), Ataie-Ashtiani & Aslani-Kordkandi (2013) reported that St near the bed is slightly smaller than that near the mid-depth. Moreover, the presence of the scour hole changes the behavior of the vortex shedding, as several dominant frequencies with a considerable decrease (when compared to the flat-bed case) were observed by Ataie-Ashtiani & Aslani-Kordkandi (2012).

Overall, many research efforts have been performed to investigate the flow behavior around a single pier, but in practical cases, most modern bridges are usually constructed on foundations with complex geometries. In this case, the results obtained from the single pier studies are no more applicable, as the flow structure is affected by the interaction between the complex pier elements.

2.3 Complex bridge piers

During the last years, the complex piers' study has attracted the attention of many researchers. Two valuable systematic studies on the complex piers are the experimental works performed by

Ataie-Ashtiani et al. (2010) and Moreno et al. (2016).

Ataie-Ashtiani et al. (2010) experimentally studied local scouring around complex piers by performing three sets of experiments (69 tests). One set (8 tests) was conducted on a column-foundation combination model and two sets of experiments (61 tests) were conducted on a complex pier model by employing all three complex pier elements (pile group, pile cap and column), considering different sizes and positions of the pier elements. The corresponding maximum scour depth data were used to investigate the effect of the pile cap on the local scour depth. In addition, modifications were proposed to improve the available procedures for estimating the maximum scour depth around the complex piers. Later, following Ataie-Ashtiani et al. (2010), Beheshti & Ataie-Ashtiani (2016) experimentally investigated the turbulent flow field past a certain complex pier formed by a rectangular column with a rectangular pile cap supported by a 2×4 pile group at the equilibrium stage of the scour hole process (see Figure 2.4). All the pier elements were exposed to the approaching flow, a situation that occurs frequently when bridges have a complex pier foundation (Beheshti & Ataie-Ashtiani, 2016). The equilibrium scour hole geometry was measured using a Vernier point gauge and the velocity data were collected using acoustic Doppler velocimeter at different horizontal and vertical planes above the initial channel bed level. The position of each plane can be observed in Figure 2.4. As mentioned before in the Introduction chapter, the laboratory measurements could not be performed inside the scour hole and at points closer than 3.5 cm to the pier elements due to measuring instrument limitations.

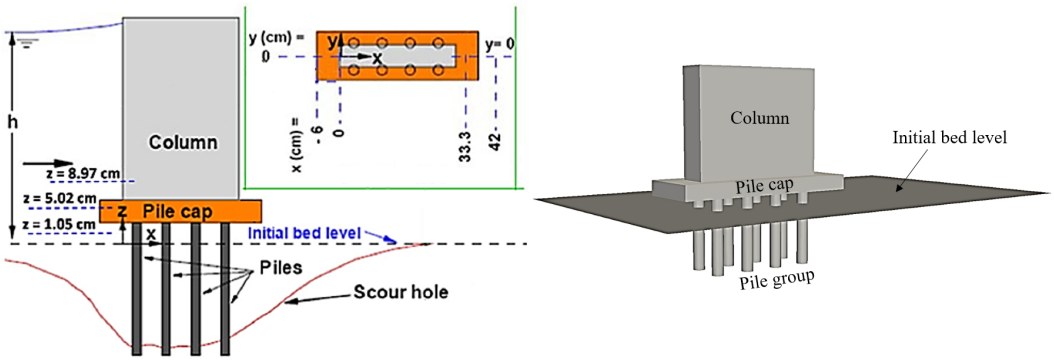

Figure 2.4: The complex bridge pier used in the experiment of Beheshti & Ataie-Ashtiani (2016).

The most relevant flow structures for this case, characterized by the experimental data, are as follows: According to Beheshti & Ataie-Ashtiani (2016), the approaching flow is deflected

downwards in front of the column; it is then diverted sideways by the top surface of the pile cap and then downwards again when flowing around the pile cap side faces. The flow structure along the column side faces was not discussed by Beheshti & Ataie-Ashtiani (2016) as the corresponding experimental results were not available (see Figure 2.5 c)). That was hence investigated in this PhD study and the corresponding results are presented in Chapter 6.

The flow approaching the pile cap is diverted in the vertical direction (both up and down the pile cap) and around the pile cap sides. Beheshti & Ataie-Ashtiani (2016) reported that the flow separates at the upstream side edges of the pile cap and reattaches midway along the pile cap sides, although the corresponding experimental results didn't show any reverse flow in the zone between the separation and reattachments points mentioned above (see Figure 2.5 b)). The possibility of the flow separation along the pile cap sides was hence investigated in this PhD study.

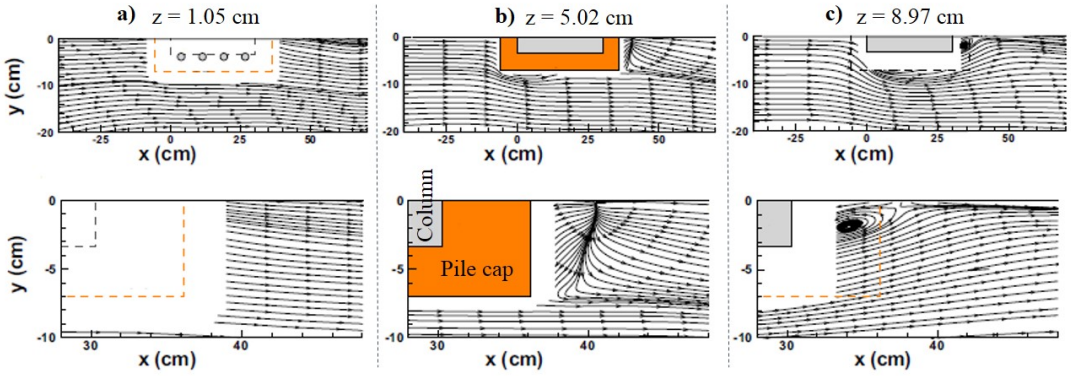

Figure 2.5: Streamlines: (top) at horizontal planes z = 1.05, 5.02 and 8.97 cm (below, about mid-height of and above the pile cap position, respectively); and (bottom) zoomed into the downstream of the complex pier, presented by Beheshti & Ataie-Ashtiani (2016).

Beheshti & Ataie-Ashtiani (2016) reported that no horse-shoe vortex was observed upstream of the pier because the flow near the bed could pass underneath the main obstructing parts of the complex pier. This conclusion was made while the flow field data were not available near the bed, particularly inside the scour hole around the base of the pier (see Figure 2.6), and that justifies the investigation of the flow behavior inside the scour hole performed in the present study.

Downstream of the pier, Figure 2.6 b), a reverse flow region was reported behind the column. Moreover, a downward flow was observed immediately downstream of that reverse flow region and above the pile cap position. The downward flow interacts with the upward outflow from the pile

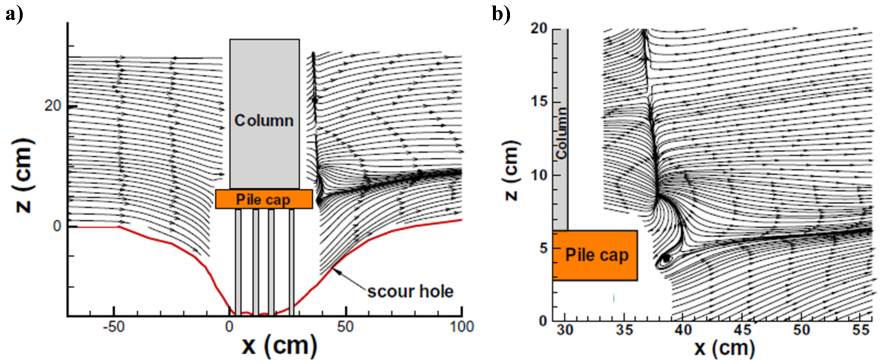

Figure 2.6: Streamlines: a) in the vertical symmetry plane $y = 0$; and b) zoomed into the downstream region, presented by Beheshti & Ataie-Ashtiani (2016).

group region, resulting in a vortex near the bottom downstream edge of the pile cap. In addition, near the top downstream edge of the pile cap, a secondary vortex develops due to the reverse flow behind the pile cap.

The streamlines in the horizontal planes, Figure 2.5, also indicate that the longitudinal extension of the reverse flow region behind the pile cap is smaller than that forms behind the column. Concerning the streamlines in the vertical transverse planes (presented in Figure 2.7), downstream of the column at cross-sections $x = 33.3$ and 42 cm, a small roller was reported at an elevation near the top surface of the pile cap.

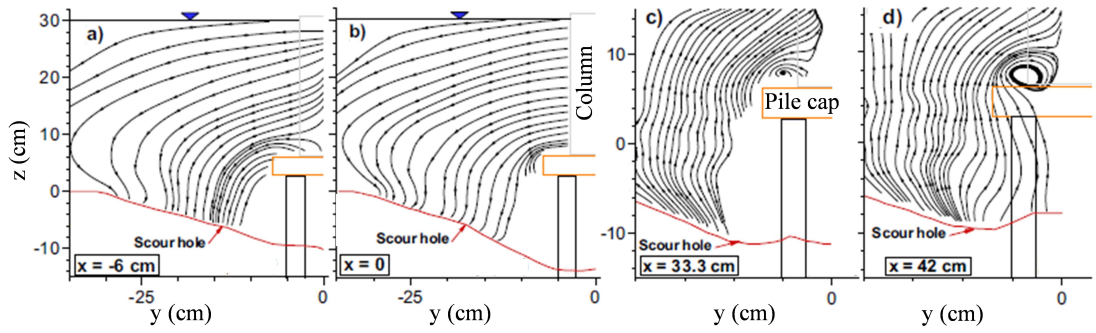

Figure 2.7: Streamlines in different vertical cross-sections: upstream of the column ($x = 0$ and -6 cm) and downstream of the column ($x = 33.3$ and 42 cm), presented by Beheshti & Ataie-Ashtiani (2016).

Moreno et al. (2016) experimentally studied clear-water scour around seven complex pier models, all consisting of a column on a pile cap (both with round nose) supported by a group of piles. Overall, 48 long-duration (7-47 days) laboratory tests were performed to quantify the

influence of the relative column width, the relative pile cap thickness, the pile cap position and the configuration of the pile group on the equilibrium scour depth. The maximum scour depth was recorded during each test, and the equilibrium depth could be estimated by extrapolation of the experimental data series. The performance of the most common existing methods to estimate the equilibrium scour depth around the complex piers was evaluated and an alternative formulation for that estimation was proposed.

Although the characterization of the flow field and scouring process development were not experimentally obtained in that study, Moreno et al. (2016) presented an interpretation of the flow structure around the complex piers on the scoured bed as shown in Figure 2.8.

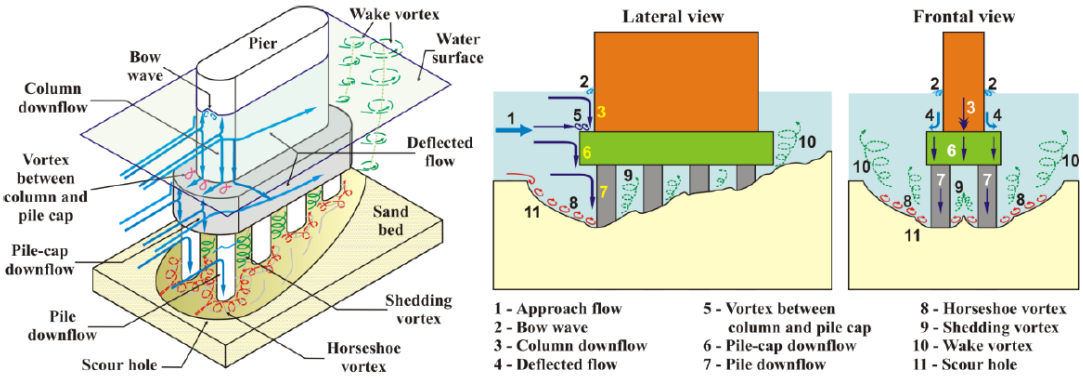

Figure 2.8: Sketch of the flow structure around a complex bridge pier, adopted from Moreno et al. (2016) and Moreno (2016).

In accordance to Figure 2.8, the flow approaching the column is affected as on the case of a single bridge pier: the approaching flow is deflected towards the sides of the column in the horizontal direction and in the vertical direction at the front face of the column (up-flow and down-flow). The vertical deflection results in the formation of the surface roller (or bow wave) at the water surface and vortices in front of the column on the top surface of the pile cap. Concerning the pile cap, a similar flow behavior was shown: vertical and sideways deflection of the flow. Although diverting the approaching flow around the sides of the column and pile cap was shown by Moreno et al. (2016), still information about the flow separation and the corresponding vortices are missing. Hence, the flow structure along the pile cap and column sides was investigated in this PhD study and the corresponding numerical results are presented in Chapter 6.

In front of the upstream piles, unlike the column and pile cap, only a downward flow was shown in Figure 2.8. Nevertheless, if an upward flow forms in front of those piles, then the formation of a reverse flow region is expected to take place near the upper part of the upstream piles by interaction with the pile cap bottom surface. That may be influenced by deflection of the approaching flow at the lower upstream edge of the pile cap. The existence of that reverse flow region was also investigated in this PhD study.

Inside the scour hole, unlike Beheshti & Ataie-Ashtiani (2016), Moreno et al. (2016) reported the circulation of the horse-shoe vortex system. Moreover, a similar pattern for vortices behind the piles (also similar to a single pier case as shown in Figure 2.1) was shown in Figure 2.8, probably, meaning that the interaction between the pile group and pile cap was assumed negligible. This interpretation requires more investigations which have been performed in this PhD study.

Downstream of the complex pier, in Figure 2.8, wake vortices have a simple pattern similar to that reported for a single pier in Figure 2.1, while Beheshti & Ataie-Ashtiani (2016) observed a more complicated flow structure in the downstream zone. Therefore, the complexity of the flow downstream of the complex pier was numerically investigated in this study.

It is noteworthy to recall that Moreno et al. (2016) did only characterize the temporal variation of the maximum scour depth in front of the complex piers considered in the systematic study. Following Moreno et al. (2016), Ramos et al. (2016) measured the temporal development of the scour hole geometry (information required for the numerical predictions) using photogrammetry for a complex pier model under similar flow conditions as used in one of the experiments carried out by Moreno et al. (2016). The complex pier model, employed by Ramos et al. (2016), has a 1×4 pile group compared to that in Figure 2.8. In addition, half-height of the pile cap was initially buried in the bed. The corresponding scour hole geometries developed at different stages of the scour process (available at https://web.fe.up.pt/~numpiers/NUMPIERSDB/doku.php) were used for the corresponding flow predictions performed in the present numerical study.

CHAPTER 3

Numerical Solution for Flow Equations

3.1 Introduction

The spatial and temporal evolution of a fluid flow is described by means of the continuity and Navier-Stokes (or momentum) equations. The mentioned flow equations set, for incompressible and constant viscosity flow, are written as:

$$\mathrm{div}(u_i) = \frac{\partial u_i}{\partial x_i} \tag{3.1}$$

$$\frac{\partial u_i}{\partial t} + \frac{\partial u_i u_j}{\partial x_j} = -\frac{1}{\rho}\frac{\partial p}{\partial x_i} + \vartheta \frac{\partial^2 u_i}{\partial x_j^2} \tag{3.2}$$

where x_i and x_j, i and j = 1, 2 and 3 denote the longitudinal (x), transverse (y) and vertical (z) directions. Parameters u_i and u_j are the velocity components in the mentioned directions (u, v and

w, respectively), p is the pressure, t represents time, ρ is the fluid density and ϑ is the kinematic viscosity ($\vartheta = \mu/\rho$, in which μ is the dynamic viscosity).

The first and second terms on the left-hand side of equation 3.2 are called the transient and convection terms, respectively. The terms on the right-hand side that are multiplied by the viscosity are called the diffusion terms and the remaining term is the pressure term.

In order to solve the flow equations set, it is necessary to know how to discretize the momentum equations spatially and temporally. In addition, as the momentum equations include pressure gradients, a method to obtain the pressure is also required in the solution. Hence, Chapter 3 is focused on the solution methods of the flow equations set and for simplicity, the attention is restricted to a two-dimensional (2-D) unsteady laminar flow on a rectangular mesh. The corresponding methods and schemes can be readily extended for three-dimensional (3-D) cases, presented in the following chapters.

3.2 Pressure solver

One difficulty in solving the set of the flow equations 3.1 and 3.2, hereafter also referred to as the velocity-pressure formulation, is that there is no explicit equation for the pressure. The problem in obtaining the pressure arises because, although there are 3 equations for u, v and p, the continuity equation does not actually contain the pressure explicitly.

An alternative formulation can be obtained by writing the flow equations in the vorticity and stream-function ($\omega - \psi$) form, in which the pressure is absent in the main equations. Alemi & Maia (2017) evaluated the two mentioned formulations by considering the 2-D steady laminar flows past a square cylinder and noticed that solving the $\omega - \psi$ formulation is much faster than the velocity-pressure formulation, because fewer equations are solved for the $\omega - \psi$ formulation (three unknown parameters u, v and p in contrast to the single stream-function and vorticity). Nevertheless, for a 3-D case, the velocity-pressure formulation has four unknowns, while the $\omega - \psi$ formulation has six, three components for the vorticity and three for vector stream-function. Therefore, the $\omega - \psi$ form of the flow equations was considered not interesting for further studies and hence the solution methods for the velocity-pressure formulation are presented in this chapter.

To solve the velocity-pressure coupling, a common way of dealing with the pressure is to use the fractional-step or projection method (e.g., Kim & Moin, 1985; Le & Moin, 1991; Choi & Moin, 1994) that decouples the computations of the pressure and velocity field in the solution by splitting each time step into some consecutive sub-steps. In this method, an intermediate velocity field is computed using the momentum equations and then the intermediate velocity field is projected onto the divergence-free field to get the next update of the pressure and velocity values.

For 2-D calculations, addressed in this chapter, a basic projection method was selected, by which the pressure gradients are dropped from the momentum equations and that requires a special care on the boundary conditions for the intermediate velocity field. The method was then improved for use on 3-D computations (to be addressed in following chapters) by including the pressure gradient terms, initially estimated from the previous time-step data in the momentum equations, as explained by Choi & Moin (1994).

3.3 Temporal discretization

A fully explicit scheme for temporal discretization of the momentum equations is conditionally stable, while a fully implicit scheme is unconditionally stable but an iteration or linearization is required on non-linear convection terms (Biringen & Chow, 2011).

Kim & Moin (1985) presented a fractional-step method for solving the time-dependent incompressible Navier-Stokes equations, in which a semi-implicit scheme was used for temporal discretization: the explicit second-order Adams-Bashforth (AB) for the convection terms and the implicit second-order Crank-Nicolson (CN) for the diffusion terms. In this case, the time-step size (Δt) should satisfy (Le & Moin, 1991):

$$\mathrm{CFL} = \Delta t \left(\frac{|u|}{\delta x} + \frac{|v|}{\delta y} \right) \leq \text{stability limit} \tag{3.3}$$

where δx and δy are the grid cell size in x- and y- directions; CFL denotes the Courant-Friedrichs-Lewy number. Le & Moin (1991) introduced a nominal stability limit of 0.5 for the AB-CN scheme.

The implicit treatment of the diffusion terms omits the time-step restriction, originating from those terms, which is particularly severe near wall surfaces where the computational grid is refined. The convection terms do not introduce the same limitation because the velocity is generally small close to the wall surface.

Following Kim & Moin (1985), Le & Moin (1991) improved the method by replacing the AB scheme with the third-order Runge-Kutta (RK) scheme, what resulted in increasing the stability limit of the solution method ($\sqrt{3}$) and consequently in using a larger time-step size than that with the AB-CN scheme. Later, Moin (1995) employed the RK-CN scheme to solve the 3-D incompressible Navier-Stokes equations for turbulent flows by noting that both the convection and diffusion terms in the wall-normal direction are equally important in limiting the time-step size. Therefore, all terms in the two other directions were treated explicitly in the calculations of Moin (1995). It is noted that the implicit treatment of the convective terms with derivatives in the wall-normal direction requires a complicated and costly solution technique compared to the method presented by Le & Moin (1991).

For the present study, two semi-implicit AB-CN and RK-CN schemes are presented, in which all the convection terms in the momentum equations are treated explicitly and the diffusion terms implicitly.

*** *Adams-Bashforth and Crank-Nicolson scheme***:

Applying the AB-CN scheme on equation 3.2 yields:

$$\frac{u_i^{n+1}-u_i^n}{\Delta t}=\frac{1}{2}\left[3\mathrm{A}(u_i^n)-\mathrm{A}(u_i^{n-1})\right]+\frac{1}{2}\left[\mathrm{B}(u_i^{n+1})+\mathrm{B}(u_i^n)\right]-\frac{1}{\rho}\frac{\partial}{\partial x_i}(p^{n+1}) \tag{3.4}$$

where superscript n represents the time-step counter and two operators A and B are defined as the convection and diffusion terms, respectively:

$$\mathrm{A}(u_i)=-\frac{\partial u_i u_j}{\partial x_j} \tag{3.5}$$

$$\mathrm{B}(u_i)=\vartheta\frac{\partial^2 u_i}{\partial x_j^2} \tag{3.6}$$

A fractional-step method to remove the dependence of the unknown pressure can be as:

$$\frac{u_i^* - u_i^n}{\Delta t} = \frac{1}{2}\left[3\mathrm{A}(u_i^n) - \mathrm{A}(u_i^{n-1})\right] + \frac{1}{2}\left[\mathrm{B}(u_i^*) + \mathrm{B}(u_i^n)\right] \tag{3.7}$$

$$\frac{u_i^{n+1} - u_i^*}{\Delta t} = \frac{1}{2}\left[\mathrm{B}(u_i^{n+1}) - \mathrm{B}(u_i^*)\right] - \frac{1}{\rho}\frac{\partial}{\partial x_i}(p^{n+1}) = -\frac{\partial}{\partial x_i}(\phi^{n+1}) \tag{3.8}$$

where u_i^* is the intermediate velocity in the subscript direction and ϕ is a scalar that contains the pressure and the residual viscous terms. The pressure can then be computed based on the scalar ϕ as follows:

$$p = \rho\phi - \frac{\mu\ \Delta t}{2}\nabla^2\phi \tag{3.9}$$

where symbol ∇^2 denotes the Laplace operator.

Finally, the solution procedure for the AB-CN scheme at each time step is as follows:

1. Solve for intermediate velocities u_i^* from equation 3.7. The boundary conditions for the intermediate velocities, required in solving equation 3.7, can be obtained through following equation (Kim & Moin, 1985):

$$u_i^* = u_i^{n+1} + \Delta t\frac{\partial \phi^n}{\partial x_i} + \mathrm{O}(\Delta t^2) \tag{3.10}$$

2. Solve for ϕ^{n+1}: combination of equation 3.8 with the continuity equation gives a discrete Poisson equation as:

$$\nabla^2\phi^{n+1} = \frac{\mathrm{div}(u_i^*)}{\Delta t} \tag{3.11}$$

3. Update the velocity values using equation 3.8.

*** *Runge-Kutta and Crank-Nicolson scheme***:

In this scheme, every time step is divided into three sub-steps, each one using an explicit treatment for the convection terms and an implicit one for the diffusion terms as follows (Le &

Moin, 1991):

$$\mathrm{div}(u_i^k) = 0 \tag{3.12}$$

$$\frac{u_i^k - u_i^{k-1}}{\Delta t} = \beta_k \left[\mathrm{B}(u_i^k) + \mathrm{B}(u_i^{k-1}) \right] + \gamma_k \mathrm{A}(u_i^{k-1}) + \zeta_k \mathrm{A}(u_i^{k-2}) - 2\beta_k \frac{1}{\rho} \frac{\partial}{\partial x_i}(p^k) \tag{3.13}$$

where k = 1, 2 and 3 denotes the sub-step number such that $u_i^{k-1} = u_i^n$ for k = 1 and $u_i^k = u_i^{n+1}$ for k = 3. Le & Moin (1991) selected values of the coefficients (β_k, γ_k and ζ_k) as

$$\beta = [4/15,\ 1/15,\ 1/6]; \quad \gamma = [8/15,\ 5/12,\ 3/4]; \quad \zeta = [0,\ -17/60,\ -5/12]$$

such that the total time accuracy was of third-order for the convection terms and of second-order for the diffusion terms.

Applying the projection method on equations 3.12 and 3.13 yields following governing equations:

$$\frac{u_i^{*k} - u_i^{k-1}}{\Delta t} = \beta_k \left[\mathrm{B}(u_i^{*k}) + \mathrm{B}(u_i^{k-1}) \right] + \gamma_k \mathrm{A}(u_i^{k-1}) + \zeta_k \mathrm{A}(u_i^{k-2}) \tag{3.14}$$

$$\frac{u_i^k - u_i^{*k}}{\Delta t} = \beta_k \left[\mathrm{B}(u_i^k) - \mathrm{B}(u_i^{*k}) \right] - 2\beta_k \frac{1}{\rho} \frac{\partial}{\partial x_i}(p^k) = -\frac{\partial}{\partial x_i}(\phi^k) \tag{3.15}$$

$$\nabla^2 \phi^k = \frac{\mathrm{div}(u_i^{*k})}{\Delta t} \tag{3.16}$$

Solving the above governing equations at each sub-step causes a significant increase in computational cost. Hence, Le & Moin (1991) modified equation 3.14 to eliminate solving the Poisson equation 3.16 at each sub-step. In fact, the Poisson equation is only solved at the final sub-step 3. In this modified scheme, the intermediate velocities at sub-step 1 are computed using equation 3.14 and for sub-steps 2 and 3, those velocities are computed through the following equation:

$$\frac{u_i^{*k} - u_i^{*k-1}}{\Delta t} = \beta_k \left[\mathrm{B}(u_i^{*k}) + \mathrm{B}(u_i^{*k-1}) \right] - \beta_k \vartheta \frac{\partial}{\partial x_i} \left(\frac{\partial u_j^{*k-1}}{\partial x_j} \right) + \gamma_k \mathrm{A}(\tilde{u}_i^{k-1}) + \zeta_k \mathrm{A}(\tilde{u}_i^{k-2}) \tag{3.17}$$

where

$$\tilde{u}_i^m = u_i^{*m} - \Delta t \sum_{l=1}^{m} 2\beta_l \frac{\partial \phi^n}{\partial x_i}, \quad m = 1 \text{ and } 2$$

$$\tilde{u}_i^0 = u_i^n$$

The boundary conditions for the intermediate velocities can be calculated at each sub-step through the following equation, proposed by Le & Moin (1991):

$$u_i^{*k} = u_i^n + \left(u_i^{n+1} - u_i^n + \Delta t \frac{\partial \phi^n}{\partial x_i} \right) \sum_{l=1}^{k} 2\beta_l \quad , \qquad k = 1, 2 \text{ and } 3 \tag{3.18}$$

Finally, the solution procedure for the RK-CN scheme at each time step can be constructed as follows:

1. Solve for u_i^{*k} using equation 3.14 for k = 1 and equation 3.17 for k = 2 and 3
2. Solve for ϕ^3 using equation 3.16
3. Update the velocity field:

$$u_i^{n+1} = u_i^{k=3} = u_i^{*3} - \Delta t \frac{\partial \phi^3}{\partial x_i} \tag{3.19}$$

3.4 Spatial discretization

The spatial discretization of the governing equations was performed on the staggered grid system such that the velocities are calculated on the grid cell interfaces and the scalar ϕ (simply the pressure) in the center of each cell. In other words, the velocities and the pressure are computed at different locations to avoid the checkerboard pattern for the pressure, which may occur when all variables are stored at the same locations.

The second-order central differencing (CD) scheme was employed to approximate the spatial terms. In this scheme that is easy to implement, no matter what the flow direction is, a linear interpolation can be used logically to estimate the values at the control volume faces. Moin (1995) reported that at high Reynolds numbers, applying the CD scheme on the convection terms might lead to instability. Although the instability was never observed in a turbulent channel flow prediction when using periodic boundary conditions and uniform grid, the use of inflow-outflow boundary conditions or of the stretched grid will likely trigger the instability. In order to avoid having that problem, the QUICK (Quadratic Upwind Interpolation for Convective Kinematics) scheme (Leonard, 1979; Neumann et al., 2011) was also implemented into the numerical model to

approximate the convection terms, having in attention that the convection terms become dominant at high Reynolds numbers (Griebel et al., 1998). In fact, the QUICK scheme reduces or removes the instability by adding numerical diffusion (Moin, 1995). According to the QUICK scheme, the velocity at a control volume face is first estimated by a linear interpolation and then corrected by a term proportional to the upstream-weighted curvature, regarding the flow direction.

As an example, a control volume for $u_{i,j}$ and its neighboring nodes are presented in Figure 3.1. The discretization of the convection terms (using the QUICK scheme) and diffusion terms (using the CD scheme) of the momentum equation in the x-direction is written as follows:

$$\begin{aligned}\frac{\partial uu}{\partial x} = \frac{1}{\delta \bar{x}_i}\Bigg[\Bigg\{ {u_e}^2 - \left(\frac{u_e + |u_e|}{2}\right)\left(\frac{{\delta x_{i+1}}^2}{8\,\delta \bar{x}_i}\right)\left(\frac{u_{i+1,j}-u_{i,j}}{\delta x_{i+1}} - \frac{u_{i,j}-u_{i-1,j}}{\delta x_i}\right) \\ - \left(\frac{u_e - |u_e|}{2}\right)\left(\frac{{\delta x_{i+1}}^2}{8\,\delta \bar{x}_{i+1}}\right)\left(\frac{u_{i,j}-u_{i+1,j}}{\delta x_{i+1}} - \frac{u_{i+1,j}-u_{i+2,j}}{\delta x_{i+2}}\right)\Bigg\} \\ - \Bigg\{ {u_w}^2 - \left(\frac{u_w + |u_w|}{2}\right)\left(\frac{{\delta x_i}^2}{8\,\delta \bar{x}_{i-1}}\right)\left(\frac{u_{i,j}-u_{i-1,j}}{\delta x_i} - \frac{u_{i-1,j}-u_{i-2,j}}{\delta x_{i-1}}\right) \\ - \left(\frac{u_w - |u_w|}{2}\right)\left(\frac{{\delta x_i}^2}{8\,\delta \bar{x}_i}\right)\left(\frac{u_{i-1,j}-u_{i,j}}{\delta x_i} - \frac{u_{i,j}-u_{i+1,j}}{\delta x_{i+1}}\right)\Bigg\}\Bigg]\end{aligned} \tag{3.20}$$

$$\begin{aligned}\frac{\partial uv}{\partial y} = \frac{1}{\delta y_j}\Bigg[\Bigg\{ u_n v_n - \left(\frac{v_n + |v_n|}{2}\right)\left(\frac{{\delta \bar{y}_j}^2}{8\,\delta y_j}\right)\left(\frac{u_{i,j+1}-u_{i,j}}{\delta \bar{y}_j} - \frac{u_{i,j}-u_{i,j-1}}{\delta \bar{y}_{j-1}}\right) \\ - \left(\frac{v_n - |v_n|}{2}\right)\left(\frac{{\delta \bar{y}_j}^2}{8\,\delta y_{j+1}}\right)\left(\frac{u_{i,j}-u_{i,j+1}}{\delta \bar{y}_j} - \frac{u_{i,j+1}-u_{i,j+2}}{\delta \bar{y}_{j+1}}\right)\Bigg\} \\ - \Bigg\{ u_s v_s - \left(\frac{v_s + |v_s|}{2}\right)\left(\frac{{\delta \bar{y}_{j-1}}^2}{8\,\delta y_{j-1}}\right)\left(\frac{u_{i,j}-u_{i,j-1}}{\delta \bar{y}_{j-1}} - \frac{u_{i,j-1}-u_{i,j-2}}{\delta \bar{y}_{j-2}}\right) \\ - \left(\frac{v_s - |v_s|}{2}\right)\left(\frac{{\delta \bar{y}_{j-1}}^2}{8\,\delta y_j}\right)\left(\frac{u_{i,j-1}-u_{i,j}}{\delta \bar{y}_{j-1}} - \frac{u_{i,j}-u_{i,j+1}}{\delta \bar{y}_j}\right)\Bigg\}\Bigg]\end{aligned} \tag{3.21}$$

$$\frac{\partial^2 u}{\partial x^2} + \frac{\partial^2 u}{\partial y^2} = \frac{1}{\delta \bar{x}_i}\left[\frac{u_{i+1,j}-u_{i,j}}{\delta x_{i+1}} - \frac{u_{i,j}-u_{i-1,j}}{\delta x_i}\right] + \frac{1}{\delta y_j}\left[\frac{u_{i,j+1}-u_{i,j}}{\delta \bar{y}_j} - \frac{u_{i,j}-u_{i,j-1}}{\delta \bar{y}_{j-1}}\right] \tag{3.22}$$

where subscripts e, w, n and s denote the *east*, *west*, *north* and *south* faces of a control volume, respectively.

An important issue in the spatial discretization is the accuracy of the results on a non-uniform

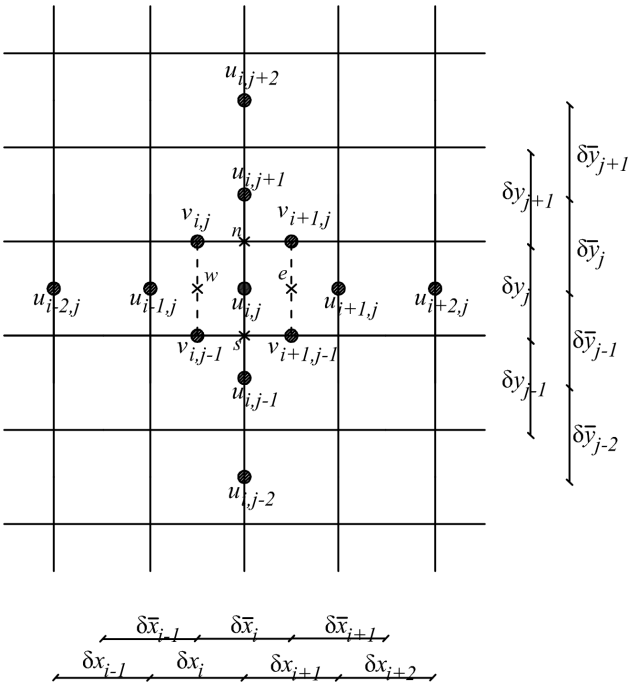

Figure 3.1: Definition of the parameters required for the spatial discretization of the 2-D momentum equation in the x-direction.

grid system. For example, the first derivative of the u-velocity at the grid point i, j is approximated as follows:

$$\frac{\partial u}{\partial x} = \frac{u_e - u_w}{\delta\overline{x}_i} - \frac{\left(\frac{\delta x_{i+1}}{2}\right)^2 - \left(\frac{\delta x_i}{2}\right)^2}{2\delta\overline{x}_i}\frac{\partial^2 u}{\partial x^2} + \mathrm{H} \tag{3.23}$$

where H means “higher order terms”.

The present numerical model uses only the first term on the right-hand side of equation 3.23, while the remaining terms are the truncation error. In a highly non-uniform grid (i.e., $\delta x_{i+1} \gg \delta x_i$), the mentioned approximation may not give a very accurate estimate of u derivative at point i, j. Therefore, the grid expansion ratio ($\delta x_{i+1}/\delta x_i$) should not be allowed to become too large.

3.5 Solving the Poisson equation

In order to solve the implicit Poisson equations 3.11 and 3.16, the Successive Over-Relaxation (SOR) method was adopted for this study as explained by Biringen & Chow (2011). It is a classical iterative method for the approximate solution of a linear equations system that is very simple to

program and can be easily enhanced for parallel computations to speed up solving the system of equations. The algorithm for the SOR method is presented following. A similar procedure can be used for the implicit equations 3.7, 3.14 and 3.17 to obtain the intermediate velocity values.

The arrangement of the parameters for the Poisson equation is shown in Figure 3.2 (left). Applying the SOR method on the 2-D discrete form of the Poisson equation yields:

$$\phi_{i,j}^{\alpha+1} = \frac{\beta}{C_{i,j}} \left\{ \delta y_j \left[u_{i,j}^* - \Delta t \frac{\phi_{i+1,j}^{\alpha}}{\delta \bar{x}_i} - u_{i-1,j}^* - \Delta t \frac{\phi_{i-1,j}^{\alpha+1}}{\delta \bar{x}_{i-1}} \right] \right.$$
$$\left. + \delta x_i \left[v_{i,j}^* - \Delta t \frac{\phi_{i,j+1}^{\alpha}}{\delta \bar{y}_j} - v_{i,j-1}^* - \Delta t \frac{\phi_{i,j-1}^{\alpha+1}}{\delta \bar{y}_{j-1}} \right] \right\} + (1-\beta)\phi_{i,j}^{\alpha} \tag{3.24}$$

where $C_{i,j}$ is a coefficient and α is iteration number. The over-relaxation parameter is denoted by β and a good choice of this parameter ($1 \leq \beta < 2$) can speed up the convergence. $\phi_{i,j}^{\alpha+1}$ represents the $(\alpha+1)^{\text{th}}$ approximation or iteration of $\phi_{i,j}$ at each time step. The iteration should be carried out until the solution is sufficiently accurate. For that, the change in the results from one iteration to the previous was calculated. The computations were repeated at each new time step until that change or difference went below the convergence limit (10^{-5} for the present 2-D calculations).

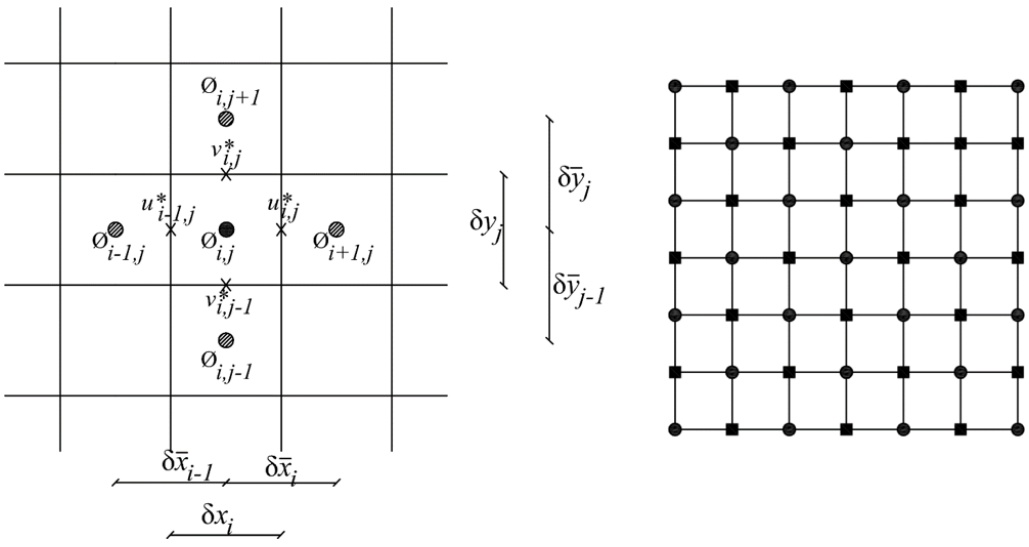

Figure 3.2: left: Staggered grid cell arrangement on 2-D plane for Poisson equation; right: definition of two series of points (*squares* and *circles*) for parallel computing.

It should be noted that for the cells adjacent to the boundaries, equation 3.24 was modified by means of the incorporation of the velocity boundary conditions such that the pressure boundary

condition was not required in the calculations.

The SOR method is inherently sequential in its original form. To take the advantages of the parallel computing, two series of points were defined as pictured in Figure 3.2 (right). In this case, calculations can be performed in two steps (Zhang et al., 2005). The *circle* grid points are connected only to the *square* points and so they can be calculated using the most recent values at the *square* points in a first step. Then, in a second step, the values at the *square* points can be obtained using the most recent values at the *circle* points. Thus, computations in each step can be partitioned into a number of independent tasks and then can be performed in parallel. In this study, parallelization of the numerical calculations was achieved by using Open Multi-Processing (OpenMP) library, which is based on the idea of using multiple processors on a shared memory computer architecture.

3.6 Test case: 2-D unsteady laminar flow around a square cylinder

Two different algorithms were reported in section 3.3, those developed by employing the AB-CN and RK-CN schemes together with a fractional-step method to solve the set of the flow equations. The efficiency of both algorithms was evaluated by considering 2-D unsteady flow past a square cylinder at $\mathrm{Re}_D = 100$, based on the approach velocity and the square side length (D). For that, the numerical models were developed using the finite-difference method in FORTRAN 90/95 programming language. In the following, the computational domain, boundary conditions and important flow quantities in studying the 2-D flow around a square cylinder are first summarized and then the corresponding numerical results are presented and compared taking into account available reference data.

3.6.1 Computational domain and boundary conditions

The computational domain is a rectangular area in the Cartesian coordinate system as shown in Figure 3.3. The origin of the Cartesian coordinate is at the left bottom corner of the domain. Hence, the center of the square cylinder cross-section is located at $x = X_{UP}$ and $y = Y/2$. Inlet boundary section was located $10D$ upstream from the center of the square and the fluid flow, down from this boundary section, was considered to have a specified constant velocity ($u = U_\infty$ and $v =$

0). Domain boundaries in the transverse direction (y), also referred to as the lateral boundaries, were located far away ($10D$) from the square center to remove or reduce extremely probable effects of these boundaries on the flow behavior around the square. The free-slip condition ($\partial u/\partial y = v = 0$) was imposed at the lateral boundaries, while the no-slip condition ($u = v = 0$) was imposed at the square faces. Finally, the convective boundary condition (CBC), equation 3.25 (Sohankar et al., 2000), with zero pressure was used at the outlet boundary section to ensure that vortices can approach and pass the outflow boundary without significant disturbances. However, for this 2-D case, the outlet section was considered sufficiently far away from the square cylinder ($X_{DOWN} = 30D$).

$$\frac{\partial u_i}{\partial t} = U_\infty \frac{\partial u_i}{\partial x} = 0 \tag{3.25}$$

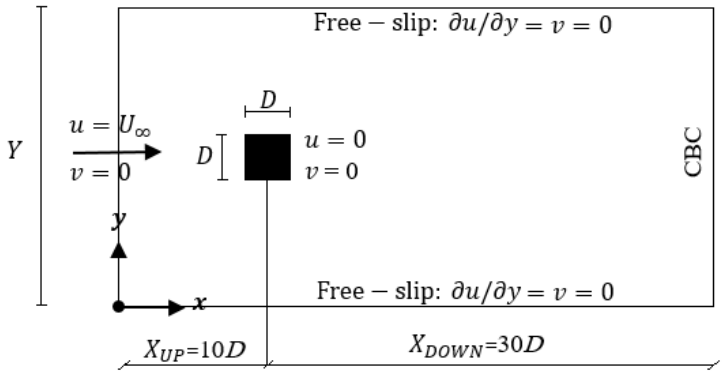

Figure 3.3: Computational domain and boundary conditions, 2-D unsteady laminar flow.

3.6.2 Definition of the integral quantities

The most important non-dimensional parameters of the fluid flow around a cylinder at an unsteady flow regime are the Strouhal number (St), the drag and the lift coefficients (C_D and C_L). The last two mentioned parameters are generally defined by means of the following equations:

$$C_D = \frac{F_D}{0.5\rho U_\infty^2 D}, \qquad C_L = \frac{F_L}{0.5\rho U_\infty^2 D} \tag{3.26}$$

where F_D and F_L are the drag and lift forces, for the present 2-D calculations, computed using the pressure force (F_P). Hence:

$$F_D = \sum F_{P_{west}} - \sum F_{P_{east}} \tag{3.27}$$

$$F_L = \sum F_{P_{north}} - \sum F_{P_{south}} \tag{3.28}$$

where indices denote square sides.

Lift is assumed to have a null mean time value but C_D was averaged over time, an overbar denoting the time averaging ($\overline{C}_D$). Also, the root-mean-square (r.m.s.) of the drag and lift coefficient fluctuations were obtained and are reported in the next section.

The Strouhal number ($St = fD/U_\infty$) is another non-dimensional parameter used in this study and it was obtained by normalization of the vortex shedding frequency ($f = 1/T$, in which T is the vortex shedding period).

Moreover, the stream-function, ψ, was also computed to illustrate the flow structure around the square cylinder. It was obtained using the u-velocity component as follows:

$$\psi_{i,j} = \sum_{m=1}^{j} u_{i,m}\, \delta y_m \tag{3.29}$$

3.6.3 Results and discussion

Several simulations were performed to evaluate the efficiency of the semi-implicit schemes, all using the same grid with a zone inside the square geometry where the grid is uniform in both x- and y- directions (a minimum cell size, a_1= 0.05D). The grid size was enlarged gradually as the distance from the square faces increases. In order to minimize the error reported in section 3.4 (equation 3.23), the expansion ratio of the grid cells (in the non-uniform part) was set close to unity ($\sim$1.01), resulting in a total number of grid cells about 85000 (344$\times$246). The corresponding calculations were performed, employing 8 processors in parallel, until a specific finish time defined as 50T. Moreover, the QUICK scheme was selected to approximate the convection terms.

The unsteady flow structure around the square cylinder, obtained by using the AB-CN scheme, is shown in Figure 3.4 by means of mapping the instantaneous streamlines near the square at

different time moments, separated by an interval of $1/8T$. From those, it can be concluded that the vortex that is formed at downstream edges of the square, grows progressively in time until it breaks off. This vortex shedding phenomenon affects the pressure distribution around the square, which leads to a periodic variation in the drag and lift forces acting on the square. The corresponding time-dependent drag and lift coefficients are presented in Figure 3.5, indicating that the frequency of the drag coefficient is twice the one of the lift coefficient and that agrees with that reported by Sumer & Fredsøe (1997).

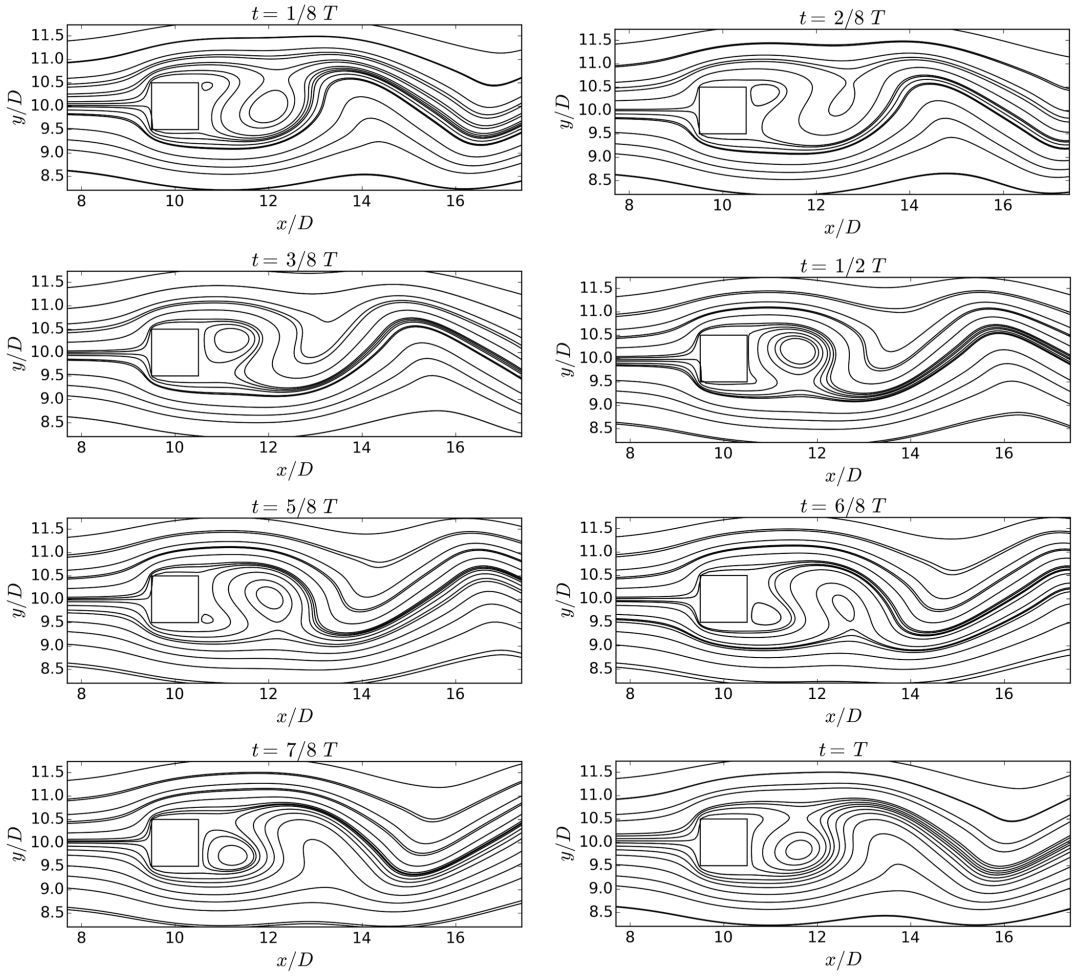

Figure 3.4: Instantaneous streamlines around the square cylinder during one vortex shedding period (T): (QUICK, AB-CN scheme, Re_D = 100).

The corresponding non-dimensional flow parameters are presented in Table 3.1 together with the numerical results reported by Sohankar et al. (1998) and Sharma & Eswaran (2004). According to Table 3.1, the mean drag coefficient and the Strouhal number obtained in this study are in

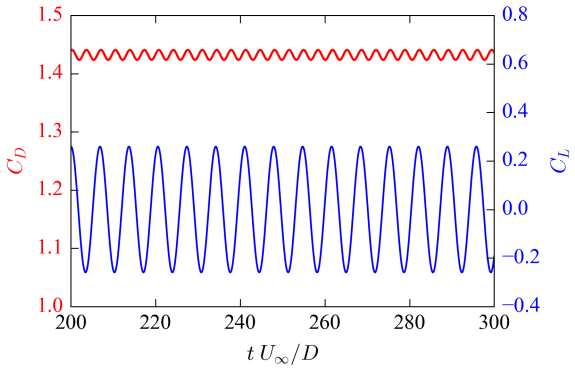

Figure 3.5: Time variation of the drag (red line) and lift (blue line) coefficients for a square cylinder at Re_D = 100 (QUICK, AB-CN scheme).

good agreement with those reported by the referenced researchers, with an error less than 2%. A difference is observed between the results obtained concerning the r.m.s. of the lift and drag coefficient fluctuations that might be due to differences in the size of the grid cells close to the square faces (a_1). In fact, Sharma & Eswaran (2004) reported that the value of $\mathrm{C_L}$ r.m.s., compared to the other non-dimensional parameters, is largely influenced by a_1. Although a relatively coarser grid was used in this study compared to that in the referenced studies, the mean drag coefficient and the Strouhal number could well be predicted and hence, the grid resolution was considered fine enough for the present comparison study between the AB-CN and RK-CN schemes.

Table 3.1: Comparison between non-dimensional parameters obtained from different studies, Re_D = 100.

Reference	Scheme	a_1/D	$\overline{\mathrm{C}}_\mathrm{D}$	$\mathrm{C_D}$ r.m.s.	$\mathrm{C_L}$ r.m.s.	St
Present Study (AB-CN)	QUICK	0.05	1.432	0.006	0.184	0.146
Sohankar et al. (1998)	QUICK	0.004	1.434	—	0.153	0.146
Sharma & Eswaran (2004)	QUICK	0.01	1.445	0.0055	0.193	0.149
Present Study (AB-CN)	CD	0.05	1.398	0.0053	0.171	0.148

In order to investigate the effect of the discretization scheme on the results, Table 3.1 shows also the non-dimensional parameters obtained by applying the CD scheme on the convection terms. By comparing those with the results obtained by the QUICK scheme, one can clearly see that the results can not be considered fully similar. Except for the Strouhal number, the CD scheme presented lower values for the non-dimensional parameters than the QUICK scheme. Ac-

curacy and adequacy of the CD and QUICK schemes were further investigated and that will be referred in the next chapters of the present thesis.

As mentioned earlier in section 3.3, the RK scheme allows using a larger time-step size than the AB scheme. Therefore, the effect of the time-step size on the results was investigated in this study by employing the RK-CN scheme. For this purpose, the 2-D flow around the square cylinder was also predicted by means of the RK-CN scheme (using the QUICK scheme) for different time-step size values and compared with those obtained by the AB-CN scheme. The corresponding time-averaged dimensionless u-velocity values at the wake centerline are presented in Figure 3.6, indicating that those are the same for different time-step sizes (in this figure, the time-step sizes were presented in the form of the CFL number as defined in section 3.3). In order to broaden the comparison zone, the corresponding distributions of the time-averaged velocity magnitude ($\left|\overline{U}\right| = \sqrt{\bar{u}^2 + \bar{v}^2}$) around the square cylinder are presented in Figure 3.7. Again, no noticeable difference was observed between the results obtained by means of the AB-CN scheme (CFL = 0.4) and the RK-CN scheme (CFL = 1.0). Further, the corresponding time-averaged streamlines are presented in Figure 3.8. At Re_D = 100, the flow separates at the trailing edge and reattaches at a short distance downstream of the square. Hence, the recirculation length (L_r) is defined as the longitudinal distance from the rear of the square to the re-attachment point along the wake centerline. The corresponding dimensionless length (L_r/D) value obtained for different time-step sizes was equal to 1.91, in accordance with the value reported by Sharma & Eswaran (2004). Overall, within the used time-steps range, the AB-CN and RK-CN schemes led to the time-averaged results nearly independent of the time-step size.

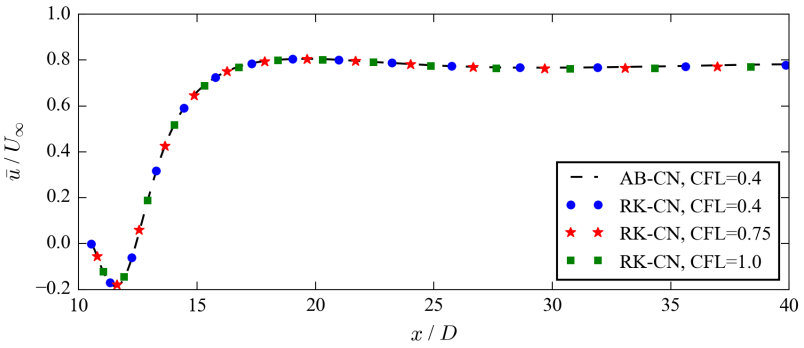

Figure 3.6: Time-averaged of the u-velocity values obtained by AB-CN and RK-CN schemes using different time-step sizes, QUICK scheme, Re_D= 100 (downstream of the square, symmetry line).

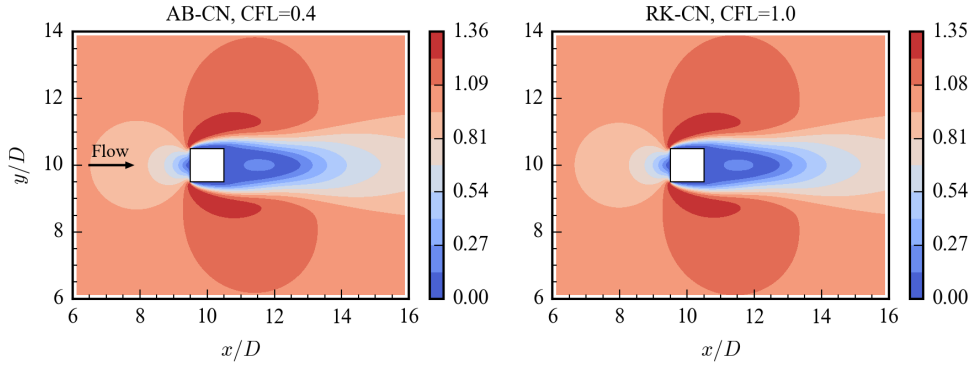

Figure 3.7: Distributions of the time-averaged velocity magnitude ($\sqrt{\bar{u}^2+\bar{v}^2}/U_\infty$) around the square cylinder obtained by AB-CN and RK-CN schemes using different time-step sizes, QUICK scheme, Re_D = 100.

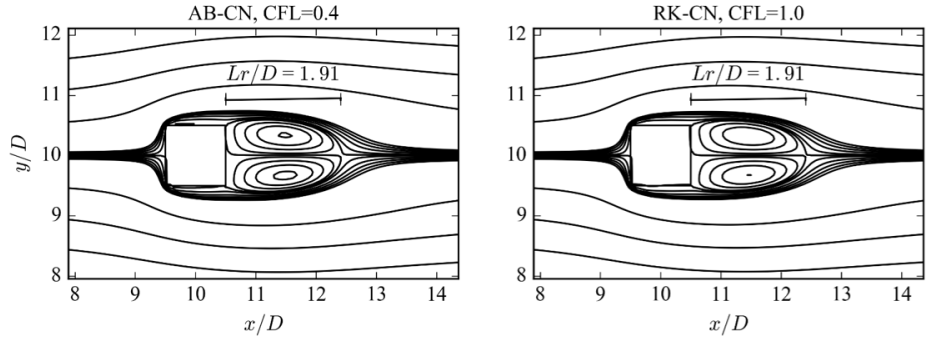

Figure 3.8: Time-averaged streamlines around the square cylinder obtained by AB-CN and RK-CN schemes using different time-step sizes, QUICK scheme, Re_D = 100 (L_r is defined as the recirculation length).

The computational time (CPU time) was also assessed for different time-step sizes, as reported in Table 3.2. Performed simulations showed that the number of inner iterations, for computing the scalar ϕ (details in section 3.5), increases with increasing the time-step size. Hence, the elapsed time due to the RK-CN calculations at CFL = 1.0 was found to be nearly equal to the one due to the AB-CN calculations at CFL = 0.4. Therefore, increasing the time-step size, by means of the RK scheme, could not decrease the total CPU time based on the methods used in this study.

Finally, two of those simulations, AB-CN (CFL = 0.4) and the RK-CN (CFL = 1.0), were restarted just for one time-step using the results previously obtained as initial data. As mentioned earlier in section 3.3, the solution algorithm at each time step is divided into three sections: (1) calculation of the intermediate velocities, (2) computation of the scalar quantity ϕ and (3) update

Table 3.2: Comparison between CPU times spent for different time-step sizes, QUICK scheme, $Re_D = 100$.

Scheme	CFL	CPU time (s)
AB-CN	0.4	2173
RK-CN	0.4	4984
RK-CN	0.75	3160
RK-CN	1.0	2467

of the velocity field. The CPU time corresponding to each of those three sections, for only one time-step, is presented in Figure 3.9. Both the AB-CN and RK-CN schemes used most of the CPU time for calculating the intermediate velocity field, largely due to the implicit treatment of the diffusion terms. For the implicit treatment, equations 3.7, 3.14 and 3.17 were rearranged into the form of a linear equation and the right-hand side of the rearranged equation was computed using the values from the previous time steps. Then, the intermediate velocity field was obtained by solving the linear equation system using an iterative method. During the iterative procedure, the intermediate velocities were updated at the flow boundaries.

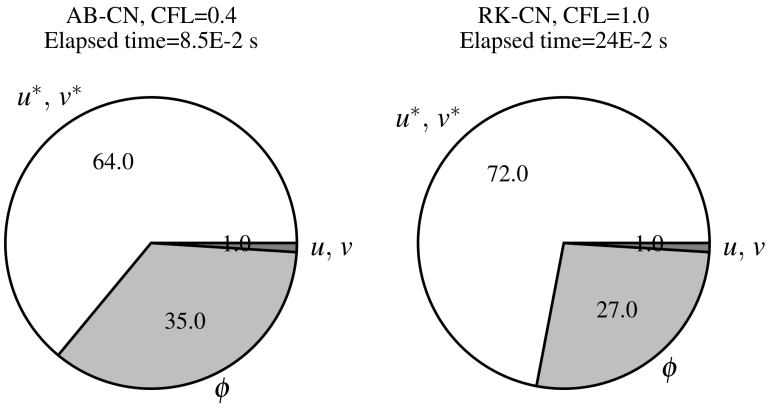

Figure 3.9: Division of the CPU time to compute the intermediate velocity field, the scalar ϕ (simply the pressure) and the velocity field for one time step, QUICK scheme, $Re_D = 100$.

3.7 Conclusions

The flow equations set, including the continuity and Navier-Stokes equations, were solved in the framework of the fractional-step method by employing two different semi-implicit schemes: (*i*)

Adams-Bashforth and Crank-Nicolson (AB-CN), and (*ii*) Runge-Kutta and Crank-Nicolson (RK-CN). Both schemes could properly predict 2-D unsteady laminar flow around a square cylinder at Re_D =100. Analysis of the corresponding results yielded:

- Choosing the spatial discretization scheme was observed to affect the results. The mean drag coefficient and the r.m.s. values of lift and of drag coefficient fluctuations obtained by means of the CD scheme were smaller than those obtained by means of the QUICK scheme, while the Strouhal number obtained by the former was bigger than those obtained using the latter scheme. Nevertheless, both schemes were adopted for the numerical model development and those will be further evaluated in the next chapters.

- Effect of the time-step size on the accuracy of the results was investigated in this study. For this purpose, according to the stability limit of each semi-implicit scheme, unsteady flow around the square cylinder was predicted by means of the AB-CN scheme for CFL = 0.4 and also by means of the RK-CN scheme for CFL = 0.4, 0.75 and 1.0. Both schemes presented similar time-averaged results for all the CFL numbers mentioned above. In terms of the CPU time, the elapsed time for the AB-CN calculations at CFL = 0.4 was found to be nearly equal to the one due to the RK-CN calculations at CFL = 1.0. Therefore, increasing the time-step size by means of the RK scheme, compared to the AB scheme, could not decrease the total CPU time in this study and hence the AB scheme was selected for further studies in the next chapters.

CHAPTER 4

Modeling Turbulent Flows

4.1 Introduction

In the previous chapter, the solution methods for the flow equations set were evaluated by considering a 2-D laminar flow around the square cylinder. However, the flow around a bridge pier is mostly turbulent and 3-D.

The most accurate method for predicting the turbulent flow is the Direct Numerical Simulation (DNS) method, which uses the flow equations directly. This means that all turbulent scales must be resolved temporally and spatially. The CPU-cost of performing a 3-D simulation using DNS increases at a rate proportional to the third power of the Reynolds number (Tremblay, 2001), meaning that the computational cost of the DNS method (for modeling turbulent flows) is high,

even by employing powerful computers available today. DNS computations are thus limited to low Reynolds number problems, which is limiting for the majority of engineering applications.

In contrast to the DNS method, unsteady Reynolds Averaged Navier-Stokes (RANS) equations are widely used in CFD. In this method, each instantaneous flow quantity (i.e., pressure and velocity field) is decomposed into its time-averaged and fluctuating components. The turbulent fluctuations are averaged over time and represented by the Reynolds stress terms what requires a separate modeling by a turbulence model (e.g., K-ε turbulence model, in which K represents the turbulent kinetic energy and ε denotes its dissipation rate). This method is more economical (in computational time) than DNS but its main disadvantage is that it is not able to reasonably reproduce the unsteady flow features past a bluff body (Rodi, 1997; Breuer et al., 2003).

Another way to overcome the high cost of the DNS method is to use the LES model. In this model, a filtering procedure (grid filtering) is used to decompose each flow quantity into large-scale and small-scale components. The large-scales are calculated directly and the effect of the small-scales is modeled by using a subgrid-scale model. Recently, Lysenko et al. (2012) simulated the flow around a circular cylinder using the LES model at $\mathrm{Re}_D = 3900$ by employing 5.76 million computational cells in such a way that the first computational point close to the cylinder wall surface was located in the viscous sub-layer to get wall-resolved results (also known in the literature as fully-resolved LES). The integration time was about 150 vortex shedding periods (T) to obtain a fully converged mean flow field and the corresponding CPU time was about 226 hours by employing 256 processors in parallel. More recently, Kim et al. (2015) simulated the turbulent flow around a circular cylinder at $\mathrm{Re}_D = 41300$ through the fully-resolved LES by using about 5 million computational cells. The time-averaged flow data were obtained for about $30T$ and the corresponding CPU time was about 360 hours by employing 96 processors in parallel. Overall, although the application of the LES model reduces the computational cost compared to the use of the DNS method, still a fully-resolved LES requires a large computational effort for engineering applications.

In order to reduce the CPU time, wall models can be employed in the solution. In this case, the near-wall region is replaced by a wall model and by that the first computational point close to the wall can be located out of the viscous sub-layer and the buffer-layer. Wang (1999) reported

that the total reduction in CPU time by the joint use of the LES model and a wall model compared to the sole use of the LES model (fully-resolved LES) is over 90%.

Over the last years, wall models based on the boundary layer approximations have been developed and widely used together with the LES model. The methodology is known as the Two-Layer approach in which the boundary layer equations are numerically solved on a grid, refined in the wall-normal direction. The boundary layer equations are a simplified set of partial differential equations derived from the Navier–Stokes equations. These equations are forced at the outer boundary by the instantaneous tangential velocities obtained from the LES model, while the no-slip condition is applied at the wall boundary. Wang & Moin (2002) compared full boundary layer equations and their simpler variants by simulating the turbulent flow past an asymmetric trailing-edge. Two simple forms were introduced either (1) by considering diffusion and pressure terms or (2) by considering only the diffusion term, from the boundary layer equations. They found that the skin-friction coefficients predicted by using the simplified forms are less accurate than those obtained by solving the full boundary layer equations in the region of strong pressure gradients. Recently, Posa & Balaras (2014) employed the boundary layer equations for a low Reynolds number case and concluded that if the first computational point close to the wall is positioned within the boundary layer, the transient and convection terms (in the boundary layer equations) can be neglected in the solution without significant errors.

It is noteworthy to mention that, during the last years, the Detached Eddy Simulation (DES) method has been developed aiming at reducing the large computational resources required for the LES calculations. This method is based on the idea of using the RANS equations to simulate the near-wall region and the LES model out of that flow region. An advantage of this method is the possibility to employ proper turbulence models in different regions. Nevertheless, Chen (2011) noted that the computational cost of the Hybrid LES-RANS (DES method) is much higher than using the LES model with the boundary layer equations as the full flow equations must be solved all the way down to the wall.

In addition to the wall model, numerical approaches for the turbulent flow predictions are also important factors to obtain the appropriate results with low computational cost. For example, a fundamental challenge for computing the eddy-viscosity (also known as the turbulent viscosity)

in the LES subgrid-scale model is to provide information concerning the unresolved scales or small-scale components. That information can be predefined in a simulation (e.g., by means of the parameters in the Smagorinsky model (Smagorinsky, 1963)) or can be dynamically adjusted in time and space during the simulation. It should be noted that, in the case of using a dynamic procedure, a test-filter (different from the grid-filter) should be applied in the solution and that increases the CPU time when compared to the use of the Smagorinsky model. Lysenko et al. (2012) reported that using the Smagorinsky model is about 20% more efficient compared to the use of a dynamic model (namely K-equation eddy-viscosity model). However, Beaudan & Moin (1994) compared the Smagorinsky model with the least-squares version of the dynamic eddy viscosity model by considering the turbulent flow around a circular cylinder at $\mathrm{Re}_D = 3900$ and noticed that the dynamic model is overall more accurate than the Smagorinsky model. Nevertheless, Kravchenko & Moin (2000) analyzed the results presented by Beaudan & Moin (1994) and could conclude that the comparative model's accuracy differences were in fact not significant.

The objective of this chapter is to study the applicability of the LES Smagorinsky model together with the Two-Layer approach in order to predict the turbulent flow behavior around bluff bodies. For that, a simple form of the boundary layer equations (by considering only the diffusion and pressure terms) was employed to approximate the wall shear stress components in the solution. The performance of the Smagorinsky subgrid-scale model was investigated by considering different values for the Smagorinsky coefficient and different definitions for computing the spatial filter width (the so-called predefined parameters). The test cases selected are (*i*) the flow past an infinite-length square cylinder at $\mathrm{Re}_D = 20000$ and (*ii*) the flow past an infinite-length circular cylinder at $\mathrm{Re}_D = 3900$. The cases have been previously investigated in different studies, experimentally and numerically, and the corresponding results are available for the present comparison study.

In the following, the grid structures, boundary conditions and details of the numerical models are first summarized and then the corresponding numerical results are presented and compared with available reference data.

4.2 Test cases: 3-D turbulent flow past a square and a circular cylinder

4.2.1 Grid structures and boundary conditions

To model the square cylinder geometry, a computational domain in the Cartesian coordinate system was used as shown in Figure 4.1 a). The origin of the Cartesian coordinate was at the left bottom corner of the domain. The square center was located $10D$ (X_{UP}) downstream from the inlet boundary section and $20D$ (X_{DOWN}) upstream from the outlet boundary section. These domain dimensions were selected regarding the numerical studies done by Sohankar et al. (2000) (X_{UP} = $7.9D$ and X_{DOWN} = $16.3D$); Minguez et al. (2011) (X_{UP} = $4.5D$ and X_{DOWN} = $15D$) and Trias et al. (2015) (X_{UP} = $10.5D$ and X_{DOWN} = $20D$) for the same inflow-outflow boundary conditions as used in this LES study. Details of those conditions are presented at the end of this section. The lateral domain boundaries were located $10D$ away from the square center. In the vertical direction, the computational domain length (L_z) was set as equal to πD as considered by Trias et al. (2015) and the grid points were distributed uniformly in that direction. In fact, Trias et al. (2015) reported that L_z must be long enough to ensure that turbulent fluctuations are uncorrelated at a separation length of one half-period, $L_z/2$. Concerning the horizontal xy plane, a uniform mesh was first defined inside the square cross-section and then the mesh grid size was enlarged gradually as the distance from the square faces increases. The resulting grid is finer near the square cylinder faces and progressively coarser out of it.

The numerical simulations for the circular cylinder were performed by employing an O-type mesh in planes perpendicular to the vertical direction. A disadvantage of the mentioned mesh type was reported by Mittal & Balachandar (1996): a sharp variation of the flow velocity was observed at the junction of the inflow and outflow sections, although this discontinuity was reported to be fairly small in magnitude compared to the inflow velocity. Nevertheless, the O-type mesh has been successfully employed by many researchers to model the turbulent flow around a circular cylinder (Breuer, 1998; Kravchenko & Moin, 2000; Mani et al., 2009; Lysenko et al., 2012; Kim et al., 2015). The O-type computational domain, used in this study, is shown in Figure 4.1 b). The origin of the domain is at the center of the circular cross-section. The computational domain has a radius

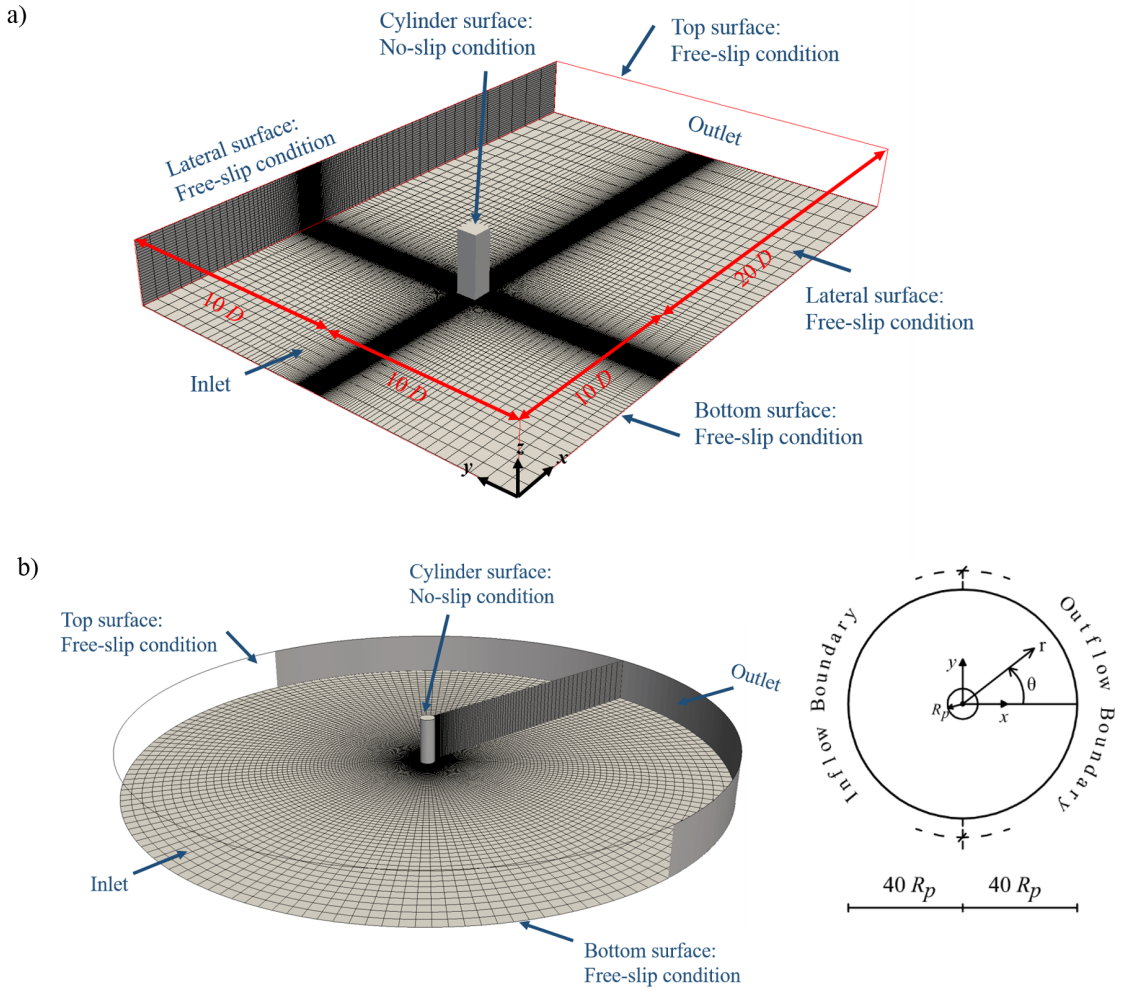

Figure 4.1: Computational domains, coordinate systems and boundary conditions: a) Infinite square cylinder case; and b) Infinite circular cylinder case.

of $40R_P$ (R_P: cylinder radius) which is in the range of $30R_P$ and $50R_P$ used by Kim et al. (2015) and Lysenko et al. (2012), respectively. In addition, the length of the computational domain in the vertical direction was defined as equal to $2\pi R_P$ as considered by Kravchenko & Moin (2000) and Lysenko et al. (2012) for the same Re_D as considered in this LES study. The grid points locations in the radial direction ($R_P \leq r_i \leq R_D$) were defined as

$$r_i = R_P\, e^{2\pi\xi_i}, \qquad \Delta\xi_i = \xi_i - \xi_{i-1} = \Delta\xi_{i+1} \tag{4.1}$$

where R_D is the radius of the computational domain and ξ is a non-dimensional parameter. Moreover, equation 4.2 was used to define the grid points locations in the azimuthal direction θ based on the radial cell width close to the circular cylinder surface (Δr_1). In the case $\eta \approx 1$, the proposed method produces nearly square cell faces in the horizontal $r\theta$ plane. Finally, in the vertical direction, the grid points were distributed uniformly.

$$\Delta\theta_j \, R_P = \eta_j \, \Delta r_1 \tag{4.2}$$

Concerning the boundary conditions, a specified constant inflow velocity ($u = U_\infty$ and $v = w = 0$) was considered at the inlet boundary section and the convective boundary condition, equation 3.25, was employed at the outlet boundary section. The free-slip condition was imposed at the lateral domain surfaces (only for the square cylinder case) and the no-slip condition at the cylinder faces (both cases). Finally, the free-slip or symmetry condition was used at the top and bottom boundaries to reduce the extent of the computational domain (cylinders with infinite length) to the symmetric subsection, justifying a sensitivity analysis on the vertical domain length which was performed in this study.

4.2.2 Governing equations and solution methods

The space-filtered Navier-Stokes (or momentum) and continuity equations, for incompressible fluids, in the Cartesian coordinate system are following presented:

$$\frac{\partial u_i}{\partial t} = -\frac{\partial u_i u_j}{\partial x_j} - \frac{1}{\rho}\frac{\partial \phi}{\partial x_i} + \vartheta \frac{\partial^2 u_i}{\partial {x_j}^2} + \frac{\partial (\vartheta_t S_{ij})}{\partial x_j} \tag{4.3}$$

$$\mathrm{div}(u_i) = \frac{\partial u_i}{\partial x_i} = 0 \tag{4.4}$$

Here ϕ, pseudo-pressure, is the sum of the filtered pressure (p) and a subgrid-scale stress tensor τ_{kk}:

$$\phi = p + \frac{1}{3}\tau_{kk} \tag{4.5}$$

It is to be noted that a subgrid-scale model, equation 4.6, has been implemented in the Navier-Stokes equations.

$$\frac{1}{\rho}\tau_{ij} - \frac{1}{3}\frac{1}{\rho}\tau_{kk}\delta_{ij} = -\vartheta_t S_{ij} \tag{4.6}$$

where δ_{ij} is the Kronecker delta, which is equal to 1 if $i = j$ and 0 otherwise. $S_{ij} = S_{ji}$ is the strain rate tensor, defined as follows:

$$S_{ij} = \frac{\partial u_i}{\partial x_j} + \frac{\partial u_j}{\partial x_i} \tag{4.7}$$

The corresponding space-filtered Navier-Stokes and continuity equations in the cylindrical coordinate system read:

$$\begin{aligned}
\frac{\partial u_r}{\partial t} &= H_r + B_r - \frac{1}{\rho}\frac{\partial \phi}{\partial r} + \vartheta\left\{\frac{1}{r}\frac{\partial}{\partial r}\left(r\frac{\partial u_r}{\partial r}\right) + \frac{1}{r^2}\frac{\partial^2 u_r}{\partial \theta^2} + \frac{\partial^2 u_r}{\partial z^2} - \frac{u_r}{r^2} - \frac{2}{r^2}\frac{\partial u_\theta}{\partial \theta}\right\} \\
&\quad + \frac{1}{r}\frac{\partial}{\partial r}(\vartheta_t r S_{rr}) + \frac{1}{r}\frac{\partial}{\partial \theta}(\vartheta_t S_{r\theta}) + \frac{\partial}{\partial z}(\vartheta_t S_{rz}) - \frac{\vartheta_t S_{\theta\theta}}{r} \\
\frac{\partial u_\theta}{\partial t} &= H_\theta + B_\theta - \frac{1}{r\rho}\frac{\partial \phi}{\partial \theta} + \vartheta\left\{\frac{1}{r}\frac{\partial}{\partial r}\left(r\frac{\partial u_\theta}{\partial r}\right) + \frac{1}{r^2}\frac{\partial^2 u_\theta}{\partial \theta^2} + \frac{\partial^2 u_\theta}{\partial z^2} - \frac{u_\theta}{r^2} + \frac{2}{r^2}\frac{\partial u_r}{\partial \theta}\right\} \\
&\quad + \frac{1}{r}\frac{\partial}{\partial r}(\vartheta_t r S_{\theta r}) + \frac{1}{r}\frac{\partial}{\partial \theta}(\vartheta_t S_{\theta\theta}) + \frac{\partial}{\partial z}(\vartheta_t S_{\theta z}) + \frac{\vartheta_t S_{\theta r}}{r} \\
\frac{\partial u_z}{\partial t} &= H_z - \frac{1}{\rho}\frac{\partial \phi}{\partial z} + \vartheta\left\{\frac{1}{r}\frac{\partial}{\partial r}\left(r\frac{\partial u_z}{\partial r}\right) + \frac{1}{r^2}\frac{\partial^2 u_z}{\partial \theta^2} + \frac{\partial^2 u_z}{\partial z^2}\right\} + \frac{1}{r}\frac{\partial}{\partial r}(\vartheta_t r S_{zr}) \\
&\quad + \frac{1}{r}\frac{\partial}{\partial \theta}(\vartheta_t S_{z\theta}) + \frac{\partial}{\partial z}(\vartheta_t S_{zz})
\end{aligned} \tag{4.8}$$

$$\mathrm{div}(u_i) = \frac{1}{r}\frac{\partial (r u_r)}{\partial r} + \frac{1}{r}\frac{\partial u_\theta}{\partial \theta} + \frac{\partial u_z}{\partial z} = 0, \qquad i = 1,\ 2 \text{ and } 3 \tag{4.9}$$

The first of the terms on the right-hand side of equation 4.8 are the so-called convection terms, which are defined as:

$$H_i = -\frac{1}{r}\frac{\partial (r u_r u_i)}{\partial r} - \frac{1}{r}\frac{\partial (u_\theta u_i)}{\partial \theta} - \frac{\partial (u_z u_i)}{\partial z}, \qquad i = 1,\ 2 \text{ and } 3 \tag{4.10}$$

where r, θ and z represent the radial, azimuthal and vertical directions, respectively. In the cylindrical system, subscripts 1, 2, and 3 are used to denote the mentioned directions.

The second of those terms, B_r and B_θ, correspond respectively to the centrifugal and Coriolis forces due to the curvature of the coordinate system:

$$B_r = \frac{{u_\theta}^2}{r}, \quad B_\theta = -\frac{u_r u_\theta}{r} \tag{4.11}$$

$S_{ij} = S_{ji}$ is the strain rate tensor and, in the cylindrical coordinate system, the tensor elements are defined as:

$$\begin{aligned} S_{rr} &= 2\frac{\partial u_r}{\partial r}, & S_{r\theta} &= \frac{\partial u_\theta}{\partial r} + \frac{1}{r}\frac{\partial u_r}{\partial \theta} - \frac{u_\theta}{r}, & S_{rz} &= \frac{\partial u_r}{\partial z} + \frac{\partial u_z}{\partial r} \\ S_{\theta\theta} &= 2\left(\frac{1}{r}\frac{\partial u_\theta}{\partial \theta} + \frac{u_r}{r}\right), & S_{\theta z} &= \frac{\partial u_\theta}{\partial z} + \frac{1}{r}\frac{\partial u_z}{\partial \theta}, & S_{zz} &= 2\frac{\partial u_z}{\partial z} \end{aligned} \tag{4.12}$$

The terms on the right-hand side of the Navier-Stokes equations 4.3 and 4.8 which are multiplied by ϑ (kinematic viscosity), embody the diffusion terms and the terms including ϑ_t (eddy viscosity) relate to the subgrid-scale model (equation 4.6). Although ϑ_t can be assigned from different theories (e.g., Smagorinsky, wall-adapting local eddy-viscosity and dynamic models (Mueller, 2012)), for this study, the Smagorinsky model (Smagorinsky, 1963) was employed. The reason for that choice is the corresponding low computational cost compared to a dynamic procedure (Tremblay, 2001). Furthermore, dynamic models are computationally sensitive and may introduce instabilities in the solution (Mueller, 2012). Based on the Smagorinsky model, the eddy viscosity can be computed through a mixing length (L_s) and the strain rate tensor as follows:

$$\vartheta_t = {L_s}^2 \left(\frac{1}{2} S_{ij} S_{ij}\right)^{0.5} \tag{4.13}$$

$$L_s = \mathrm{Cs}\, \Delta\, \mathrm{D_f} \tag{4.14}$$

The spatial filter width was denoted by Δ and computed from different definitions as:

$$\Delta^3 = \delta_x\, \delta_y\, \delta_z \tag{4.15}$$

$$\Delta^2 = {\delta_x}^2 + {\delta_y}^2 + {\delta_z}^2 \tag{4.16}$$

where δ_x, δ_y and δ_z are the grid cell sizes (the spatial filter widths) in the subscript directions. Cs is the Smagorinsky coefficient and should be specified prior to a simulation. For many researchers, as reported by Zou et al. (2008), the corresponding range of 0.1-0.14 was found to yield good results. The Van Driest wall damping function, $\mathrm{D_f}$, was also introduced in equation 4.14 to guarantee that the eddy viscosity is reduced near the wall surface (Breuer, 1998).

$$\mathrm{D_f} = \sqrt{1 - \exp\left[-\left(\frac{y^+}{25}\right)^3\right]} \tag{4.17}$$

where y^+ is the non-dimensional wall distance defined as:

$$y^+ = \frac{\rho\, y_c\, u_*}{\mu} \tag{4.18}$$

where y_c is the cell center normal distance to the wall and u_* is the friction velocity that is related to the wall shear stress ($\tau_w = \rho u_*^2$).

Approximate boundary conditions were imposed at the wall boundaries in terms of the wall shear stress components τ_{wi} estimated based on the boundary layer equations (Wang & Moin, 2002; Catalano et al., 2003) as follows.

$$\frac{\partial}{\partial x_2}(\vartheta + \vartheta_t)\frac{\partial u_i}{\partial x_2} = \frac{1}{\rho}\frac{\partial p}{\partial x_i}, \qquad i = 1 \text{ and } 3 \tag{4.19}$$

Here $i = 1$ and 3 represent directions parallel to the wall and $i = 2$ denotes the wall normal direction.

Since the pressure is assumed x_2-independent in the thin wall layer and obtained from the outer flow layer (LES calculations), the tangential velocity components at the first velocity point next to the wall (u_i, i = 1 and 3) can be related to the corresponding wall shear stress components as follows:

$$\tau_{wi} = \frac{\rho}{\int_0^{x_{2C}} \frac{\mathrm{d}x_2}{(\vartheta+\vartheta_t)}}\left(u_i - \frac{1}{\rho}\frac{\partial p}{\partial x_i}\int_0^{x_{2C}} \frac{x_2}{(\vartheta+\vartheta_t)}\mathrm{d}x_2\right) \tag{4.20}$$

where x_{2C} is the normal distance from the first tangential velocity node to the wall surface.

In order to solve equation 4.20, the eddy viscosity definition is required from point x_{2C} down to the wall (inner layer or wall layer). In this study, that was estimated from a mixing length model with a near-wall damping function as adopted by Wang & Moin (2002) and Catalano et al. (2003):

$$\vartheta_t = \vartheta \, \mathrm{k} \, y^+ \left[1 - \exp\left(-\frac{y^+}{19}\right)\right]^2 \tag{4.21}$$

Catalano et al. (2003) considered k as the von Kármán constant, while Wang & Moin (2002) reported that Cabot & Moin (2000) suggested to compute it dynamically by matching the stresses between the inner layer and the outer layer solutions. In the present study, k was considered as the von Kármán constant (k = 0.4). Furthermore, in order to compute y^+ and then ϑ_t in equation 4.21, the friction velocity that depends on the wall shear stress given by equation 4.20, is required. Hence, an iterative procedure was implemented to solve equations 4.20 and 4.21 simultaneously. However, Wang & Moin (2002) suggested estimating the friction velocity using the instantaneous τ_{wi} values from the previous time step.

The spatial discretization of the governing equations was performed on the staggered grid system. In general, the QUICK scheme was adopted for discretization of the convection terms and the CD scheme for the remaining terms as used by Paone et al. (2016) to achieve a stable LES simulation around a circular cylinder on a relatively coarse mesh. However, concerning the approximation of the convection terms, Einian (2012) reported that the QUICK upwind scheme is relatively diffusive and thus used the CD scheme in the square-cylinder wake region. It should be noted that the numerical calculations of Einian (2012) were performed using the fully-resolved LES (i.e., using fine mesh in the wake region), while for the joint use of the LES and a wall model (e.g., Paone et al. (2016) and present study), the grid is relatively coarse and applying the CD scheme on the convection terms might lead to inaccurate results. Nevertheless, both scenarios were examined in the present study. The circular cylinder case was investigated by employing only the QUICK scheme to approximate the convection terms, while the square cylinder case was studied by using both the QUICK and CD schemes in such a way that the CD zone covers the recirculation regions that exist downstream and at the lateral sides of the square cylinder.

For the temporal discretization, the momentum equations 4.3 and 4.8 were split and three operators (M, N and P) were defined such that the M operator was treated explicitly by the second-order

Adams-Bashforth (AB) scheme and the N operator was treated implicitly by the second-order Crank-Nicolson (CN) scheme. Applying the semi-implicit AB-CN scheme on the momentum equations resulted in the following equation:

$$\frac{{u_i}^{n+1} - {u_i}^n}{\Delta t} = \frac{1}{2}\left[3\mathrm{M}\left({u_i}^n\right) - \mathrm{M}\left({u_i}^{n-1}\right)\right] + \frac{1}{2}\left[\mathrm{N}\left({u_i}^{n+1}\right) + \mathrm{N}\left({u_i}^n\right)\right] - \mathrm{P}_i\left(\phi^{n+1}\right) \tag{4.22}$$

where the P operator is related to the pseudo-pressure term (simply referred to as the pressure term).

The N operator was defined as equation 4.23 and the remaining terms on the right-hand side of the momentum equations were considered as the M operator.

$$\begin{aligned} \mathrm{N}\left(u_i\right) &= \vartheta\ \nabla^2 u_i = \vartheta \left\{\frac{\partial^2 u_i}{\partial {x_j}^2}\right\}, && \text{Cartesian system} \\ \mathrm{N}\left(u_i\right) &= \vartheta\ \nabla^2 u_i = \vartheta \left\{\frac{1}{r}\frac{\partial}{\partial r}\left(r\frac{\partial u_i}{\partial r}\right) + \frac{1}{r^2}\frac{\partial^2 u_i}{\partial \theta^2} + \frac{\partial^2 u_i}{\partial z^2}\right\}, && \text{Cylindrical system} \end{aligned} \tag{4.23}$$

Regarding which momentum terms were treated explicitly and which terms were treated implicitly, the following definition was adopted for the stability criterion (Moin, 1995):

$$\begin{aligned} \mathrm{SC} &= \Delta t \left\{\frac{|u|}{\delta x} + \frac{|v|}{\delta y} + \frac{|w|}{\delta z} + 4\ \vartheta_t \left(\frac{1}{(\delta x)^2} + \frac{1}{(\delta y)^2} + \frac{1}{(\delta z)^2}\right)\right\}, && \text{Cartesian system} \\ \mathrm{SC} &= \Delta t \left\{\frac{|u_r|}{\Delta r} + \frac{|u_\theta|}{r\Delta\theta} + \frac{|u_z|}{\delta z} + 4\ \vartheta_t \left(\frac{1}{(\Delta r)^2} + \frac{1}{(r\Delta\theta)^2} + \frac{1}{(\delta z)^2}\right)\right\}, && \text{Cylindrical system} \end{aligned} \tag{4.24}$$

where δx, δy and δz are the cell sizes in the Cartesian system, while in the cylindrical system, the cell sizes are Δr, $r\Delta\theta$ and δz.

In order to solve the equation 4.22 together with the continuity equation, a four-step time advancement scheme was employed as follows:

$$u_i^* - \frac{\Delta t}{2}\mathrm{N}(u_i^*) = u_i^n + \Delta t\left[\frac{3}{2}\mathrm{M}(u_i^n) - \frac{1}{2}\mathrm{M}\left(u_i^{n-1}\right) + \frac{1}{2}\mathrm{N}(u_i^n) - \mathrm{P}_i(\phi^n)\right] \tag{4.25}$$

$$\frac{u_i^{**} - u_i^*}{\Delta t} = \mathrm{P}_i(\phi^n) \qquad \rightarrow\ u_i^{**} = u_i^* + \Delta t\ \mathrm{P}_i(\phi^n) \tag{4.26}$$

$$\nabla^2\phi^{n+1} = \frac{\rho}{\Delta t}\mathrm{div}(u_i^{**}) \tag{4.27}$$

$$\frac{u_i^{n+1} - u_i^{**}}{\Delta t} = -\mathrm{P}_i(\phi^{n+1}) \qquad \rightarrow\ u_i^{n+1} = u_i^{**} - \Delta t\ \mathrm{P}_i(\phi^{n+1}) \tag{4.28}$$

where u_i^* and u_i^{**} are the intermediate velocities. An advantage of the mentioned scheme is that the intermediate velocity boundary condition, required in equation 4.25, can be considered equal to u_i^{n+1} (Choi & Moin, 1994).

Finally, the quality of the LES calculations was evaluated by a method suggested by Pope (2004), which is expressed in terms of the turbulence resolution (TR) as follows:

$$\mathrm{TR} = \frac{\mathrm{K_{SGS}}}{\mathrm{K_{res}} + \mathrm{K_{SGS}}} \tag{4.29}$$

where $\mathrm{K_{SGS}}$ represents the sub-grid energy and $\mathrm{K_{res}}$ represents the resolved part of the energy. The resolved part of the energy is equal to the turbulent kinetic energy obtained from the simulation, since the large-scales or resolved scales are calculated through the filtered momentum equations.

$$\mathrm{K_{res}} = \mathrm{K} = 0.5\ \left(\overline{u'u'} + \overline{v'v'} + \overline{w'w'}\right) \tag{4.30}$$

The sub-grid energy ($\mathrm{K_{SGS}}$) corresponds to the small-scales that are modeled by the subgrid-scale model. Coussement et al. (2012) suggested the following equation to approximate $\mathrm{K_{SGS}}$:

$$\mathrm{K_{SGS}} = \frac{\overline{\vartheta_t^2}}{\left(C_m\overline{\Delta}\right)^2} \tag{4.31}$$

where C_m is an auto-similar function of the turbulence considered equal to 0.069 (Coussement et al., 2012).

According to Pope (2004), for a well-resolved LES, the TR value (Pope index) must be less than 0.2 that corresponds to a resolution of 80% of the turbulent kinetic energy by LES. The parts

of a domain in which this criterion was not met are interpreted as insufficiently resolved.

4.3 Results and discussion

As mentioned earlier in section 4.1, the goal of this chapter is to examine the effect of the Smagorinsky model parameters (Cs and Δ) on the flow prediction around two different flow obstacles (infinite square cylinder at Re_D = 20000 and infinite circular cylinder at Re_D = 3900). The corresponding tests are hereafter referenced as the main tests (in this chapter). In addition, a series of preliminary tests (sensitivity analysis) was required to be performed before the main numerical tests to find and confirm the proper grid resolution, vertical domain length and time-step size. Therefore, in the following, the outcomes of the sensitivity analysis are first summarized and then the main tests and the corresponding results are presented and discussed.

4.3.1 Sensitivity analysis

Details of the grid systems and preliminary numerical tests' characteristics used for the sensitivity analysis are presented in Table 4.1 together with the corresponding mean drag coefficient ($\overline{C}_D$), the root-mean-square value of the lift coefficient fluctuations (C_L r.m.s.) and the Strouhal number (St) which are the most important non-dimensional parameters of an unsteady flow around a cylinder.

Three sets of grids (namely a coarse one, a medium one and a fine one) were employed for the grid refinement study. The corresponding tests are referenced in accordance: *T_IS0*, *T_IS1* and *T_IS2*, for the square cylinder; and *T_IC0*, *T_IC1* and *T_IC2*, for the circular cylinder. In addition, an investigation regarding the effects of the cylinder length (L_z) on the accuracy of the results was also performed in the present study. For that, numerical tests *T_IS3* and *T_IC3* were done by considering a cylinder length larger than that in tests *T_IS2* and *T_IC2*. Moreover, the time-step size refinement study was carried out by performing numerical tests *T_IS4*, *T_IS5*, *T_IC4* and *T_IC5* and then by comparing the corresponding results with numerical results obtained from tests *T_IS2* and *T_IC2*. It is to be noted that all numerical simulations referred in Table 4.1 were performed by considering Cs = 0.1 and by computing Δ from equation 4.15.

Table 4.1: Infinite (square and circular) cylinder cases; sensitive analysis (Cs = 0.1 and $\Delta^3 = \delta_x\ \delta_y\ \delta_z$).

	Reference	a_1 or Δr_1	Total number of cells	L_z	Δt	SC_{max}	$\overline{C}_D$	C_L r.m.s.	St
Square cylinder	*T_IS0*	$0.025D$	$121\times114\times25$	πD	$0.0048\ \frac{D}{U_\infty}$	0.55	2.01	1.21	0.138
	T_IS1	$0.0225D$	$134\times126\times25$	πD	$0.0044\ \frac{D}{U_\infty}$	0.55	2.07	1.25	0.135
	T_IS2	$0.02D$	$153\times144\times25$	πD	$0.004\ \frac{D}{U_\infty}$	0.6	2.05	1.26	0.133
	T_IS3	$0.02D$	$153\times144\times50$	$2\pi D$	$0.004\ \frac{D}{U_\infty}$	0.6	2.07	1.16	0.134
	T_IS4	$0.02D$	$153\times144\times25$	πD	$0.003\ \frac{D}{U_\infty}$	0.45	2.05	1.2	0.133
	T_IS5	$0.02D$	$153\times144\times25$	πD	$0.0025\ \frac{D}{U_\infty}$	0.35	2.05	1.22	0.134
Circular cylinder	*T_IC0*	$0.025D$	$90\times124\times20$	πD	$0.0094\ \frac{D}{U_\infty}$	0.63	0.92	0.14	0.225
	T_IC1	$0.022D$	$100\times142\times25$	πD	$0.0078\ \frac{D}{U_\infty}$	0.6	0.97	0.1	0.211
	T_IC2	$0.02D$	$108\times162\times30$	πD	$0.0068\ \frac{D}{U_\infty}$	0.55	0.99	0.08	0.207
	T_IC3	$0.02D$	$108\times162\times60$	$2\pi D$	$0.0068\ \frac{D}{U_\infty}$	0.55	0.99	0.07	0.207
	T_IC4	$0.02D$	$108\times162\times30$	πD	$0.0058\ \frac{D}{U_\infty}$	0.45	1.01	0.1	0.205
	T_IC5	$0.02D$	$108\times162\times30$	πD	$0.0047\ \frac{D}{U_\infty}$	0.37	1.00	0.11	0.212

The main idea for the grid refinement was to increase the grid resolution in the xy or $r\theta$ plane (perpendicular to the cylinder axis) to find the adequate grid spacing for the main-tests study. Nevertheless, for the circular cylinder, the grid refinement was also performed in the vertical direction to examine also the effect of vertical grid spacing on the above-referred results. A comparison between those numerical results obtained using the medium and fine grids (see Table 4.1) indicates that, except for C_L r.m.s. (circular cylinder case), the differences between the corresponding results are less than 2%.

The requirements for further grid refinement were assessed by evaluating the dimensionless wall distance (wall units) of the first tangential velocity nodes to the cylinder surface. As an example, the dimensionless sizes of the first adjacent grid cells ($\delta x^+ = \rho u_* \delta x/\mu$, δy^+ and δz^+) over the square wall faces (*T_IS2*, fine grid) are shown in Figure 4.2. The values pictured are relatively large, as a wall model (boundary layer equations) was used near the wall. Furthermore, profiles of δx^+ and δy^+ are identical since the wall-adjacent grid cells in the horizontal planes are squares ($\delta x = \delta y$). Overall, Figure 4.2 shows that, at front face of the square, the dimensionless size of the first grid cell (for the three-axis) increases from a minimum value at the stagnation point (O_1) to a maximum at the upstream corner edge B. Over the square face B-C, the referred

dimensionless sizes are oscillated (decreased and increased significantly), similar to the numerical predictions of Trias et al. (2015). Finally, at the square rear face, the corresponding sizes decrease toward the wake centerline (point O_2). It should be noted that the first tangential-velocity nodes near the square wall surfaces are situated at $\delta x^+/2$ or $\delta y^+/2$, where the LES model and the wall model are matched. Using the fine grid (*T_IS2*), those tangential-velocity nodes are between 0 and about 40 wall units. Therefore, no further refinement was performed in this study since $\delta x^+/2$ (or $\delta y^+/2$) is considered to be sufficiently large to allow the use of a wall model (Schindfessel et al., 2015). Concerning the circular cylinder (*T_IC2*, fine grid), values of Δr^+ (r is the normal direction to the circular cylinder face) are less than 15 as the corresponding Reynolds number is relatively low.

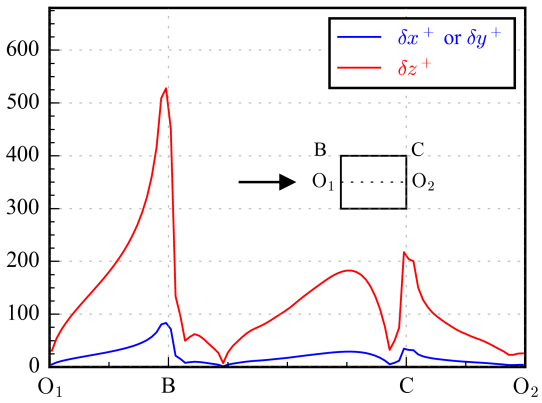

Figure 4.2: Dimensionless sizes (δx^+, δy^+ and δz^+) of the first adjacent cells over the half contour line of the infinite square cylinder geometry (*T_IS2*, fine grid).

The grids' quality was also assessed by considering the Pope index. For that, the turbulence resolution (TR) was estimated at each grid cell. The corresponding TR values for all preliminary simulations indicate that the most of grid cells are in the zone where TR ≤ 0.2, which according to Pope (2004) means that most part of domain was sufficiently resolved. As examples, the results obtained from test *T_IS2* (fine grid, square cylinder) and test *T_IC0* (coarse grid, circular cylinder) are presented in Figure 4.3. The value of TR is between 0 and 1. According to Pope, TR = 0 corresponds to DNS and TR = 1 to RANS modeling. It is to be noted that the grid cells lying inside the square cross-section geometry were excluded from the TR evaluation.

Concerning the vertical domain length (L_z), numerical tests *T_IS3* and *T_IC3* were conducted

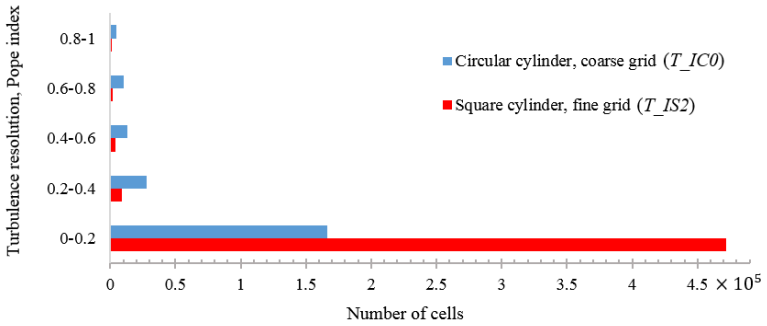

Figure 4.3: Turbulence resolution (TR), infinite cylinder cases.

by considering $L_z = 2\pi D$, larger than that (πD) in the reference tests *T_IS2* and *T_IC2* but the cells size in the vertical direction was considered the same as in the referenced tests (see Table 4.1). The corresponding numerical results, except for C_L r.m.s., were observed to be almost similar. Overall, it was found that doubling the cylinder length (from πD to $2\pi D$) and keeping the same resolution in the vertical direction did not change noticeably the values of the non-dimensional parameters, in accordance to that reported by Lysenko et al. (2012).

Finally, the effect of the time-step size was evaluated by performing tests *T_IS4*, *T_IS5*, *T_IC4* and *T_IC5* and comparing the corresponding results with those obtained in tests *T_IS2* and *T_IC2* as presented in Table 4.1. The time-step sizes were selected regarding a nominal stability limit of AB-CN ($SC_{max} = 0.5$) introduced by Le & Moin (1991). Again, the most noticeable effect was observed only on the values of C_L r.m.s.. It is noteworthy to mention that the number of inner iterations to solve the Poisson equation 4.27 slightly increased with the time-step size, leading to increase in the CPU time.

Considering the above-described, the grid cells, vertical domain length and time-step sizes employed in tests *T_IS2* and *T_IC2* were selected for the main-tests study (for evaluation of the Smagorinsky model parameters).

4.3.2 Main numerical test results

It is noteworthy to recall that the goal, in this chapter, is to evaluate the performance of the LES Smagorinsky model (together with a simple wall model) by using different values for the Smagorinsky coefficient and different definitions for computing the spatial filter width. To achieve

the goal and by considering the preliminary tests, the turbulent flow around the cylinders was predicted by using a different value for the Smagorinsky coefficient (Cs = 0.13, the corresponding test hereafter referred to as *T_IC6*) and a different definition for computing the spatial filter width (Δ was computed from equation 4.16, the corresponding test hereafter referred to as *T_IS6*). The numerical results were then compared with the results obtained from test *T_IC2* (Cs = 0.1) and test *T_IS2* (Δ from equation 4.15).

In order to clarify the difference between the two equations 4.15 and 4.16, the distribution of the ratio $\Delta_{4.16}/\Delta_{4.15}$ around the square cylinder is presented in Figure 4.4. The mentioned ratio is not uniform in the computational domain. In the zone adjacent to the square cylinder, the ratio is greater than in the outer zone. Overall, equation 4.16 presented higher Δ values than equation 4.15. Since the value of Δ plays a control role in the modeling of the small-scale components in the LES solution, using higher values of Δ may yield inaccurate prediction of the flow variables due to unresolved small eddies' effects. Hence, only in test *T_IS6* (when using equation 4.16), the smaller value of k y_c and Cs Δ was used for estimating the mixing length as $L_s = \min(\mathrm{k}\, y_c, \mathrm{Cs}\, \Delta)\mathrm{D_f}$.

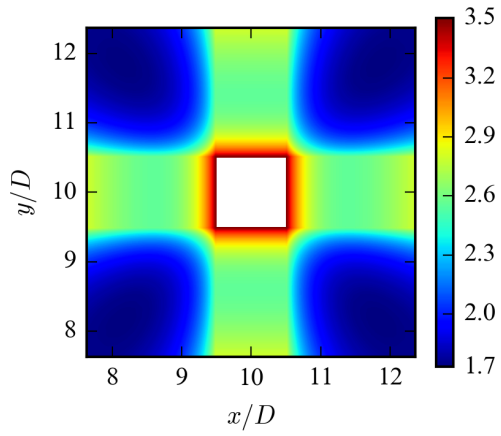

Figure 4.4: Ratio of the spatial filter width scales obtained by means of the two definitions $\left(\frac{\sqrt{\delta x^2+\delta y^2+\delta z^2}}{\sqrt[3]{\delta x\ \delta y\ \delta z}}\right)$, infinite square cylinder case.

The flow variables (velocity components and pressure) were averaged both in the vertical direction and over time during about 50 vortex shedding periods after removing the initial uniform condition effects from the calculations. The transient time (normalized by multiplying it by (U_∞/D) was about 200 and 175 for the square and circular cylinder cases, respectively, to achieve

a fully developed state. The CPU time for one time-step was around 1.5 seconds on average and the total CPU time spent on the transient time and the time-averaging period was about 35 hours for the square cylinder case and about 20 hours for the circular cylinder case by employing 16 processors in parallel. Overall, the computational cost of the present numerical simulations was much lower than the simulations performed by Lysenko et al. (2012) and Kim et al. (2015), as explained earlier in section 4.1, by the application of the wall model.

4.3.2.1 Mean integral quantities

Table 4.2 summarizes the numerical simulation characteristics of tests *T_IS2*, *T_IS6*, *T_IC2* and *T_IC6* together with the ones of some comparative reference tests. In addition, the corresponding experimental and numerical results for the non-dimensional parameters are also presented in Table 4.2.

Table 4.2: Infinite cylinder cases: present study numerical tests (shaded) and numerical and experimental tests of reference - characteristics and results obtained.

Reference		Re_D	Disc. [a]	Wall model	Δ	Cs	$\overline{C}_D$	St
Present study	*T_IS2*	20000	CD+QUICK	BLE [b]	(4.15) [c]	0.1	2.05	0.133
(Square cylinder)	*T_IS6*				(4.16) [c]		2.15	0.128
Sohankar et al. (2000)		22000	CD	No		0.1	2.22	0.127
						Dyn. [d]	2.03	0.126
Trias et al. (2015)		22000	Direct Numerical Simulation				2.18	0.132
Roosenboom (2005)		20000	Experiment				2.18	0.129
Lyn et al. (1995)		21400	Experiment				2.1	0.132
Present study	*T_IC2*	3900	QUICK	BLE	(4.15)	0.1	0.99	0.207
(Circular cylinder)	*T_IC6*					0.13	1.01	0.209
Lysenko et al. (2012)		3900	CD	No		Dyn.	0.97	0.209
Beaudan & Moin (1994)		3900	Up-Biased [e]	No		Dyn.	1.00	0.203
Breuer (1998)		3900	QUICK	No		0.1	0.97	
			CD			Dyn.	1.02	
Parnaudeau et al. (2008)		3900	Experiment					0.208

[a] Disc.: Discretization scheme for convection terms. [b] BLE: Boundary Layer Equations. [c] (4.15): equation (4.15); (4.16): equation (4.16). [d] Dyn.: Dynamically computed. [e] Up-Biased: Upwind-Biased scheme.

The time-averaged or mean drag coefficients were computed by considering the viscous (friction) and the pressure forces acting on the cylinders. The obtained numerical results for the square cylinder (*T_IS2* and *T_IS6*) indicate that $\overline{C}_D$ increases with increasing the spatial filter width. It is noteworthy to recall that equation 4.16 led to higher Δ values than equation 4.15. Overall, the predicted $\overline{C}_D$ values are fairly in good agreement with the reference data presented in Table 4.2. For a more in-depth evaluation, the time-dependent drag and lift coefficients (C_D and C_L) acting on the square cylinder are presented in Figure 4.5 for about 25 vortex shedding periods. The C_L value, by using equation 4.15, oscillates nearly periodically over time compared to that with equation 4.16. For further comparison, the r.m.s. values of the drag and lift coefficients fluctuations (C_D r.m.s. and C_L r.m.s.) were computed for both time history profiles. The corresponding values are, respectively, 0.1 and 1.26, when using equation 4.15 and 0.18 and 1.13, when using equation 4.16. Overall, those are fairly in good agreement with the experimental results reported by Sohankar et al. (2000) (C_D r.m.s. = 0.17-0.22 and C_L r.m.s. = 1.19-1.3).

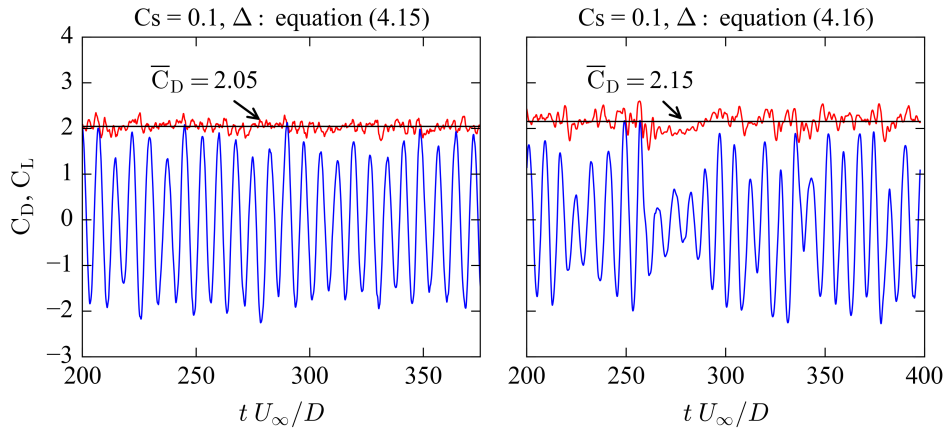

Figure 4.5: Time variation of the drag (C_D, red line) and lift (C_L, blue line) coefficients for the infinite square cylinder simulations (*T_IS2*: left and *T_IS6*: right), Re_D=20000.

In the circular cylinder case, $\overline{C}_D$ increased slightly with increasing Cs from 0.1 (*T_IC2*) to 0.13 (*T_IC6*). Overall, $\overline{C}_D$ was well predicted in agreement with the results obtained by means of the reference studies as presented in Table 4.2.

The pressure distribution along the cylinder surface was also evaluated for both cases, taking into account that the pressure force is known to have the main contribution to the drag on the turbulent flow regime (Trias et al., 2015). The distribution of the time-averaged pressure coefficient

($\overline{C}_P = (\bar{p} - p_\infty)/(0.5\rho U_\infty^2)$, in which p_∞ is the free stream pressure) on the infinite square and circular cylinders' surface is presented in Figure 4.6 a) and Figure 4.6 b), respectively. For the circular case, only *T_IC2* results are shown as *T_IC6* results are most similar to those. The pressure measurements of Bearman & Obasaju (1982), Norberg (1987), Hasan (1989) and numerical results of Trias et al. (2015) are also plotted to validate the present numerical results.

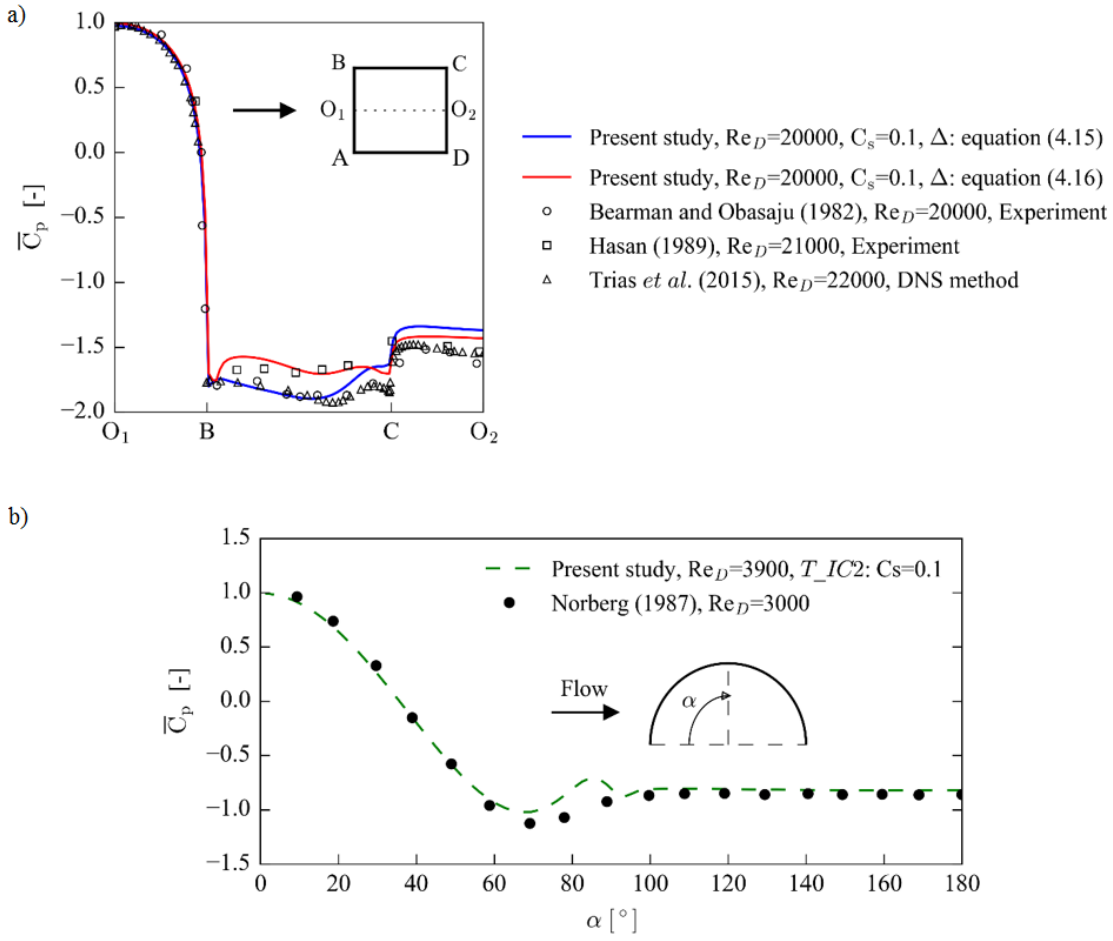

Figure 4.6: Time- and vertically- averaged pressure coefficients on the cylinders' surface: a) infinite square cylinder, b) infinite circular cylinder.

In the square cylinder case, Figure 4.6 a), the main difference between the two profiles obtained by the present study is observed at face B-C. Nevertheless, equation 4.15 results are fairly in agreement with the experimental and numerical results presented by Bearman & Obasaju (1982) and Trias et al. (2015), while equation 4.15 results are similar to the physical observations of Hasan (1989). Moreover, using equation 4.16 (higher Δ values) led to slightly decrease the pressure

values at face C-D, while no change was observed at face A-B. Therefore, the pressure difference between the two mentioned faces increased from test *T_IS2* to *T_IS6* and consequently, the drag component became greater by using equation 4.16.

Concerning the circular cylinder, Figure 4.6 b), the $\overline{C}_P$ profile is in good agreement with the measurements performed by Norberg (1987) for a nearly similar flow condition. As pictured, $\overline{C}_P$ decreased from a positive maximum value at the stagnation point ($\alpha = 0$) until a negative minimum value and then increased slightly until it reached a constant value in the wake region. A small over-estimation of $\overline{C}_P$ is observed at the $70^o < \alpha < 90^o$ zone but the agreement in the wake region is excellent. Moreover, a small bump at about $\alpha = 85^o$ is detected when compared to the experimental results. Nevertheless, the overall drag coefficient could be well estimated.

The Strouhal number (St) is another relevant non-dimensional parameter and, in this study, it was determined from the power spectrum of the C_L time history. The corresponding results are all within the range of the reference data as reported in Table 4.2.

In order to study the flow structures around the cylinders, the corresponding time- and vertically-averaged streamlines are presented in Figure 4.7. In the square cylinder case, Figure 4.7 a), the flow separates from the two corner edges at the upstream side of the cylinder and creates four regions with recirculation. Two recirculation regions are located at the lateral sides and the two others are developed behind the square cylinder. The normalized focal points coordinates of the mentioned recirculation regions with respect to the center of the square geometry are (0.14, $\pm$0.65) and (0.74, $\pm$0.37) by using equation 4.15 and are (0.12, $\pm$0.66) and (0.82, $\pm$0.42) by using equation 4.16. The corresponding focal points coordinates obtained experimentally by Hinsberg (2004) are (0.2, 0.65) and (0.15, -0.62) for the lateral recirculation regions and are (0.71, 0.43) and (0.75, -0.32) for the ones behind the square cylinder. Concerning the wake region, the use of equation 4.16 led to a longer recirculation length (L_r) than that with equation 4.15. However, equation 4.16 resulted in $L_r = 0.82D$ that is in good agreement with the experimental results presented by Lyn et al. (1995) ($L_r = 0.9D$ at $Re_D = 21400$) and Durão et al. (1988) ($L_r = 0.83D$ at $Re_D = 14000$), while equation 4.15 yielded $L_r = 0.63D$ that is quite in agreement with physical measurements of Roosenboom (2005) ($L_r = 0.64D$ at $Re_D = 20000$).

For a circular cylinder, the separation points' positions are not fixed and in accordance to

the different bibliography (Breuer, 1998; Kravchenko & Moin, 2000; Lysenko et al., 2012), the separation shall occur at α_{sep} = 85°-89° (Re_D = 3900), where α is measured from the stagnation point. The separation points' positions obtained in this study were not included in Table 4.2, as the values obtained for *T_IC2* and *T_IC6* are identical: about 88° from the stagnation point (see Figure 4.7 b)). Concerning the wake recirculation length, the use of Cs = 0.1 resulted in a longer recirculation length than that obtained by using Cs = 0.13 (respectively, L_r = 1.75D and 1.6D), both over-predicted compared to the experimental results reported by Breuer (1998). Nevertheless, Breuer (1998) also numerically obtained L_r = 1.7D by using the Smagorinsky subgrid-scale model (Cs = 0.1) and the QUICK scheme for the approximation of the convection terms as used in this study what verifies the present numerical calculations. Moreover, it is noteworthy to mention that Beaudan & Moin (1994) numerically obtained L_r as equal to 1.74D by using the Smagorinsky model with a fixed coefficient and applying a fifth-order accurate upwind-biased scheme on the convection terms.

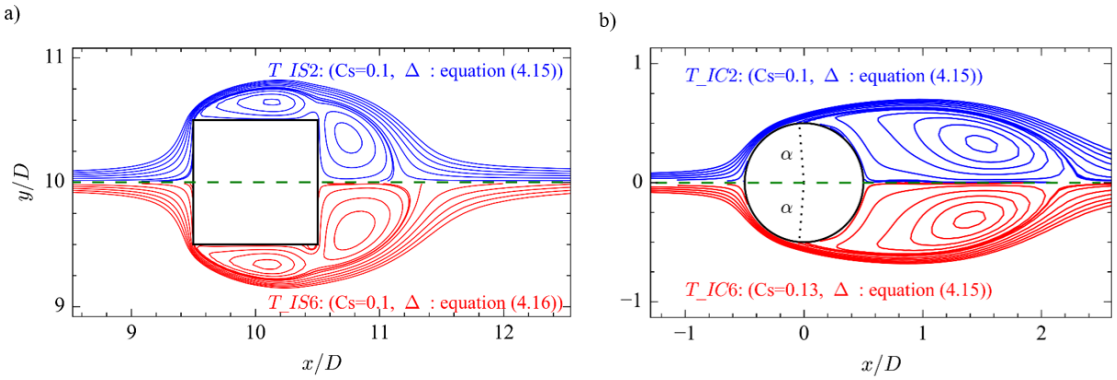

Figure 4.7: Time- and vertically- averaged streamlines around the: a) infinite square cylinder and b) infinite circular cylinder.

4.3.2.2 First-order and second-order statistics

The time- and vertically- averaged u-velocity ($<\bar{u}>$) values along the wake centerline of the square and circular cylinders are presented in Figure 4.8 and Figure 4.9, respectively. The value of $<\bar{u}>$ at the cylinder surface (rear face) is zero; it reaches a negative minimum value in the recirculation zone and then increases progressively until a maximum value.

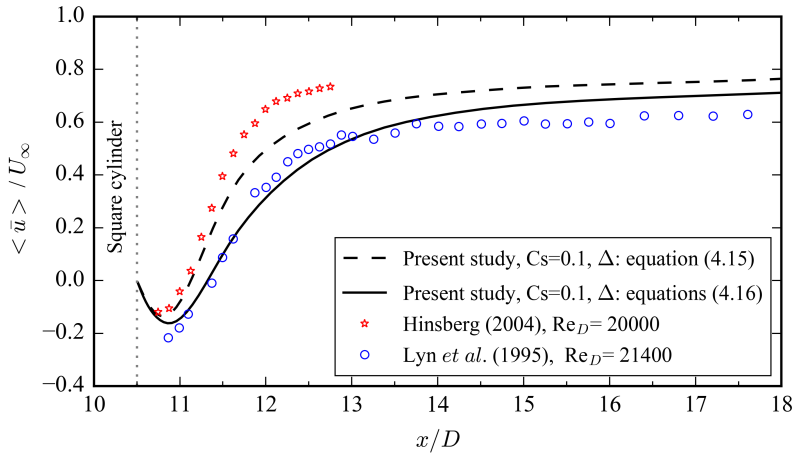

Figure 4.8: Time- and vertically- averaged u-velocity at the wake centerline of the infinite square cylinder, Re_D=20000.

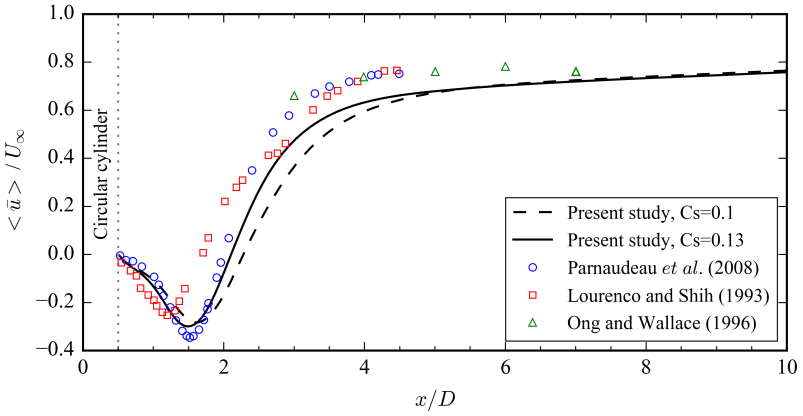

Figure 4.9: Time- and vertically- averaged u-velocity at the wake centerline of the infinite circular cylinder, Re_D=3900.

Although Lyn et al. (1995) and Hinsberg (2004) presented comparative different results at the wake centerline downstream of the square cylinder for Re_D about 20000, both were used as reference data in this study (see Figure 4.8). In fact, the present numerical results obtained by using equation 4.16 are in agreement with the experimental measurements of Lyn et al. (1995) and those calculated by using equation 4.15 are similar to the physical observations of Hinsberg (2004).

In the circular cylinder case (Figure 4.9), also Lourenco & Shih (1993) and Parnaudeau et al. (2008) presented different $<\bar{u}>$ profiles at the wake centerline downstream of the cylinder for Re_D = 3900. The present numerical results (for Cs = 0.1 and Cs = 0.13) are both more similar to the

experimental results reported by Parnaudeau et al. (2008). The experimental measurements of Ong & Wallace (1996), which were also plotted in Figure 4.9, enabled to control and validate the upper limit of the predicted $<\bar{u}>$ values at the symmetry line outside of the recirculation zone.

The time- and vertically- averaged velocity magnitude ($<\left|\overline{U}\right|>$) and vertically-averaged turbulence intensities ($<\sqrt{\overline{u'u'}}>$ and $<\sqrt{\overline{v'v'}}>$) around the square cylinder are presented in Figure 4.10. The approach flow is deflected by the square cylinder and accelerated close to its upstream side edges. The use of equation 4.15 resulted in a higher $\left|\overline{U}\right|_{\max}$, fairly close to the corresponding value presented by Minguez et al. (2011) ($\left\{\left|\overline{U}\right|/U_\infty\right\}_{\max}$ = 1.65 for Re_D = 21400), while equation 4.16 yielded a lower value for $\left|\overline{U}\right|_{\max}$, in agreement with the ones experimentally obtained by Hinsberg (2004) ($\left\{\left|\overline{U}\right|/U_\infty\right\}_{\max}$ = 1.5 for Re_D = 20000) and Roosenboom (2005) ($\left\{\left|\overline{U}\right|/U_\infty\right\}_{\max}$ = 1.425 for Re_D = 20000).

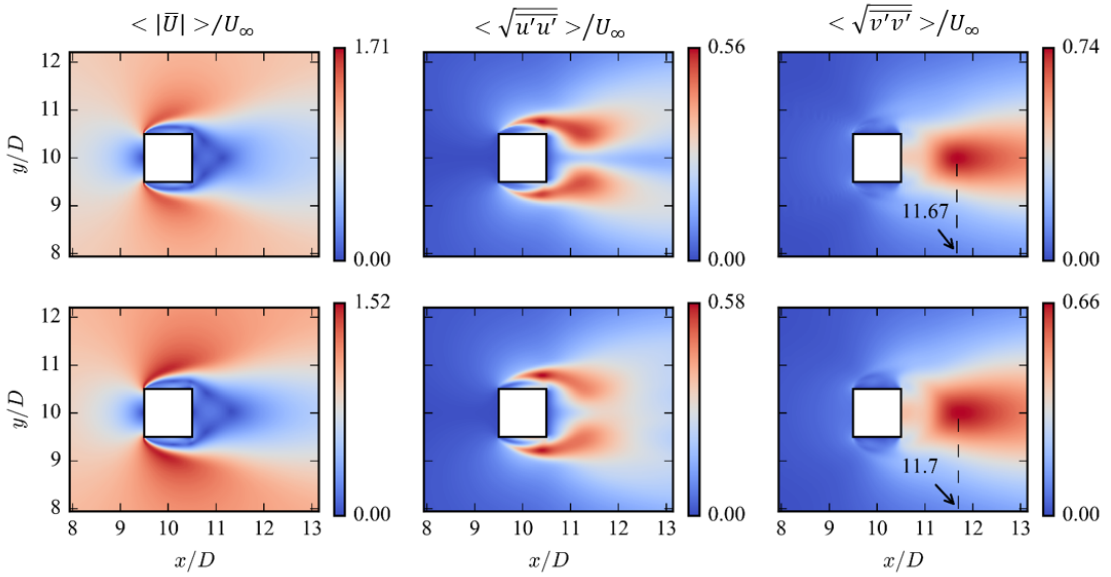

Figure 4.10: Time- and vertically- averaged velocity magnitude (left) and root-mean-square u- (center), v- (right) fluctuations around the infinite square cylinder at Re_D=20000 (top: Δ computed from equation 4.15; and bottom: Δ computed from equation 4.16).

The plots of root-mean-square u-fluctuations' maps ($<\sqrt{\overline{u'u'}}>$: turbulence intensity in the longitudinal direction) in Figure 4.10 (center) show a maximum value at each side of the centerline close to the rear corner points of the square geometry. The corresponding maximum value of $<\sqrt{\overline{u'u'}}>/U_\infty$ was obtained as equal to 0.56 by using equation 4.15 and 0.58 by using equation

4.16. It is noteworthy to mention that Roosenboom (2005) reported a maximum value of about 0.61 with a location similar to the present study.

The root-mean-square v-fluctuations' maps ($<\sqrt{\overline{v'v'}}>$: turbulence intensity in the transverse direction) in Figure 4.10 (right) show a sole maximum at the centerline behind the square cylinder. The use of equation 4.15 led to a maximum value higher than that with equation 4.16. Nevertheless, both maximum values are lower than the maximum one reported by Roosenboom (2005) ($<\sqrt{\overline{v'v'}}>/U_\infty = 0.9$ for $\mathrm{Re}_D = 20000$). However, the position of the maximum values at the centerline, x/D =11.67 for equation 4.15 and x/D =11.7 for equation 4.16, is similar to the position experimentally observed by Roosenboom (2005).

Concerning the circular cylinder case, the time- and vertically- averaged velocity components in the longitudinal and transverse directions and the corresponding turbulence intensities around the cylinder are presented in Figure 4.11 (*T_IC6*: Cs = 0.13). The numerical results obtained for *T_IC2* (Cs = 0.1) are nearly similar to those presented in Figure 4.11. The numerical predictions indicate that $\bar{u}$-velocity component's map is symmetric, while $\bar{v}$-velocity component's map is anti-symmetric. Moreover, $\sqrt{\overline{u'u'}}$ and $\sqrt{\overline{v'v'}}$ maps are both symmetric. The maximum value of $\sqrt{\overline{v'v'}}$ is located on the wake centerline, while the maximum values of $\sqrt{\overline{u'u'}}$ are observed on both sides of the wake centerline. The mentioned observations are in agreement and similar to those reported by Beaudan & Moin (1994), Parnaudeau et al. (2008) and Meyer et al. (2010) for the same cylinder geometry and flow conditions.

4.4 Conclusions

The space-filtered Navier-Stokes and continuity equations (LES model) were solved in the framework of a fractional time-step method by using the semi-implicit Adams-Bashforth and Crank-Nicolson scheme. The Smagorinsky model was selected as the subgrid-scale model and the approximate values of the wall shear stress components were imposed at the wall boundaries by employing a simple form of the boundary layer equations. Analysis of the results obtained by the numerical simulations of the 3-D turbulent flow around infinite-length cylinders with different cross-sections (square and circle) yielded:

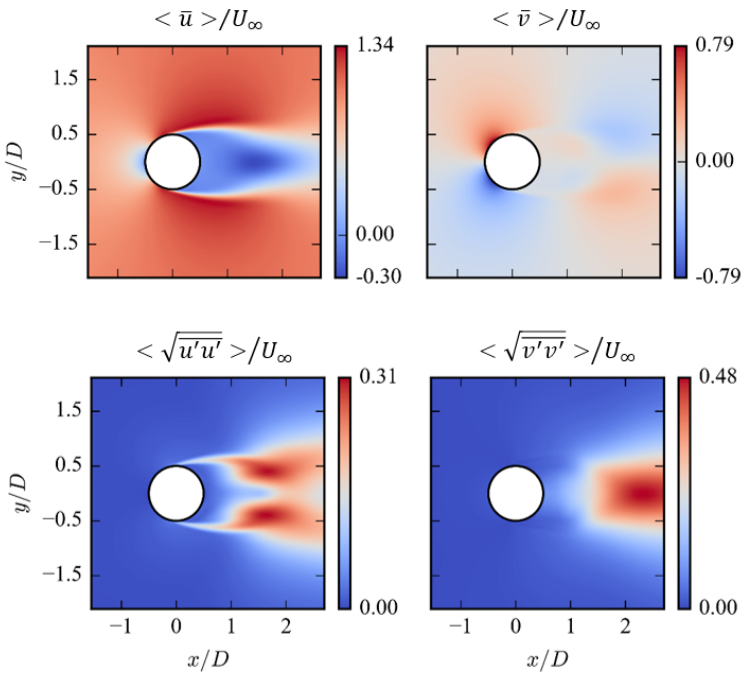

Figure 4.11: Time- and vertically- averaged velocity components (top) and root-mean-square *u*-, *v*- fluctuations (bottom) around the infinite circular cylinder (*T_IC6*: Re_D=3900, Cs = 0.13).

- Overall, using wall modeling, the flow characteristics around the selected cylinders were predicted in good agreement with the experimental and numerical reference data. The solution procedure, developed in this study, was shown to have low computational cost as all calculations were performed in a short period of time (longest elapsed time, CPU time, for a simulation case was about 35 hours) without employing a large number of processors.

- For the square cylinder, the joint use of the CD and QUICK schemes could represent results in agreement with available experimental data. Nevertheless, it requires predefining the subdomains in which each scheme is used. In the complex pier studies, the definition of the subdomains may alter for one case to another and hence the hybrid CD-QUICK scheme (as explained in this chapter) was considered not interesting for the following studies. Concerning the circular cylinder, although the corresponding wake recirculation lengths were over-predicted compared to the available experimental data, those are in good agreement with the referenced numerical studies in which the LES Smagorinsky model and a high-order upwind scheme (e.g., QUICK scheme) for the approximation of the convection terms

(as the same in this study) were used. Considering the above-described, the sole use of the QUICK or CD scheme will be further evaluated in the next chapter.

- A sensitivity analysis of the Smagorinsky coefficient value resulted in that changing the coefficient from 0.1 to 0.13 did not noticeably change the corresponding results. Yet, the numerical results were found to largely depend on how the spatial filter width is estimated for the solution. In this study, the spatial filter width Δ was calculated at each grid cell through two different equations: (*i*) cubic root of the computational cell volume (equation 4.15), and (*ii*) root-sum-squared of the grid cell size along each direction (equation 4.16). Both equations 4.15 and 4.16 could represent numerical results in agreement with the ones obtained from different numerical and experimental reference studies. Nevertheless, in overall, equation 4.16 presented higher Δ values than those with equation 4.15, which can be interpreted to not be appropriate because using higher Δ values may affect modeling of the small-scale components. Hence, for the further simulations (next chapters), the spatial filter width Δ was set as equal to the cubic root of the computational cell volume (equation 4.15).

CHAPTER 5

Modeling Complex Geometries

5.1 Introduction

To predict the flow past a bridge pier on a scoured bed, the numerical approach should be able to model the turbulent flow features and the complex geometries properly. In the previous chapter, the applicability of the LES Smagorinsky model as a turbulent flow solver was investigated and in this chapter, a methodology for performing the LES near the complex geometries is presented.

The final goal is to model the pier and bed geometries in a simple and accurate way. In the last years, the so-called immersed-boundary method has been widely used to study the flow around bluff bodies with complex geometries (e.g., Balaras (2004)). In this method, the bluff body is immersed in a structured grid system with orthogonal grid lines and its effect on the flow field is usually accounted for by estimation of a body-force term around the immersed body. The near-wall model explained in the previous chapter, namely the boundary layer equations, can also be incorporated in the solution together with the immersed-boundary method. In general, the

boundary layer equations are solved on an embedded near-wall mesh (inner-layer) such that the equations are forced at the outer boundary of the inner-layer by the first instantaneous tangential velocities to the wall surface, obtained from the LES calculations, while the no-slip condition is applied at the stationary wall boundary (see Figure 5.1 a)). In a case when the wall normal plane does not cross any velocity point (e.g., Figure 5.1 b)), the boundary condition at the outer edge of the inner-layer is obtained using the surrounding LES velocities.

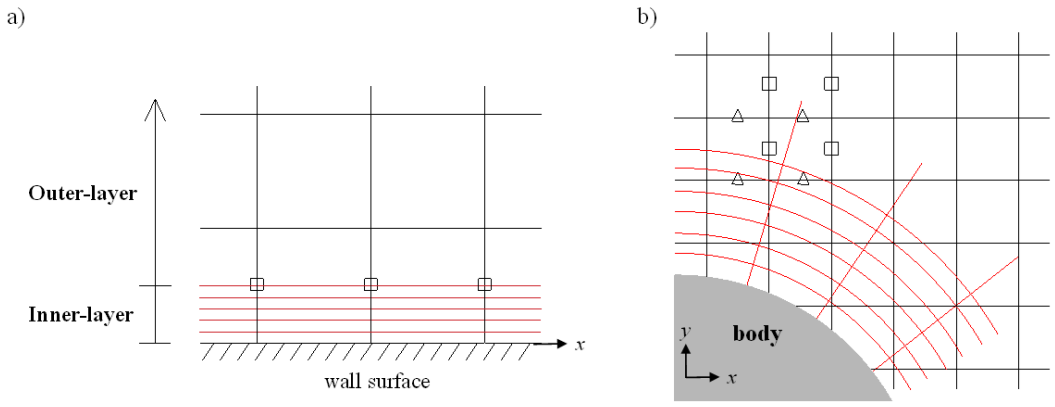

Figure 5.1: Representation of the Two-Layer approach for a) a flat wall surface and b) a curved wall surface: (square: u-velocity points; triangle: v-velocity points), immersed-boundary method.

In this study, the LES Smagorinsky model was first upgraded by using the immersed-boundary method and then the model was evaluated by considering the turbulent flow around an infinite-length circular cylinder at $\mathrm{Re}_D = 4 \times 10^4$. For this circular cylinder case, the velocity values at the outer boundary points of the inner-layer were interpolated from the surrounding points and importantly, the inner-layer thickness was determined in such a way that the first velocity points from the wall surface were not involved in the interpolation procedure. Then, values of the velocity at the first velocity points, outside the body, were estimated through solving the simplified boundary layer equations and rest of the velocity values through the LES calculations. The corresponding numerical results together with available reference data are summarized in Appendix A (Figure A.1 and Table A.1). Overall, the present numerical results are in good agreement with the ones obtained from the referenced bibliography. Nevertheless, employing the above-referred methodology for modeling cases with irregular boundary shapes, such as an eroded bed, was found complicated.

An alternative approach to the immersed-boundary method is to use the FAVOR (stands for

Fractional Area/Volume Obstacle Representation) method as explained by Hirt & Sicilian (1985). In this method, prior to solving the governing equations, the position of the grid cell vertices with respect to the flow obstacle is determined and subsequently, the fractional portions of the grid cell faces open to the flow and the cell volume fraction occupied by the fluid (hereafter referred to as FAVOR variables) are computed. In fact, in this method, the geometry in every grid cell is converted into fractional volume and areas. For example, Figure 5.2 shows the fractional areas for flow in a 3-D Cartesian grid cell that contains a wall surface. The FAVOR method's simplicity for modeling complex geometries was found attractive and thus its accuracy for the study of bridge pier problems was evaluated in this research, which is presented in this chapter.

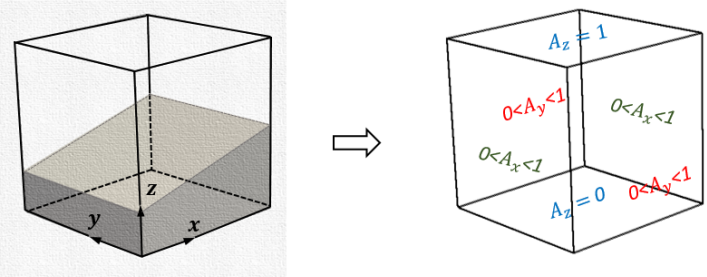

Figure 5.2: FAVOR method to describe the geometry in a Cartesian cell (definition of the open areas fractions).

In the following sections, details of the numerical model (including the governing equations, assumptions and solution procedure) are first summarized in section 5.2 and then the numerical model validation is presented in section 5.3.

5.2 Numerical model details

The space-filtered Navier-Stokes and continuity equations for a 3-D incompressible flow, including the FAVOR variables, are written as:

$$\frac{\partial u_i}{\partial t} = -\frac{1}{V_F}\left(u_j A_j \frac{\partial u_i}{\partial x_j}\right) - \frac{1}{\rho}\frac{\partial \phi}{\partial x_i} + \frac{W S_i}{\rho\, V_F} + \frac{1}{V_F}\frac{\partial\left(\left(\vartheta + \vartheta_t\right) A_j S_{ij}\right)}{\partial x_j} \tag{5.1}$$

$$\frac{\partial}{\partial x_i}\left(A_i u_i\right) = 0 \tag{5.2}$$

The terms on the right-hand side of equation 5.1 are called the convection, pressure, wall shear

stress and viscous terms, respectively. The variable V_F represents the volume fraction of the fluid, which is estimated for each grid cell. A_i and A_j, i and j = 1, 2 and 3, denote the fractional areas open to the flow such that A_1 (or A_x) is estimated at the cell-faces normal to the x-direction, A_2 (or A_y) at the cell-faces normal to the y-direction and A_3 (or A_z) at the cell-faces normal to the z-direction. Furthermore, ϕ is the pseudo-pressure (equation 4.5) and ϑ_t denotes the eddy viscosity (equation 4.13). It should be noted that the wall damping function D_f, in equation 4.14, was neglected in computing the mixing length and consequently in estimating ϑ_t. In fact, according to equation 4.17, D_f tends to unity for y^+>30 (i.e., when the near-wall region is not fully resolved). Nevertheless, for confidence, in a grid cell containing the wall surface, the mixing length was considered as the smaller value of k y_c and Cs Δ as used by Werner & Wengle (1991) for the LES calculations with wall modeling. The Smagorinsky coefficient Cs was set equal to 0.1 and the spatial filter width Δ was set as equal to the cubic root of the computational cell volume (equation 4.15). Finally, the terms WS_i represent the wall shear stresses. According to the FAVOR method, if the fractional area open to flow (A) at a cell face is less than unity, the remaining area (1-A) is considered to be a wall on which a wall shear stress is generated. For instance, on a face y parallel to the longitudinal velocity u, the shear stress term can be estimated as $\rho(1-A_y)u_*^2/\delta y$, in which δy is the cell size in the y-direction. Here, the friction velocity u_* was obtained by using the wall tangential velocity (u_t) through equation 5.3 that incorporates the bed roughness effect in the solution. Moreover, according to Roulund et al. (2005), this equation allows using a coarse mesh resolution close to the wall boundaries.

$$\frac{u_t}{u_*} = 2\int_0^{x_{2C}{}^+} \frac{\mathrm{d}x_2{}^+}{1+\sqrt{1+4\mathrm{k}^2(x_2{}^+ + \Delta x_2{}^+)^2\left[1-\exp\left(-\frac{x_2{}^+ + \Delta x_2{}^+}{25}\right)\right]^2}} \tag{5.3}$$

where

$$\Delta x_2{}^+ = 0 \quad \text{for } k_s{}^+ \le 5\,; \qquad \Delta x_2{}^+ = 0.9\left[\sqrt{k_s{}^+} - k_s{}^+ \exp\left(-\frac{k_s{}^+}{6}\right)\right] \quad \text{for } k_s{}^+ > 5 \tag{5.4}$$

with $k_s{}^+$ being the normalized equivalent sand roughness ($k_s u_*/\vartheta$), $x_2{}^+$ the dimensionless distance in the direction normal to the wall and $x_{2C}{}^+$ dimensionless wall normal distance of a point where the tangential velocity is available.

Although several researchers have employed equation 5.3 in the local pier scour predictions (e.g., Roulund et al., 2005; Stahlmann, 2013; Baykal et al., 2015), it uses an assumed velocity profile (the van Driest velocity profile as reported by Baykal et al. (2015) and Stahlmann (2013)) and that justifies evaluating its accuracy for separated flows, performed in this study. For that, equation 5.3 was iteratively solved, in which the trapezoidal rule was applied to estimate the integral term.

Approximation of the convection terms, in equation 5.1, was performed using either the CD scheme or the QUICK scheme, while only the CD scheme was applied on the other spatial derivative terms. In fact, following an investigation of Tafti (1996) on turbulent channel flow predictions, applying the CD scheme on the convection terms was reported to resolve the turbulent spectrum better than the higher order upwind schemes. Nevertheless, for a more complex case such as flow around a circular cylinder, applying the CD scheme on the convection terms resulted in instabilities at the upstream side of the cylinder (an example is shown in Figure B.1 of Appendix B), while the QUICK scheme could remove those instabilities. In summary, concerning the convection terms, the CD scheme was adopted to predict the turbulent flat-channel flow and the QUICK scheme was selected for cases with a complex flow compared to the flat-channel case.

For the temporal discretization, the fully explicit second-order Adams-Bashforth scheme was employed in the solution. Although the implicit treatment of the diffusion terms generally allows using a larger time-step size than the explicit treatment, it might not result in significant gains in this study because of using a relatively coarse mesh near the wall boundaries. In addition, using a fully explicit scheme avoids the requirement of the intermediate velocity boundary condition and that simplifies the solution procedure.

Finally, in the framework of the fractional-step method, a four-step time advancement scheme was employed to solve equations 5.1 and 5.2 as follows:

- Computing the intermediate velocity u_i^*:

$$\frac{{u_i}^* - {u_i}^n}{\Delta t} = \frac{3}{2}\,\mathrm{M}\left({u_i}^n\right) - \frac{1}{2}\mathrm{M}\left({u_i}^{n-1}\right) - \mathrm{P}_i(\phi^n) \tag{5.5}$$

  The M operator includes the convection, wall shear stress and viscous terms of equation 5.1. The pressure term was denoted by the P operator and estimated using the previous time-step

data.

- Calculating a new intermediate velocity u_i^{**} by adding the pressure term:

$$\frac{{u_i}^{**} - {u_i}^{*}}{\Delta t} = \mathrm{P}_i(\phi^n) \tag{5.6}$$

- Solving an implicit equation to obtain the new pressure values:

$$\frac{\partial}{\partial x_i}\left(A_i \frac{\partial \phi^{n+1}}{\partial x_i}\right) = \frac{\rho}{\Delta t}\frac{\partial (A_i {u_i}^{**})}{\partial x_i} \tag{5.7}$$

- Updating the velocity field through the latest pressure values:

$$\frac{{u_i}^{n+1} - {u_i}^{**}}{\Delta t} = -\mathrm{P}_i(\phi^{n+1}) \tag{5.8}$$

When periodic boundary conditions are required in the x-direction, namely to facilitate simulation of an endless channel, a mean pressure gradient that drives the flow in the x-direction is used in the momentum equation in terms of a source term:

$$\mathrm{S}_1^{n+1} = \mathrm{S}_1^n + \frac{\alpha}{\Delta t}\left(V_{\text{target}} + V^{n-1} - 2\,V^n\right) \tag{5.9}$$

where S_1 represents the source term in the x-direction that is constant in space but may vary in time. The average cross-sectional flow velocity was denoted by V and $\alpha = 0.3$ is a dimensionless coefficient used to ensure the stability.

5.3 Numerical model validation

As mentioned in the introduction to this work (section 1.3), the validation test cases selected are turbulent flat-channel flow, turbulent flow in a channel with periodic hill constrictions and turbulent flow around a single and compound piers on the eroded bed. The turbulent channel flows with smooth wall surfaces are well-known case studies, which have been widely investigated during last years and the corresponding experimental and numerical results are available for the comparison study. In addition, a flat-channel simulation can provide LES inflow conditions for the

bridge pier studies. The single pier case (with rough bottom bed) helped to evaluate the capability of the present numerical model to capture the main flow features around a single bridge pier on the eroded bed, which are already well known (as summarized in Chapter 2). Further, the corresponding experimental bed shear stress results, available for this case, enabled to assess the accuracy of the present numerical results. Finally, turbulent flow around a compound pier on eroded (rough) bed was also predicted, because the corresponding experimental velocity profiles at different longitudinal positions on the vertical symmetry plane are available, making the accuracy study straightforward.

5.3.1 Turbulent flat-channel flow

The LES calculations were performed for a flat-channel flow at $\mathrm{Re}_\tau = u_* h/\vartheta = 590$ (where h represents the channel half-height as shown in Figure 5.3 (left)). For this case, the corresponding DNS results of Moser et al. (1999) was selected as reference data. Since the DNS method uses the Navier-Stokes equations directly, it was decided to switch off the wall model only for this specific validation. This decision helped to evaluate the accuracy of the present numerical model by the sole use of the LES Smagorinsky model.

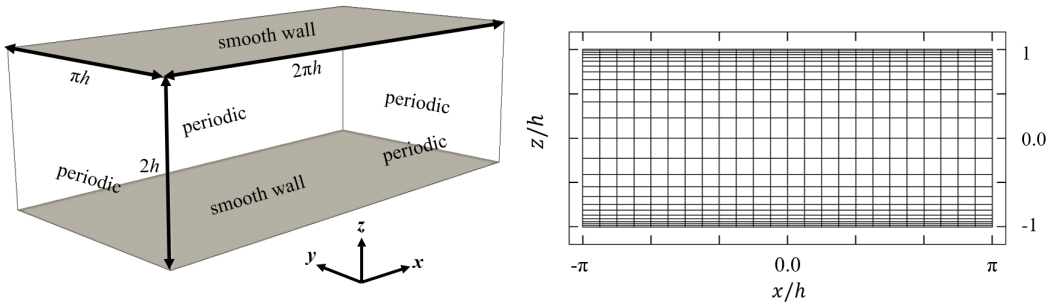

Figure 5.3: Flat-channel case: (left) computational domain with the corresponding dimensions and boundary conditions; (right) side view of the grid (every 5$^{\text{th}}$ grid line is shown).

The computational domain dimensions ($2\pi h \times \pi h \times 2h$) are in accordance with the referenced DNS-study (see Figure 5.3 (left)). Stationary smooth walls were located at the bottom and top of the domain and periodic boundary conditions were applied in the x- and y- directions in accordance with the reference study. A side view of the grid used in this case is presented in Figure 5.3 (right). The grid system is uniform in the x- and y- directions. In the vertical direction z, the grid cell

height was minimized close to the wall surfaces in such a way that three sequent grid points in the normal direction to the wall were located within the viscous sub-layer (i.e., fully-resolved LES). The Van Driest wall damping function, equation 4.17, was then employed for only this case to guarantee that the eddy viscosity is reduced near the wall surfaces. In overall, 120 grid cells were used for each direction.

The LES calculations were carried out first for 20 flow-through times (i.e., $20 \times 2\pi h/V$, where V represents the average cross-sectional flow velocity) to remove the initial condition effects from the calculations and to allow the 3-D flow structures to be developed. Then, the flow field was averaged in space (longitudinal and transverse directions) and in time over an extra long period of 40 flow-through times. The corresponding LES results obtained in this study and also, for comparison, the DNS results reported by Moser et al. (1999) for the same flow conditions are presented in Figure 5.4.

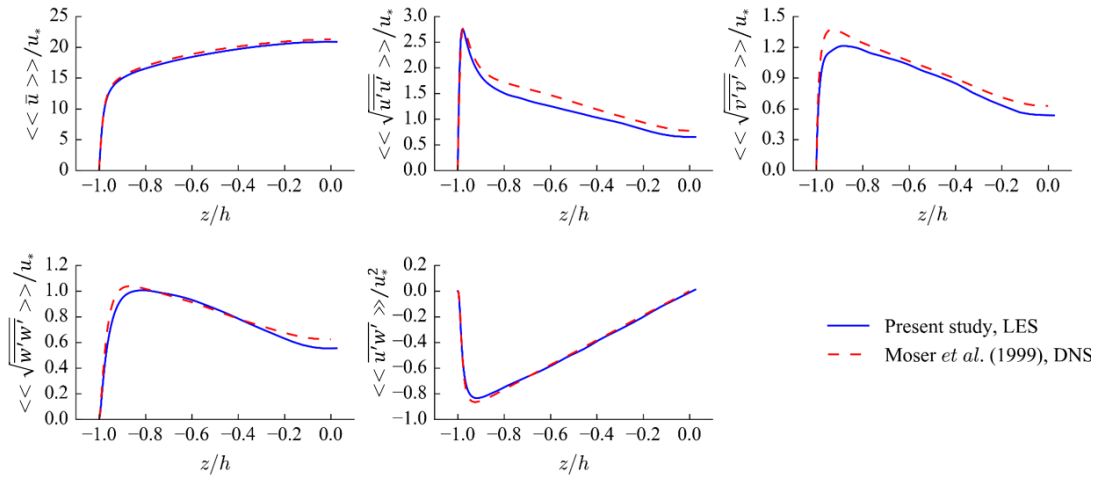

Figure 5.4: Comparison of the LES results with the corresponding DNS results for a turbulent flat-channel flow at $\mathrm{Re}_\tau = 590$ (the flow quantities were averaged in space, longitudinal and transverse directions, and in time).

The obtained LES results show that the mean u-velocity profile was well predicted in this study. Also, the vertical distributions of the Reynolds shear stress term (represented as $\overline{u'w'}$) and of the r.m.s. values of the velocity components fluctuations are in good agreement with the DNS results. The small differences between those (in some regions) can be attributed to the fact that in the DNS method, all turbulent scales are resolved temporally and spatially, while in the LES

calculations, the large-scale motions of the turbulent flow are computed directly and the small-scale motions are modeled using a subgrid-scale model. It should be noted that the results of a grid sensitivity analysis performed (not shown here) indicated that the differences are minimized by refining the grid, particularly in the region close to the wall surfaces.

5.3.2 Periodic hill-channel flow

Prediction of the flow separation from a curved surface is also important for the numerical model validation. Therefore, in this study, the flow over periodically arranged hills in a channel was selected as a benchmark test case to evaluate the accuracy of the present numerical model in the flow separation characteristics. Details of the benchmark case and the corresponding experimental and numerical reference results are available on the ERCOFTAC database (http://178.250.48.186/w/index.php/Abstr:2D_Periodic_Hill_Flow).

The geometry of the test case is shown in Figure 5.5 (left). The size of the computational domain is $9h$, $4.5h$, and $3.036h$ (here h denotes the height of the hill) in the x-, y- and z- directions, respectively. Periodic boundary conditions were applied in the x- and y- directions similar to the flat-channel case. A smooth wall was located at the top of the computational domain and the hill geometry (solid smooth-surface) was positioned at the bottom of the domain. The hill geometry is mirrored at $x = 4.5h$ and its definition was obtained through equation 5.10.

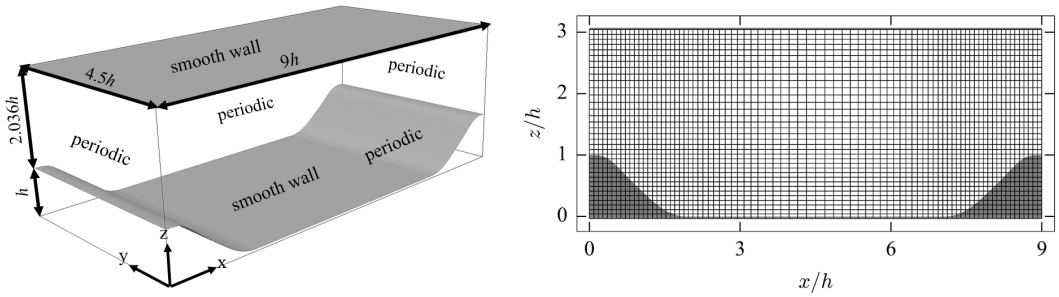

Figure 5.5: Periodic hill-channel case: (left) computational domain with the corresponding dimensions and boundary conditions; (right) side view of the grid (every 3th grid line is shown).

$$
\begin{aligned}
0 \le x \le 0.3214h: \; z(x)/h &= \min\left(1,\; 1+0.1897x^2-1.6656x^3\right) \\
0.3214h < x \le 0.5h: \; z(x)/h &= 0.89548+0.97548x-2.8451x^2+1.4816x^3 \\
0.5h < x \le 0.7143h: \; z(x)/h &= 0.92129+0.82067x-2.5355x^2+1.2752x^3 \\
0.7143h < x \le 1.0714h: \; z(x)/h &= 1.4452-1.3796x+0.54485x^2-0.16231x^3 \\
1.0714h < x \le 1.4286h: \; z(x)/h &= 0.64016+0.87439x-1.5589x^2+0.49217x^3 \\
1.4286h < x \le 1.9286h: \; z(x)/h &= \max(0,\; 2.0139-2.0105x+0.46058x^2+0.02097x^3) \\
1.9286h < x \le 4.5h: \; z(x) &= 0
\end{aligned}
\tag{5.10}
$$

For this hill case (also for all the following cases), the numerical prediction was performed by employing the wall model, equation 5.3, helping to evaluate its accuracy in predicting separated flows. Moreover, according to Roulund et al. (2005), it allows using a coarse mesh resolution near the wall boundaries, reducing the total number of grid cells compared to that by the sole use of LES. A side view of the grid used for this case was shown in Figure 5.5 (right). The grid system is uniform in the y-direction, while in the x- and z- directions, the grid is finer in the zone near the wall boundaries and is coarser out of it. The model domain for the hill case consists of about 2.9 million cells ($246\times113\times106$). From those, about 2.6 million cells are partially or fully open to the flow. In fact, since the model domain comprises a single mesh-block, some grid cells were completely blocked by the solid geometries.

The LES calculations were performed for Reynolds number 10595 ($\mathrm{Re_b} = U_b h/\vartheta$, in which U_b is the bulk velocity at the crest of a hill with height h). A global view of the corresponding flow structure is shown in Figure 5.6, picturing the streamlines obtained by means of the flow field averaged in the transverse direction and over a long period of 10 flow-through times. According to the present LES results, the flow separates at the hill crest at about $x = 0.2h$ and reattaches at about $x = 4.3h$. The corresponding reattachment point was experimentally observed by Rapp & Manhart (2011) at $x = 4.21h$ - $4.28h$ for the same flow conditions. In addition, the corresponding fully-resolved LES calculations of Breuer et al. (2009) predicted that the flow separation occurs at about $x = 0.19h$ and the reattachment at about $x = 4.69h$.

The time- and transverse- averaged u- and w- velocity profiles ($<\bar{u}>$ and $<\bar{w}>$) at $x = 2h$, $4h$ and

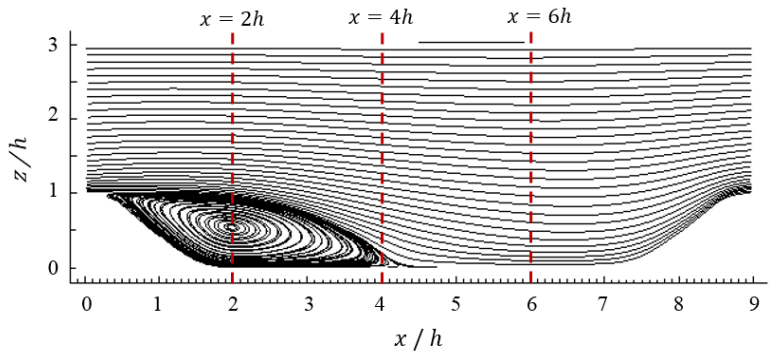

Figure 5.6: Streamlines of the time-and transverse- averaged flow field (hill-channel case, present study).

6h (near the mid-length, near the end and downstream of the recirculation region, respectively) are presented in Figure 5.7 and compared with the corresponding experimental and numerical reference results (ERCOFTAC database). Furthermore, profiles of the transverse-averaged Reynolds shear stress ($\overline{u'w'}$) are presented in Figure 5.7.

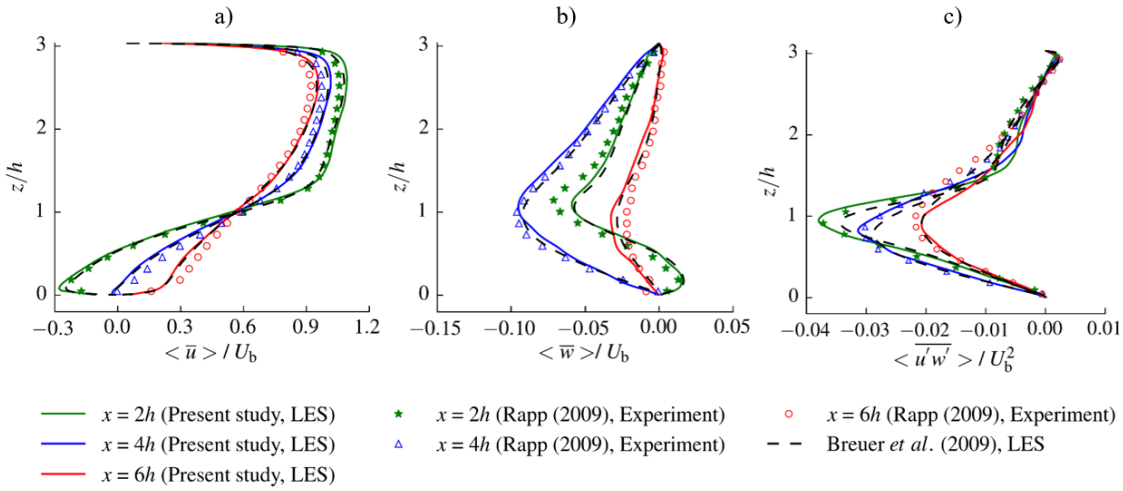

Figure 5.7: Comparison of the present LES results for the hill-channel case with reference data (obtained from the ERCOFTAC database) at three different positions x=2h, 4h and 6h (the flow quantities were averaged in the transverse direction and over time).

The predicted vertical distributions of $<\bar{u}>$ and $<\bar{w}>$ and the corresponding peak values are in accordance with LES results of Breuer et al. (2009) and both are in good agreement with experimental reference results (ERCOFTAC database). It is noteworthy to recall that the numerical calculations of Breuer et al. (2009) were performed based on the fully-resolved LES, while in the present study, a wall model was used in the LES calculations. Concerning the Reynolds shear

stress ($\overline{u'w'}$), at about $z = 2h$ (where the vertical size of the grid cells is maximum), the present LES results slightly deviated from the experimental results but in the rest of the regions over depth, values of $<\overline{u'w'}>$ were correctly predicted (particularly the peak values). Overall, the present numerical results can be considered quite well, indicating the adequacy of the present wall model in predicting separated flows.

5.3.3 Single bridge pier on an eroded bed

In both channel cases presented in sections 5.3.1 and 5.3.2, the wall surfaces were smooth and the flow was assumed periodic in the longitudinal direction. At this stage, and taking into account the aimed goal of the work, the turbulent flow around a circular pier on an eroded rough-bed was predicted (by assuming the inflow-outflow boundary conditions in the longitudinal direction) for the same pier geometry and flow conditions of the experiment conducted by Graf & Istiarto (2002). The pier diameter (D), mean approach flow velocity (U_∞) and the flow depth (h) were 0.15 m, 0.45 m/s and 0.18 m, respectively. Therefore, the corresponding Reynolds number is $\mathrm{Re}_D = 67500$ ($\mathrm{Re}_h = 81000$). Moreover, the bed material was a uniform sand with mean diameter $d_{50} = 2.1$ mm. Graf & Istiarto (2002) measured the velocity components at the equilibrium stage of the scour hole process using an acoustic Doppler velocity profiler. Although the corresponding bed bathymetry was not reported by Graf & Istiarto (2002), the maximum scour depth and horizontal extension of the scour hole upstream and downstream of the pier are available. For the present numerical study, the deposition dune that would be expected to be formed downstream of the scour hole (far away from the pier) was neglected and the scour hole definition upstream ($x \leq -D/2$) and downstream ($x \geq D/2$) of the pier was obtained through equations 5.11 and 5.12, having in attention that the portions of the scour hole surface upstream and downstream of the pier have been reported to be a half inverted cone and a parabolic surface, respectively (Pournazeri et al., 2014). For $-D/2 < x < D/2$, the scour hole definition was obtained by linear interpolation between those equations.

$$\left(\frac{z+0.3}{0.3}\right)^2 = \left(\frac{x}{0.45}\right)^2 + \left(\frac{y}{0.45}\right)^2, \quad x \leq -D/2 \tag{5.11}$$

$$\left(\frac{z+0.2}{0.2}\right)^2 = \left(\frac{x}{1.05}\right)^2 + \left(\frac{y}{0.45}\right)^2, \quad x \geq D/2 \tag{5.12}$$

In accordance with the experimental data, the longitudinal extensions of the scour hole upstream and downstream of the pier are, respectively, 0.45 and 1.05 m from the pier center. Moreover, the maximum depth of the scour hole is 0.25 m at the upstream side of the pier and 0.19 m downstream of the pier.

The computational domain contains two layers, defined as the top and the bottom layers. The top layer depth was considered equal to the water depth h and the bottom layer depth, h', was considered approximately equal to the maximum scour depth as shown in Figure 5.8. For this case, the inlet boundary section was located $10D$ upstream from the pier center and the approach fluid flow at this boundary was considered to follow a logarithmic velocity profile. At the outlet section, located $20D$ downstream from the pier center, the convective boundary condition was applied to the velocity components using equation 3.25. The remaining outer domain surfaces were treated as a free-slip rigid lid. Kirkil et al. (2009) reported that the rigid lid approximation on the top boundary (water surface) is widely used for simulating flows with channel Froude number less than 0.5. In fact, in accordance with the investigation of Roulund et al. (2005), the water surface changes around a single pier are very small for small Froude numbers. It is to be noted that the Froude number for this case is 0.34.

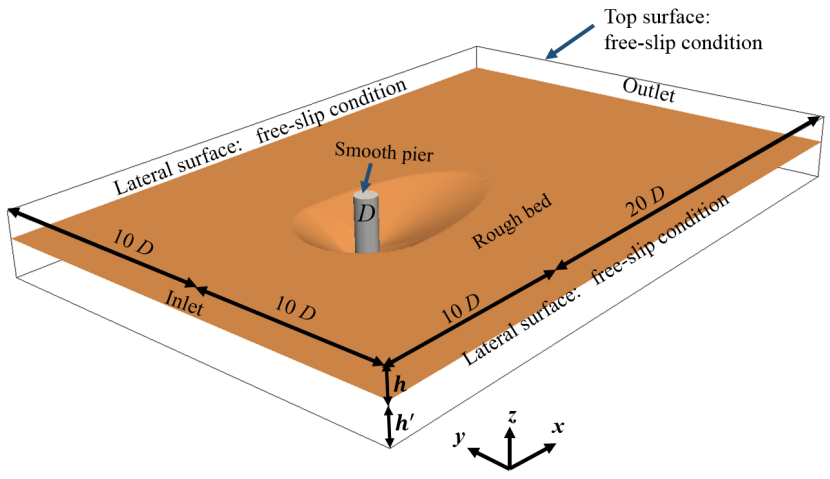

Figure 5.8: Computational domain and boundary conditions for the single pier case.

A structured grid with orthogonal grid lines was employed such that the grid is finer near the pier position and progressively coarser out of it as exemplified in Figure 5.9. The grid consists of about 2.5 million grid cells ($195\times180\times70$) with variable sizes. The minimum grid spacing size in

the x- and y- directions is equal to $0.02D$. That size was enlarged gradually (with expansion ratio about 1.05) with increasing the horizontal distance from the pier. Furthermore, the grid points' locations in the vertical direction were defined as uniform in the bottom layer (bed layer). The corresponding grid spacing size was $0.03h$ (taking into account the bed roughness height) and was enlarged (with expansion ratio about 1.025) above the scour hole towards the top domain surface. Overall, the selected grid is relatively coarse, aiming to assess if the present LES with the wall model can properly represent the important flow structures forming around the single pier in the presence of a scour hole.

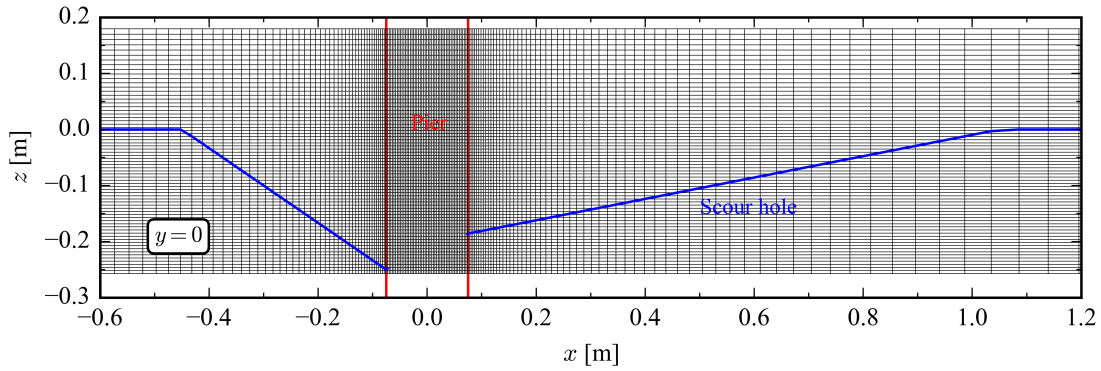

Figure 5.9: Computational grid at the vertical symmetry plane for -4$D \leq x \leq$ 8D (D = 0.15 m), single pier case.

The time-averaged flow structure around the single pier is shown in Figure 5.10. The predicted main flow features are the down-flow in front of the pier, the horse-shoe vortex system at the pier's base, the flow acceleration around the flanks of the pier and the wake flow behind the pier. According to the present results, the approach flow is vertically diverted in front of the pier. The corresponding down-flow is then deflected at the pier's base and rolls up to form the horse-shoe vortex system, comprising a number of necklace-like structures, which wraps around the pier's base and extends downstream of the pier before losing its identity. Moreover, the approach flow is also deflected sideways by the pier body and accelerated into the zones adjacent to both sides of the pier. In addition, the boundary layer over the pier surface separates and a wake zone is formed behind the pier.

Details of the main necklace vortices upstream of the pier are shown in Figure 5.11 by means of picturing the streamlines at the vertical symmetry plane inside the scour hole. Dark blue and dark

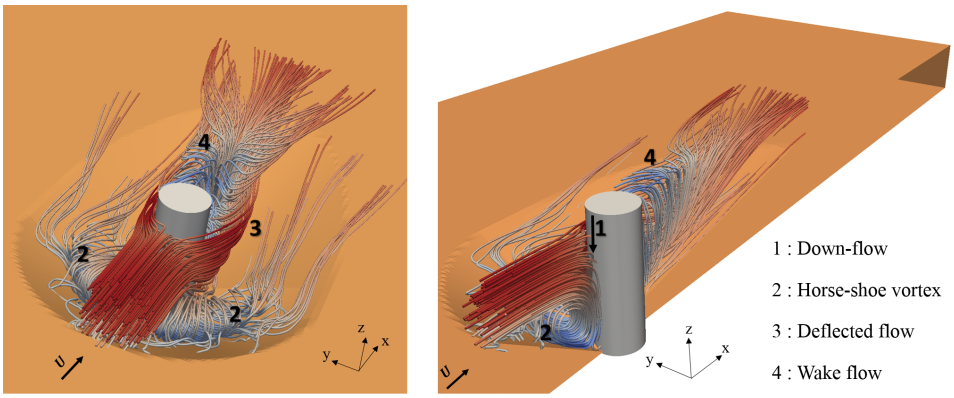

Figure 5.10: Time-averaged flow structure around a single pier located on eroded bed, present study.

red colors indicate the minimum and maximum values of the predicted $\bar{u}$-velocities in the pictured zone. In front of the pier, inside the scour hole, the flow is more complex than that for the hill-channel case (section 5.3.2) as several vortices are observed for this pier case. A large and strong vortex (V2) along with a small neighboring vortex (V1) were predicted directly upstream of the pier. The flow near the bed, beneath V2, is directed upstream of the scour hole (negative $\bar{u}$-velocity values), while the corresponding flow beneath V1 is directed downstream (positive $\bar{u}$-velocity values). In other words, those vortices are counter-rotating: the biggest vortex V2 rotates in the clockwise direction, while the neighboring vortex V1 rotates in the opposite direction, contributing to transport sediments upslope and downslope of the scour hole, respectively.

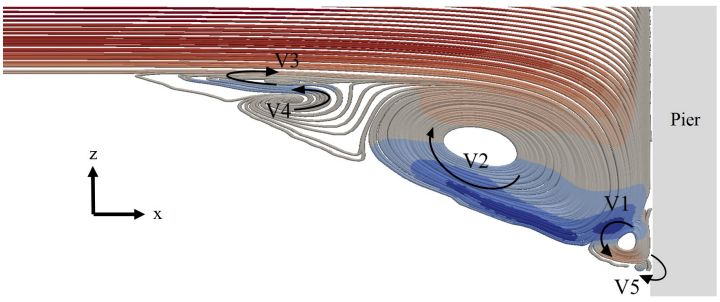

Figure 5.11: Time-averaged vortices, formed inside the scour hole, at the vertical symmetry plane $y = 0$ upstream of the single bridge pier.

Furthermore, the approach flow separates at the upstream edge of the scour hole due to the change in the bed surface slope and a clockwise vortex (V3) is formed immediately after that edge. Then, a counter-clockwise vortex (V4), attached to the bottom, is present just downstream of V3. These vortices, created upstream of V2, are weaker and may not support the transport of

sediment particles as strongly as V2 or even V1 does. Similar physical observations and numerical predictions were reported by Graf & Istiarto (2002) for the same Reynolds number as used in this study and by Kirkil et al. (2008) for Re_D = 16000 (Re_h = 18000). In addition to the above-mentioned vortices, the present numerical simulation predicted a very small vortex (V5) at the junction of the pier's base and the bed surface that might be due to the bed geometry definition considered for this study (i.e., sharp junction of the pier and bed surface compared to a ring-shaped portion in Figure 2.2 b)). It is noteworthy to mention that the experimental measurements of Graf & Istiarto (2002) could not be performed at the location where V5 was numerically predicted.

To characterize the local flow structure caused by the pier, the time-averaged 2-D streamlines around the single pier at two different horizontal planes z = -10 cm (inside the scour hole) and z = 5 cm (above the scour hole) are presented in Figure 5.12. Overall, the predicted flow pattern is symmetric. A reverse flow region is observed at the upstream part of the scour hole, Figure 5.12 a), corresponding to the horse-shoe vortex system reported above (Figure 5.11). Moreover, one can clearly see that the pier deflects the incoming flow to both sides of the pier but, downstream of it, the deflected flow redirects to the symmetry line y = 0. The position of the boundary layer separation points from the pier surface and, consequently, the wake zone size changes over the height of the pier because the flow features are not uniform over the flow depth. In fact, by comparing the separation points at z = -10 cm and z = 5 cm, as signaled by the red lines in Figure 5.12, the separation points at the pier surface inside the scour hole occur further downstream compared to the upper section of the flow what is in accordance with the experimental observations of Ataie-Ashtiani & Aslani-Kordkandi (2012). Concerning the upper level z = 5 cm, above the scour hole, the flow structure predicted is different from that was obtained for an infinite circular cylinder (see Figure 4.7 b)) what can be attributed to the presence of the bottom scour hole in this case (single pier). Overall, the predicted flow behavior around the single bridge pier on the scoured bed is in accordance with the literature.

Graf & Istiarto (2002) estimated the bed shear stress values at the symmetry plane y = 0 by two processes, using either time-averaged velocities or Reynolds shear stresses ($-\rho\overline{u'w'}$) and could conclude that the results obtained by means of the former are more reliable than those with the

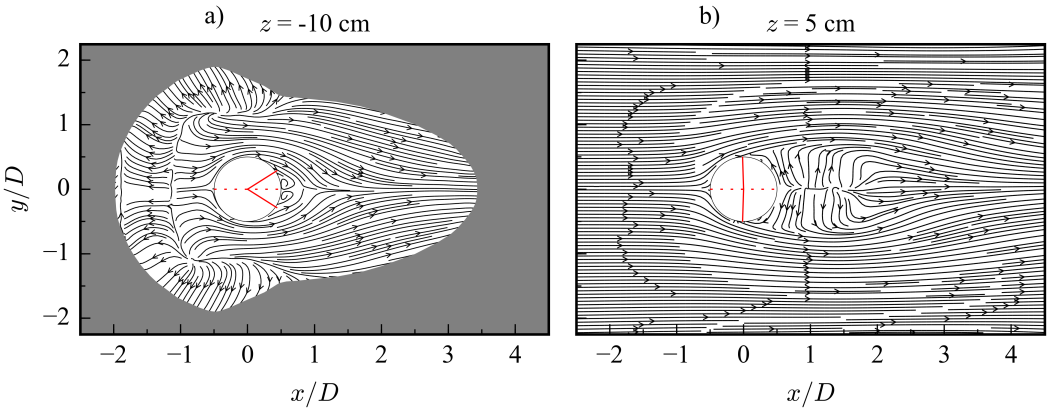

Figure 5.12: Time-averaged 2-D streamlines around the single bridge pier at horizontal planes: a) z = -10 cm and b) z = 5 cm.

latter. Concerning the process using the time-averaged velocities, Graf & Istiarto (2002) first obtained the velocity parallel to the bed surface (at a normal distance of x_2= 4 mm) and then estimated the corresponding bed shear stress through $\tau = \rho \vartheta_t \partial u_t / \partial x_2$, in which ϑ_t was taken as the measured eddy viscosity in the approach flow (1.3×10^{-5} m^2/s). In the present numerical study, the bed shear stresses were obtained by two different methods: (*i*) by using $\tau = \rho \vartheta_t \partial u_t / \partial x_2$ to facilitate a direct comparison between the numerical (present LES study) and experimental (Graf & Istiarto, 2002) data; (*ii*) estimating the local friction velocity, u_*, through equation 5.3 such that the corresponding bed shear stress was computed by $\tau = \rho {u_*}^2$. In the present study, the velocity components parallel to the bed surface were determined at the center of the cells near the bed (corresponding wall normal distances are about 5 mm) using the time-averaged velocity values available in the staggered grid system. The corresponding bed shear stress distribution along the symmetry plane upstream and downstream of the single pier is presented in Figure 5.13.

Overall, there is a good agreement between the numerical and experimental results. Upstream of the pier, inside the scour hole, the bed shear stress values change non-linearly since several vortices exist in that zone. Downstream of the pier, the bed shear stresses progressively increase with distance from the pier until the downstream edge of the scour hole. A major point is that the bed shear stresses, specifically those predicted using equation 5.3, are too small at the upstream part of the scour hole. For further evaluation, the corresponding spatial distribution of the friction velocity is presented in Figure 5.14. By it, one can conclude that the smaller values of the bed

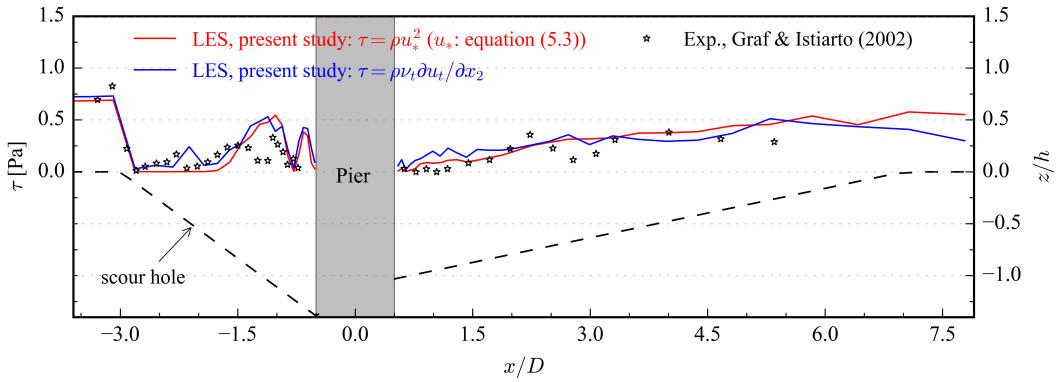

Figure 5.13: Time-averaged bed shear stresses at the symmetry plane $y = 0$, single pier case.

shear stress in the scour hole were developed in the region beneath the (weak) vortices V3 and V4. Link et al. (2008) reported that V3 and V4 are weaker than and not as stable as V2. Therefore, the bed slope beneath those vortices would be expected to be smaller than the bed slope at V2 (see Figure 2.2 b)). That means that as a constant slope was assumed upstream of the pier for this numerical study, the scour hole geometry considered may have affected the predicted friction velocity values.

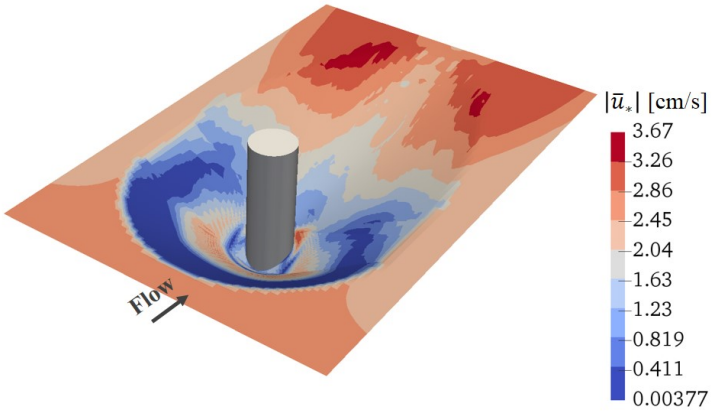

Figure 5.14: The friction velocity distribution around the single pier, obtained through equation 5.3 using the time-averaged velocity field.

It should be noted that the map's pattern presented in Figure 5.14 is similar to that reported by Kirkil et al. (2008) and Bayón-Barrachina et al. (2014) as shown, respectively, in Figure B.2 (see also Figure 2.3) and Figure B.3 of Appendix B. Nevertheless, Kirkil et al. (2008) and Bayón-Barrachina et al. (2014) did not clearly report the predicted small values. It is worth to note

here that although the present study is related to the equilibrium stage of the local scour process, Melville & Raudkivi (1977) attributed the sediment motion in the local pier scour to the combined effect of temporal mean shear stress, sediment weight and turbulent agitation of the flow field (as reported by Radice & Tran (2012). In the other words, sediment entrainment can occur around a pier, even if the mean shear stresses are below the critical values (Beheshti & Ataie-Ashtiani, 2016). No more explanation was found for that behavior. Apart from that, upstream of the pier inside the scour hole, the largest values of the friction velocity are observed beneath the main vortex V2 and V1 (close to the junction line of the pier and bed surface) as expected from the results of Kirkil et al. (2008) in Figure 2.3 and Figure B.2. Downstream of the pier, the largest values of the friction velocity were predicted near the crest of the scour hole but still lower than the critical value of 3.69 cm/s (Graf & Istiarto, 2002). Although the depositional zone was not numerically modeled in this study due to lack of the bed geometry data, Kirkil et al. (2008) and Bayón-Barrachina et al. (2014) also predicted the largest values of the friction velocity near the downstream edge of the scour hole due to the flow acceleration in that region.

5.3.4 Compound pier on an eroded bed

As an ultimate validation case, the turbulent flow around a compound pier on the scoured bed was numerically predicted for the same pier geometry and flow conditions of the experiment conducted by Kumar & Kothyari (2012). For this case, compared to the single pier case, numerically predicted velocity profiles and velocity components fluctuations are compared with the ones obtained from the reference study at several different longitudinal positions on the symmetry plane. The compound pier model consists of a circular pier with diameter D = 11.4 cm supported by a circular foundation with diameter 21 cm for a configuration when the top surface of the foundation was located at z = -2.1 cm (below the initial channel bed level). The flow depth and the approach flow velocity were 0.16 m and 0.28 m/s, respectively (Re_h = 44800). Moreover, the bed material was a uniform sand with median size d_{50} = 0.4 mm, stabilized (after the local scoring process was stopped) by spraying a light solution of cement that enabled the velocity measurements on a rigid bed.

The corresponding bed bathymetry (Kumar & Kothyari, 2012), developed after 7 hours (intermediate stage of the scour hole process), is shown in Figure 5.15 (left). For the present numerical study, the bed geometry was generated based on it. The bed level at any point between the available contour lines was determined by linear interpolation between the closest bed elevations data. The sediment deposition data were available for this case and thus were used to generate the bed model as shown in Figure 5.15 (right). For this compound pier case, the domain dimensions and the boundary conditions were selected the same as for the single pier case (section 5.3.3) and those are resumed in Figure 5.15 (right).

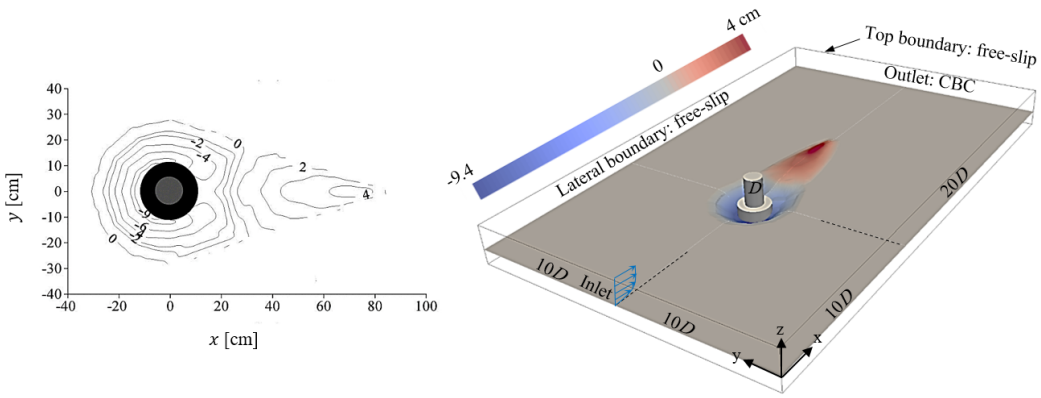

Figure 5.15: Compound pier case: (left) bed bathymetry (Kumar & Kothyari, 2012); (right) computational domain dimensions and boundary conditions.

The numerical calculations were performed on a non-uniform grid system with $313\times254\times85$ (about 6.8×10^6) cells over the x-, y- and z- directions, respectively. The smallest grid cell size in the horizontal xy plane ($\delta x = \delta y = 0.0175D$, D the pier diameter) was defined all along the circular foundation cross-section in both x- and y- directions. That small size was enlarged gradually (with expansion ratio of about 1.035) in the horizontal plane as the distance from the foundation increased. In the vertical direction, the grid points were distributed uniformly ($\delta z = 0.0125h$) over depth of the bed model (h') until the channel bed level and then the grid point spacing was gradually increased with an expansion ratio of about 1.035 up to the top boundary surface.

The time-averaged streamlines, obtained numerically at the longitudinal vertical plane $y = 0$, are shown in Figure 5.16. The corresponding experimental results (velocity vectors) of Kumar & Kothyari (2012) are presented in Figure B.4 of Appendix B. Overall, the present LES could repre-

sent more details about the flow structure, particularly upstream of the pier inside the scour hole, than the referred experimental study. According to the present numerical results, the downward flow in front of the pier foundation is deflected to upstream and downstream of the scour hole bed bank at the bottom bed, forming a big vortex V2 and a small junction vortex V1. In addition, two counter-rotating vortices (V3 and V4) were predicted upstream of V2. The predicted flow structure in front of the circular pier foundation is similar to that observed for the single pier case (see Figure 5.11). Downstream of the pier, the reverse flow region was predicted behind the pier, with its horizontal length being maximum at the top domain boundary. Downstream of the reverse flow region, the flow is mostly directed upwards what fosters sediment transport downstream of the scour hole.

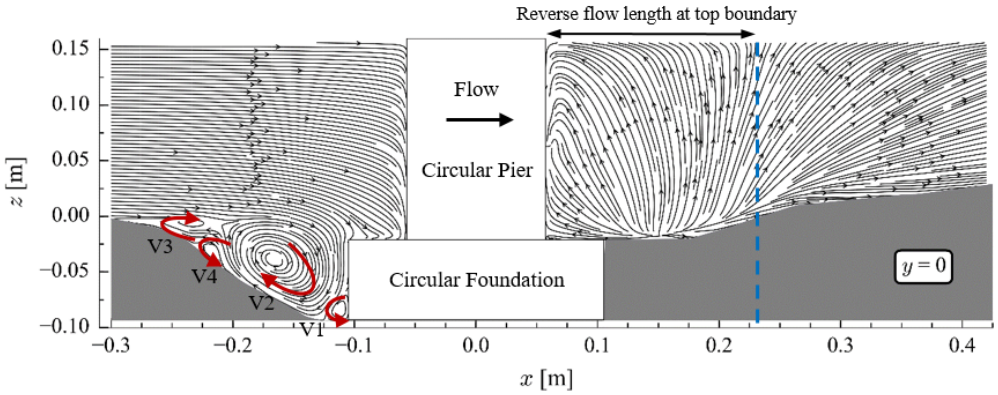

Figure 5.16: Time-averaged streamlines at the symmetry plane $y = 0$, present study, compound pier case.

For an in-depth evaluation, $\bar{u}$-velocity profiles were extracted at six different longitudinal positions on the symmetry plane $y = 0$ and compared with the corresponding experimental measurements of Kumar & Kothyari (2012) in Figure 5.17. Overall, the present LES results are in agreement with the ones obtained from the reference study, however, $\bar{u}$-velocity values at $x = 0.14$ m are under-predicted over local water depth. The difference is maximum at a region close to the bed and is minimized when mowing towards the top domain boundary. In other words, longitudinal length of the reverse flow (negative $\bar{u}$-velocity) region close to the bed was numerically predicted larger than that in the experimental study. Nevertheless, the predicted size at the top domain boundary is in good agreement with the physical observation of Kumar & Kothyari (2012). The difference may be attributed to the quality and accuracy of the bed model downstream of the

pier that, as mentioned before, was made by linear interpolation between the bed contour lines provided by Kumar & Kothyari (2012). In fact, any difference between the bed level of the experimental study and the one obtained and used for the numerical simulation affects the local water depth and consequently leads to different velocity values over the depth. Nevertheless, it should be noted that the corresponding experimental and numerical $\bar{w}$-velocities and r.m.s. values of the velocity components fluctuations at x = 0.14 m, as well as at x = 0.25 m, are in good agreement as shown in Figure 5.18.

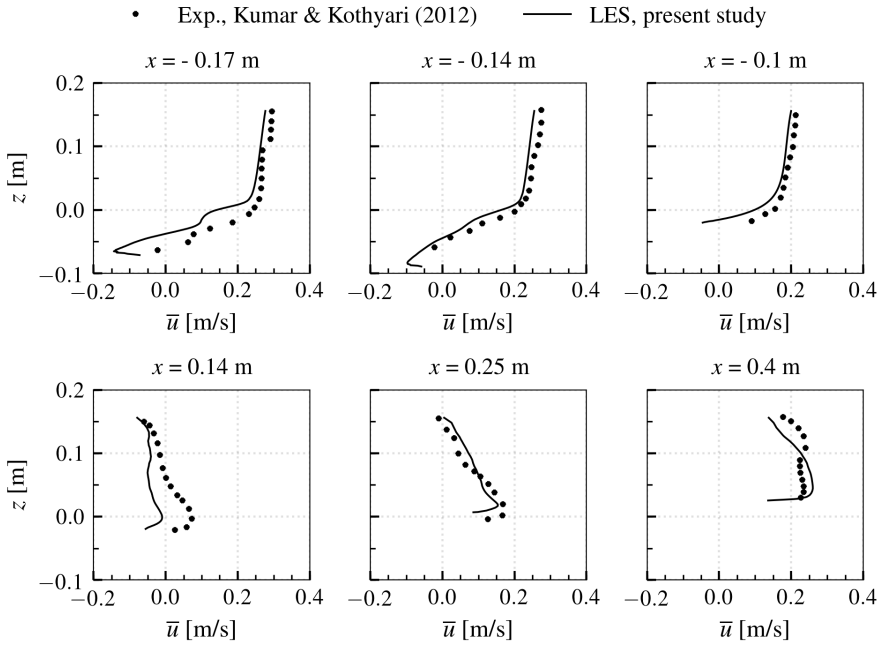

Figure 5.17: Comparison of the present LES results ($\bar{u}$-velocity values) with the experimental results at different positions x = -0.17, -0.14, -0.1, 0.14, 0.25 and 0.4 m (measured from the pier center), compound pier case.

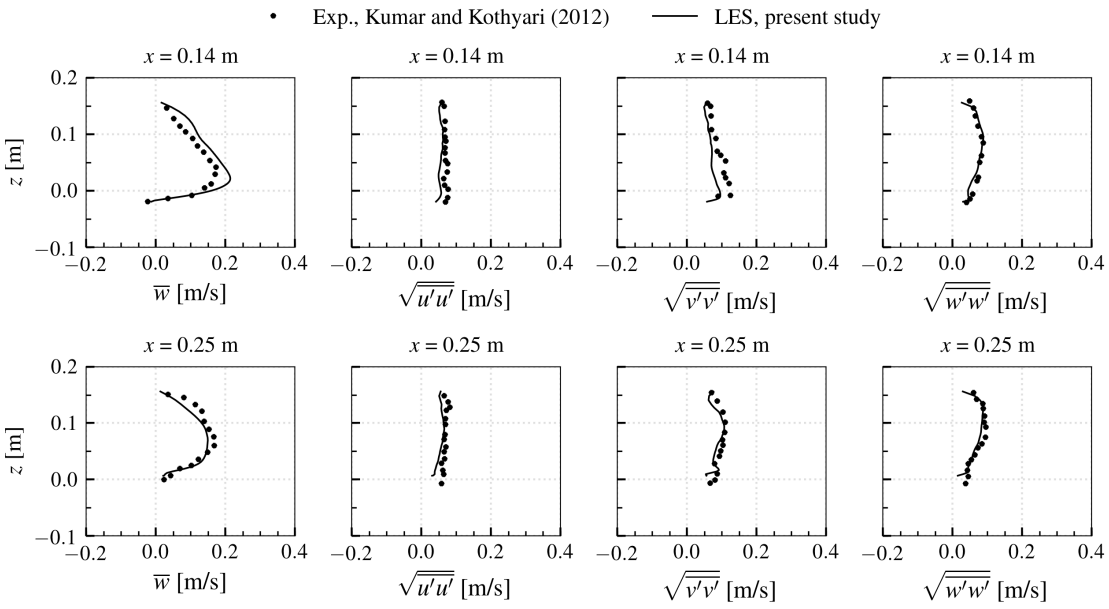

Figure 5.18: Comparison of the present LES results ($\bar{w}$-velocities and r.m.s. values of the velocity components fluctuations) with the experimental results at different positions downstream of the compound pier case.

CHAPTER 6

Numerical Modeling of Complex Piers

6.1 Introduction

This chapter concerns the numerical modeling of the turbulent flow around complex bridge piers on the scoured bed. At this stage, one limitation was to find adequate laboratory benchmark tests for validating the corresponding numerical simulations. Nevertheless, after a bibliographic survey, two complex bridge piers (the so-called case I and II in Chapter 1) were selected for this study. The complex piers consist of a column and a pile cap supported by a group of piles; the piers of case I and II differ in the number of the piles, pile cap position and nose shape of the column and pile cap. They thus address different challenges to the simulation code, namely in the type of flow

separation around the edges of the pile cap and column (sharp vs round corners), flow structure near the pile group (1 vs 2 rows of piles).

In Chapter 2, background knowledge of the flow structure around the selected complex piers was assessed and the main contributions of the present numerical study were addressed. In fact, the present numerical simulations provide more details of the flow structure, helping to better understand and characterize the flow mechanism around those specific complex piers on the scoured bed. In addition to those discussed earlier in Chapter 2, some other experimental results are presented in this chapter, helping to evaluate the accuracy of the present numerical results.

In the following, details of the test cases and the corresponding LES results are presented and discussed in section 6.2 and section 6.3, respectively, for the complex pier case I and II.

6.2 Complex pier case I: column and pile cap with sharp corners

6.2.1 Details of the test case and numerical model setup

Numerical prediction of the flow around the complex bridge pier case I was performed for the same conditions as an experiment conducted by Beheshti & Ataie-Ashtiani (2016) to facilitate comparison between numerical and experimental results.

Beheshti & Ataie-Ashtiani (2016) experimentally investigated the turbulent flow around a specific configuration of the complex bridge pier, as shown in Figure 6.1, in the scour hole developed after 72 hours of the beginning of the scour process (considered as the equilibrium stage). The pile cap was fully submerged and above the channel bed level ($z = 0$). The approach flow depth was equal to 0.301 m and the mean approach flow velocity was 0.358 m/s ($\mathrm{Re}_h \sim 10^5$ and Fr = 0.21). Moreover, the bed material was a uniform sand with mean diameter $d_{50} = 0.71$ mm. For the present numerical study, the scour hole model (Figure 6.2 b)) was generated using the scour contour lines provided by Beheshti & Ataie-Ashtiani (2016) as shown in Figure 6.2 a). The reported single holes formed around each of the piles as also the deposition dune formed downstream of the scour hole were neglected for generating the scour hole model, as no adequate experimental data on those particular zones was made available.

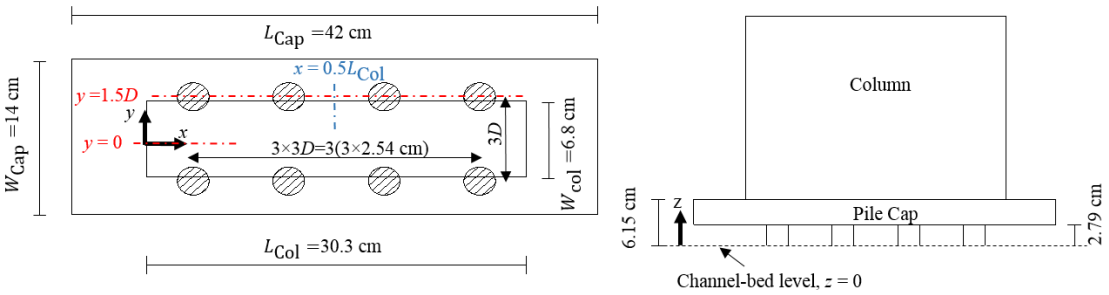

Figure 6.1: Geometry and position of the complex pier elements, complex pier case I.

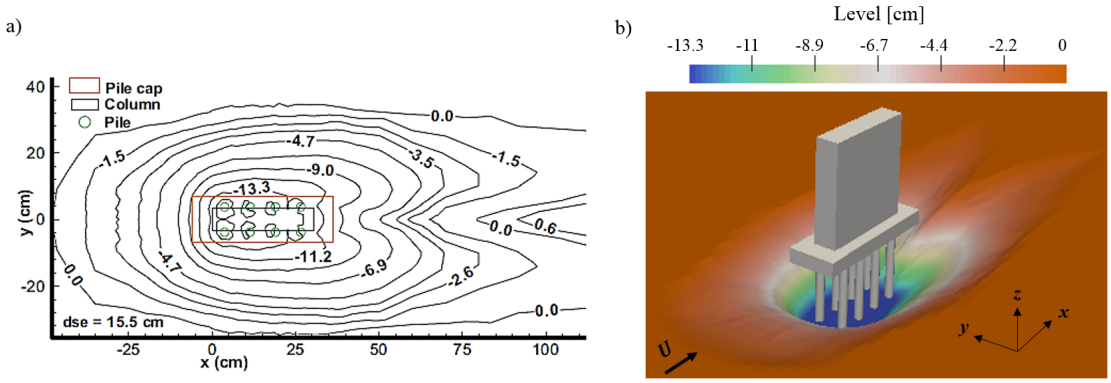

Figure 6.2: Complex pier case I: a) Scour contours at the equilibrium condition presented by Beheshti & Ataie-Ashtiani (2016); and b) scour hole model generated for the present numerical study.

The present numerical model solves the governing equations on a rectangular domain in planes perpendicular to the vertical axis. The corresponding computational domain, as shown in Figure 6.3, extends 7.5W_{cap} upstream of the column (i.e., the upstream face of the column where x = 0) and 17.5W_{cap} downstream of it. The domain width is 15W_{cap} such that the complex pier was located in the mid-width of the domain. Here, W_{cap} (pile cap width) was selected to determine the domain dimensions because it is the widest among all of the complex pier elements. Finally, the domain depth (h+h') was selected in such a way that it covers the water depth and the corresponding maximum scour depth. For the governing equations, the convective boundary condition for the velocity was applied at the outlet section, while velocity profiles were imposed at the inlet. Concerning the velocity profiles, a previous flat-channel simulation was used to provide the time series of the instantaneous velocity components. The free-slip boundary condition was applied at the two lateral sides of the domain. In addition, the top domain surface was modeled using the free-slip condition, having in attention that the Froude number is small for this case.

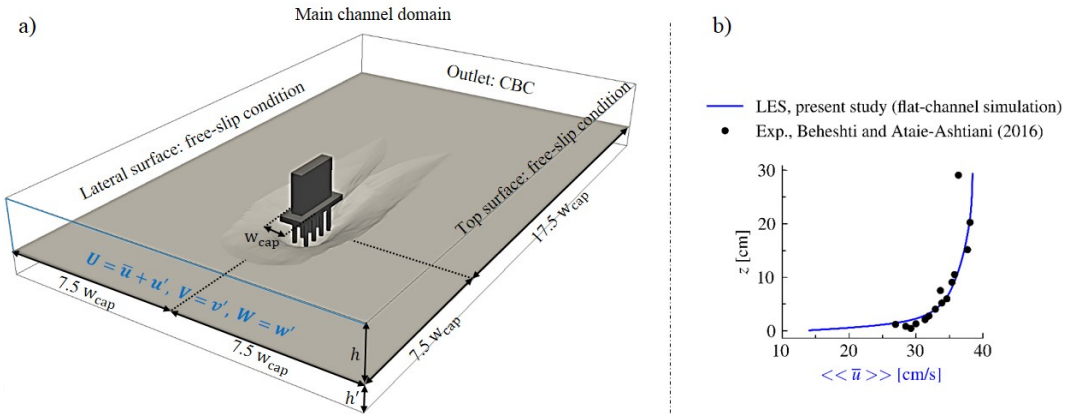

Figure 6.3: Computational domain dimensions and boundary conditions for the complex pier case I.

A structured grid with orthogonal grid lines was generated regarding the position and size of the complex pier elements. The resulting grid contains about 7.9 million grid cells (448×234×75) with variable sizes such that it is finer in the zone near the bed and pier elements and coarser out of it as shown in Figure C.1 (Appendix C). The near-wall boundary layer was not fully resolved, aiming to reduce the corresponding computational efforts. Since the quality of the LES calculations largely depends on the grid resolution, the fraction of unresolved kinetic energy or the so-called turbulence resolution (TR) in section 4.2.2 was computed for each grid cell. As shown in Figure 6.4, in most of the grid cells (88% of the cells which contain the fluid flow), the corresponding TR value is less than 0.2 what translates at least resolution of 80% of the kinetic energy in those cells. This is in agreement with Pope's criterion that the LES requires resolution of 80% of the kinetic energy and thus the carried out LES is judged as fairly well-resolved.

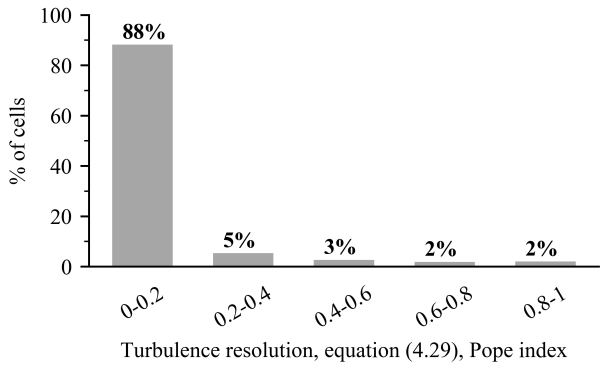

Figure 6.4: Turbulence resolution, complex pier case I.

Finally, it should be noted that the time-step size used in the numerical calculations was 0.00075 s and the temporal averaging of the results was performed over about 45000 time-steps after removing the initial condition effects from the calculations. In fact, following the investigation of Beheshti & Ataie-Ashtiani (2016) on the power spectrum at different points in the wake of the column and pile cap, the corresponding frequencies of the wake vortices (about 1.1 Hz) were used to pre-define the time-integration period for the present numerical study. Therefore, for this case, the flow quantities were averaged over time for about 35 vortex shedding periods. The corresponding CPU time was about 10 days using 16 processors.

6.2.2 Results and discussion

The complexity of the flow around the complex pier case I is shown in Figure 6.5, picturing the time-averaged 3-D streamlines. Several vortices with different shapes are observed in the mean flow. On top of the pile cap, two main vortex systems (one vertical and other horizontal) are identified on each side of the column. In addition, the wake vortex system is detected behind the column. Along the pile cap side face, a small roller was predicted with its main axis parallel to the main flow direction. The horse-shoe vortex system is observed inside the scour hole, although that could not be perceived by the experimental reference study (Beheshti & Ataie-Ashtiani, 2016). Moreover, a recirculation zone was also predicted below the pile cap (after the lower upstream edge of the pile cap) towards the upstream piles. Finally, although that is not apparent from Figure 6.5, a wake region was also predicted behind the piles, as well as the pile cap, and it will be discussed following the presentation of the results in 2-D planes made in sections 6.2.2.1 and 6.2.2.2.

6.2.2.1 Flow features in vertical planes

The time-averaged u- and w- velocity values at two different vertical planes, $y = 0$ and $y = 1.5D$, are presented in Figure 6.6. For comparison, the corresponding experimental results of Beheshti & Ataie-Ashtiani (2016), available for the plane $y = 0$, are shown in Figure 6.7. The vertical plane $y = 0$ is the symmetry plane and the plane at $y = 1.5D$ includes the four in-line piles axis as shown in Figure 6.1. Further, the numerically obtained 2-D streamlines at $y = 0$ and $y = 1.5D$ are presented, respectively, in Figure 6.8 and Figure 6.9.

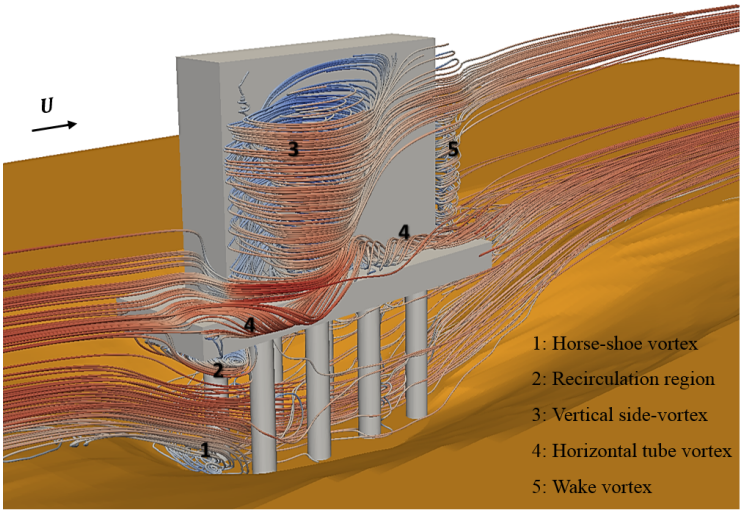

Figure 6.5: Time-averaged streamlines around the complex bridge pier case I, present study.

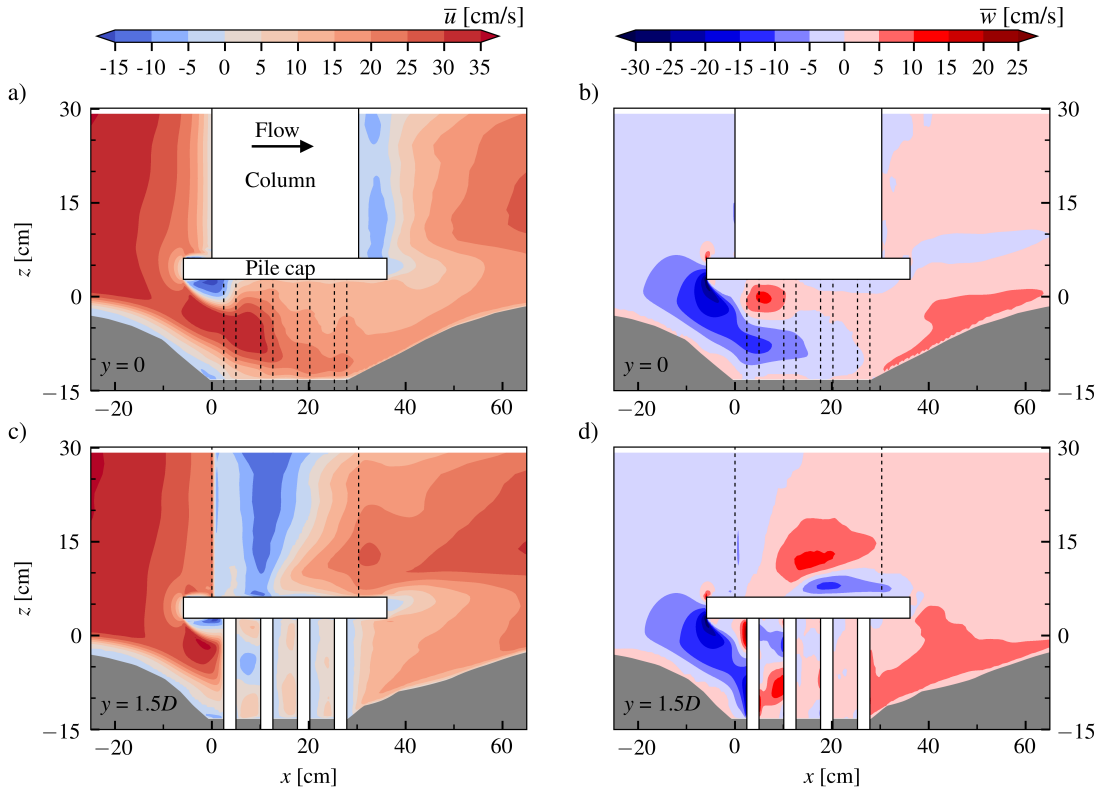

Figure 6.6: Contours of: a) and c) $\bar{u}$-velocity, and; b) and d) $\bar{w}$-velocity, respectively, at: a) and b): vertical plane $y = 0$, and; c) and d): vertical plane $y = 1.5D$, complex pier case I (present study).

Maps of $\bar{u}$-velocity in Figure 6.6 a) and c) indicate that the approach flow velocity decreases when approaching the pier and then the flow accelerates below the pile cap towards the piles. In

addition, the flow separates at the lower upstream edge of the pile cap, resulting in a reverse flow (a region with negative $\bar{u}$-velocity values) being formed below the pile cap. Contours of $\bar{w}$-velocity in Figure 6.6 b) and d) show that the approach flow is deflected in the vertical direction due to the pile cap, with a downward flow (down the pile cap) stronger than the upward flow (up the pile cap). Below the pile cap, at $y = 1.5D$, the incoming accelerated flow is deflected vertically in front of the upstream pile, creating an upward flow slightly stronger than the downward flow.

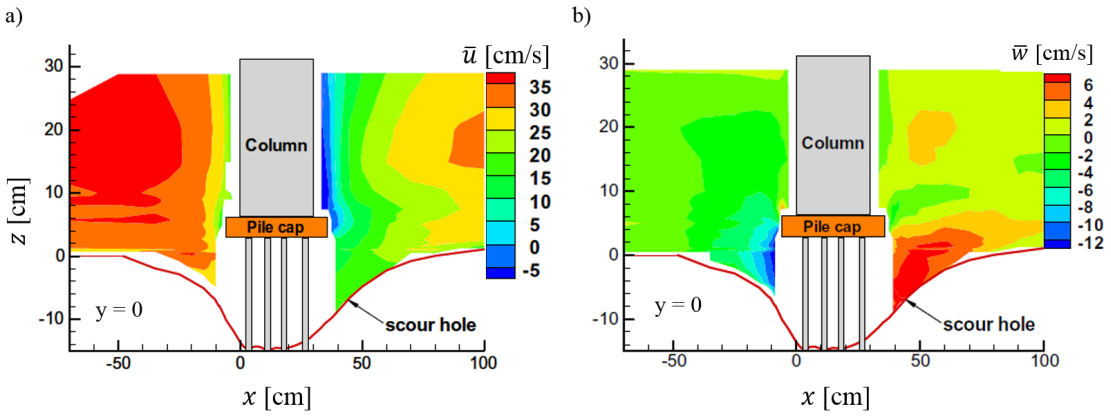

Figure 6.7: Contours of $\bar{u}$- and $\bar{w}$- velocities at the vertical plane $y = 0$, complex pier case I (Beheshti & Ataie-Ashtiani, 2016).

In front of the column, the approach flow is vertically directed towards the pile cap and then deflected against the approach flow direction, resulting in the formation of a small reverse flow region on the pile cap top level (Figure 6.8). Along the column side, a reverse flow region is detected above the pile cap due to the flow separation at the upstream side edges of the column, and its longitudinal length is increasing from the pile cap top level to the upper boundary surface (Figure 6.9).

Downstream of the pier, below the pile cap position, both $\bar{u}$- and $\bar{w}$- velocity components are positive which facilitates lift and transport of bed particles of the scour hole (see Figure 6.7 for comparison). The reverse flow region is visible behind the column with a nearly constant longitudinal extension over the column height (Figure 6.8) what is similar to the physical observations of Beheshti & Ataie-Ashtiani (2016) as shown in Figure 2.6. Furthermore, the outflow from the pile group zone interacts with the flow above the pile cap, thereby inducing two vortices: one near the bottom and other near the top downstream edges of the pile cap as shown in Figure 6.8 and

Figure 6.9. The peak values of $\bar{u}$-velocity at the wake of the pile cap was numerically predicted as about -4 cm/s what is fairly in agreement with the one experimentally obtained by Beheshti & Ataie-Ashtiani (2016) as presented in Figure 6.7 (-0.12U_∞ = -4.3 cm/s).

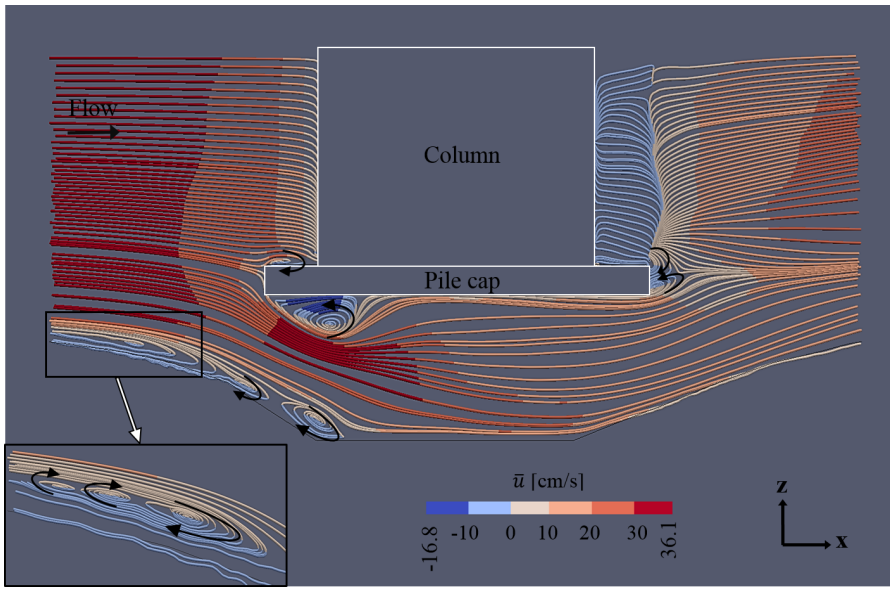

Figure 6.8: Time-averaged streamlines at the vertical plane $y = 0$, complex pier case I (present study).

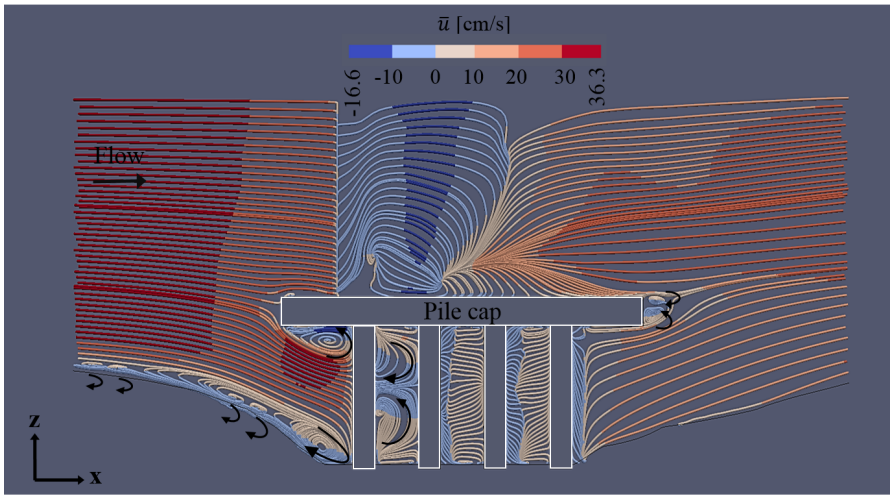

Figure 6.9: Time-averaged 2-D streamlines at the vertical plane $y = 1.5D$, complex pier case I (present study).

Inside the scour hole (upstream of the pile group) a big vortex together with several smaller vortices were numerically predicted close to the bed surface, which correspond to the horse-shoe vortex system. Those vortices are rotating in the same direction, as shown in Figure 6.8 and

Figure 6.9, which is different from what was observed for the single and compound pier cases in Chapter 5. That different behavior may possibly be explained by the fact that the incoming flow could pass underneath the main obstructing parts of the complex pier, resulting in a big/main horse-shoe vortex weaker than those for the single and compound pier cases. It is noteworthy to mention that the minimum $\bar{u}$-velocity value obtained (or maximum reverse flow velocity), which is corresponding to the big horse-shoe vortex, was about -0.25U_∞ for the complex pier case I while it was about -0.5U_∞ for the single and compound pier cases. Within the pile group, as shown in Figure 6.9, the flow structure behind the upstream pile is different from those predicted behind the following piles, which is due to the direct effect of the incoming accelerated flow on the upstream piles.

Concerning the flow structure in the transverse vertical plane, Figure 6.10 shows numerically obtained 2-D streamlines at mid-length of the complex pier ($x = 0.5L_{\text{col}}$). Due to the symmetry condition, the results are presented for only one side of the symmetry plane $y = 0$.

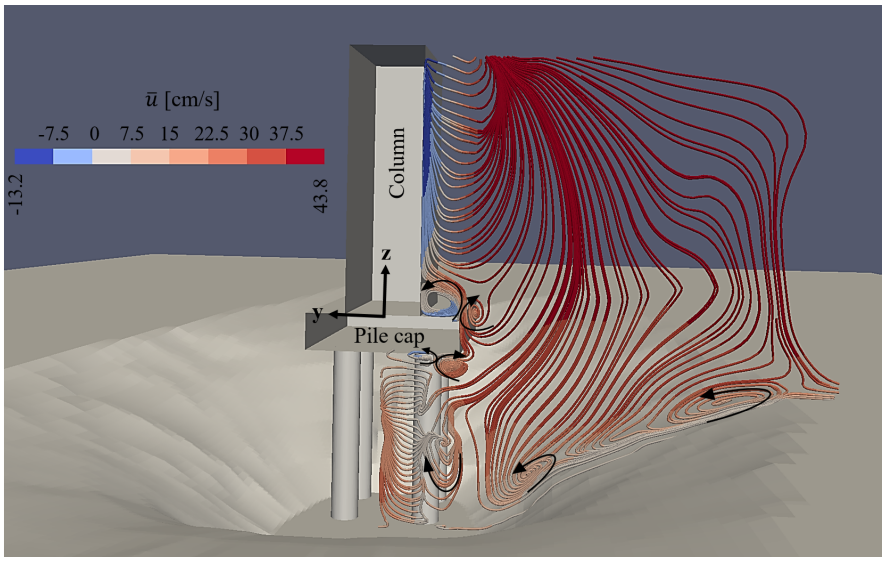

Figure 6.10: Time-averaged 2-D streamlines at the vertical transverse plane $x = 0.5L_{\text{col}}$, looking downstream, complex pier case I (present study).

The streamlines pattern, at $x = 0.5L_{\text{col}}$, indicates that two big vortices are formed at each side of the pile group close to the scour hole banks. Those vortices, which are a part of the horse-shoe vortex system, are rotating in the same direction. Moreover, $\bar{u}$-velocity values corresponding to those vortices are positive, meaning that they are moving downstream. In the piles' zone, no

vortex is observed in the transverse gap between the piles due to the flow contraction in that region. However, a big flow recirculation area was predicted in the zone below the pile cap and closer to the bottom bed, rotating in opposite direction of that for the horse-shoe vortices at this transverse plane. In addition, two vortices were predicted close to the bottom face of the pile cap in which one vortex points upstream zone (negative $\bar{u}$-velocity) and the other points downstream. Furthermore, a small roller that moves downstream is observed at the lateral side face of the pile cap and a vortex is detected on top of the pile cap at the junction of the pile cap and the column side (horizontal tube vortices in Figure 6.5). Overall, the streamlines presented in the above-referred vertical planes show that the flow structure around the pier elements is complex (much more than that for a single pier) as various vortices could be predicted with axes in all three directions.

Maps of the turbulence intensities are presented in Figure 6.11 for the vertical planes $y = 0$ and $y = 1.5D$ in terms of the mean-square u-, v- and w- velocity fluctuations ($\overline{u'u'}$, $\overline{v'v'}$ and $\overline{w'w'}$). In addition, the corresponding turbulent kinetic energy, computed as K = 0.5 ($\overline{u'u'}$+$\overline{v'v'}$+$\overline{w'w'}$), is also presented in Figure 6.11. For comparison, the experimental results of Beheshti & Ataie-Ashtiani (2016), at the vertical plane $y = 0$, are shown in Figure 6.12.

The turbulence intensities are not significant upstream of the complex pier. Below the pile cap, the turbulence intensities increase due to the flow-pier-bed interaction in that zone. Corresponding experimental results could not be obtained as shown in Figure 6.12 but the present numerical results indicate that, below the pile cap, the higher values of the turbulence intensities are generally positioned near the upstream piles (upstream part of the pier), decreasing when moving downstream. Moreover, the values of the turbulent kinetic energy near the scour hole bottom are larger than those for the approach flow region (where the corresponding friction velocity is close to the critical one (Beheshti & Ataie-Ashtiani, 2016)) what indicates the possibility of the bed erosion at the bottom of the scour hole after 72 h.

Downstream of the pier, the turbulence intensities decrease progressively with distance from the pier. At the symmetry plane $y = 0$, behind the column, the highest values of $\overline{u'u'}$ and $\overline{w'w'}$ are smaller than that for $\overline{v'v'}$ what is in agreement with the experimental results of Beheshti & Ataie-Ashtiani (2016) as shown in Figure 6.12. However, the predicted maximum values of $\overline{u'u'}$ and $\overline{v'v'}$ are, respectively, slightly under-estimated and over-estimated compared to the experimental

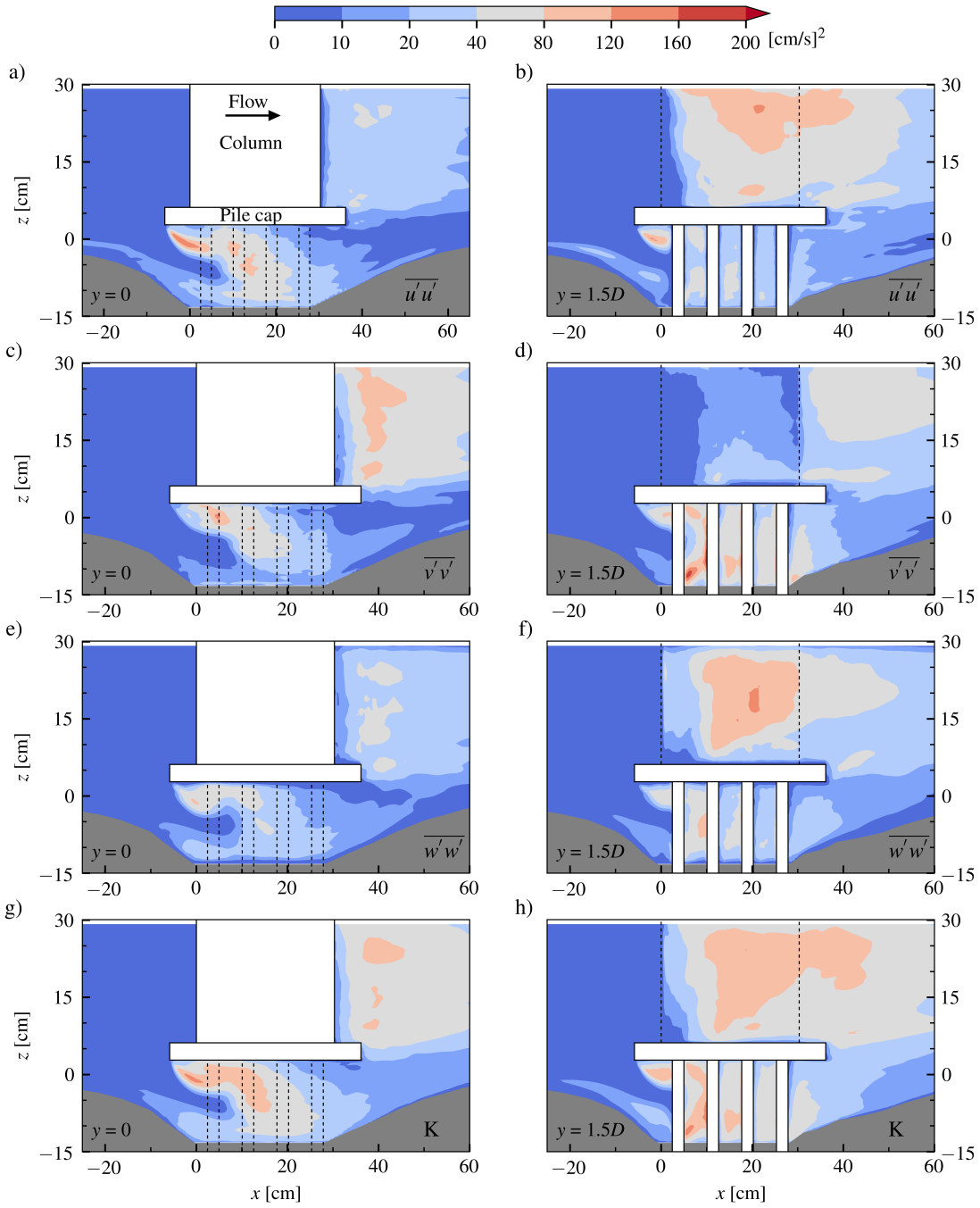

Figure 6.11: Contours of $\overline{u'u'}$, $\overline{v'v'}$, $\overline{w'w'}$ and K at vertical planes $y = 0$ (left) and $y = 1.5D$ (right), complex pier case I (present study).

results, whereas the highest values of $\overline{w'w'}$ and the turbulent kinetic energy were quite well predicted in this study. Concerning the vertical plane $y = 1.5D$, above the pile cap position, $\overline{u'u'}$ and $\overline{w'w'}$ turbulence intensities are dominant along the column side and thereby the turbulent kinetic

energy is quite high in that zone. The referred strong fluctuations mostly occurred downstream of the vertical vortex formed along the full column side (see Figure 6.9 for the location of the vertical vortex).

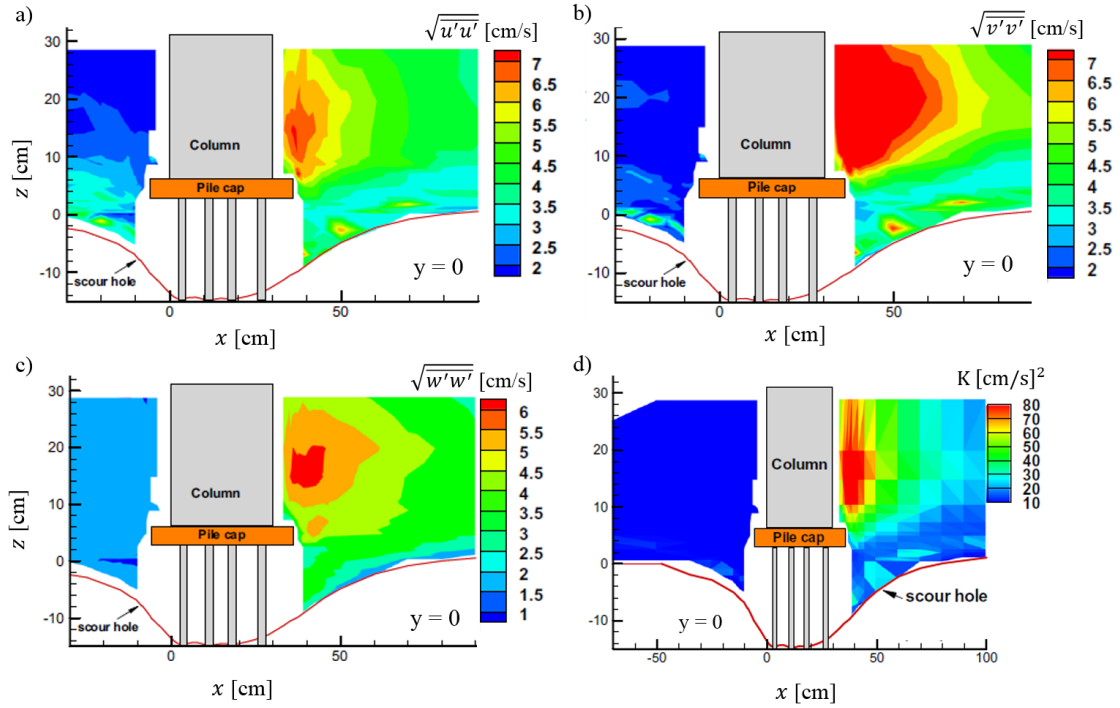

Figure 6.12: Contours of $\sqrt{\overline{u'u'}}$, $\sqrt{\overline{v'v'}}$, $\sqrt{\overline{w'w'}}$ and K at the vertical plane y = 0, complex pier case I (Beheshti & Ataie-Ashtiani, 2016).

Overall, most of the peak values were predicted in the zones where no experimental measurements could be performed due to measuring instrument's limitations what demonstrates the potential advantage of using the present numerical model to investigate the flow field around the complex pier elements.

6.2.2.2 Flow features in horizontal planes

Contour plots of the time-averaged u- and v- velocity components at different horizontal planes are presented in Figure 6.13. The chosen horizontal planes were situated below (z = -13, -6.5 and 1.05 cm), by the middle (z = 5 cm) and above (z = 8.97 cm) the pile cap position. The horizontal planes at negative z-levels relate to the flow field inside the scour hole. The corresponding experimental results of Beheshti & Ataie-Ashtiani (2016), available for z = 1.05, 5 and 8.97 cm, are shown in

Figure 6.14. Moreover, numerically obtained time-averaged streamlines (using the longitudinal and transverse velocity components) and also $\bar{w}$-velocity contour map at z = 5 and 8.97 cm are presented in Figure 6.15.

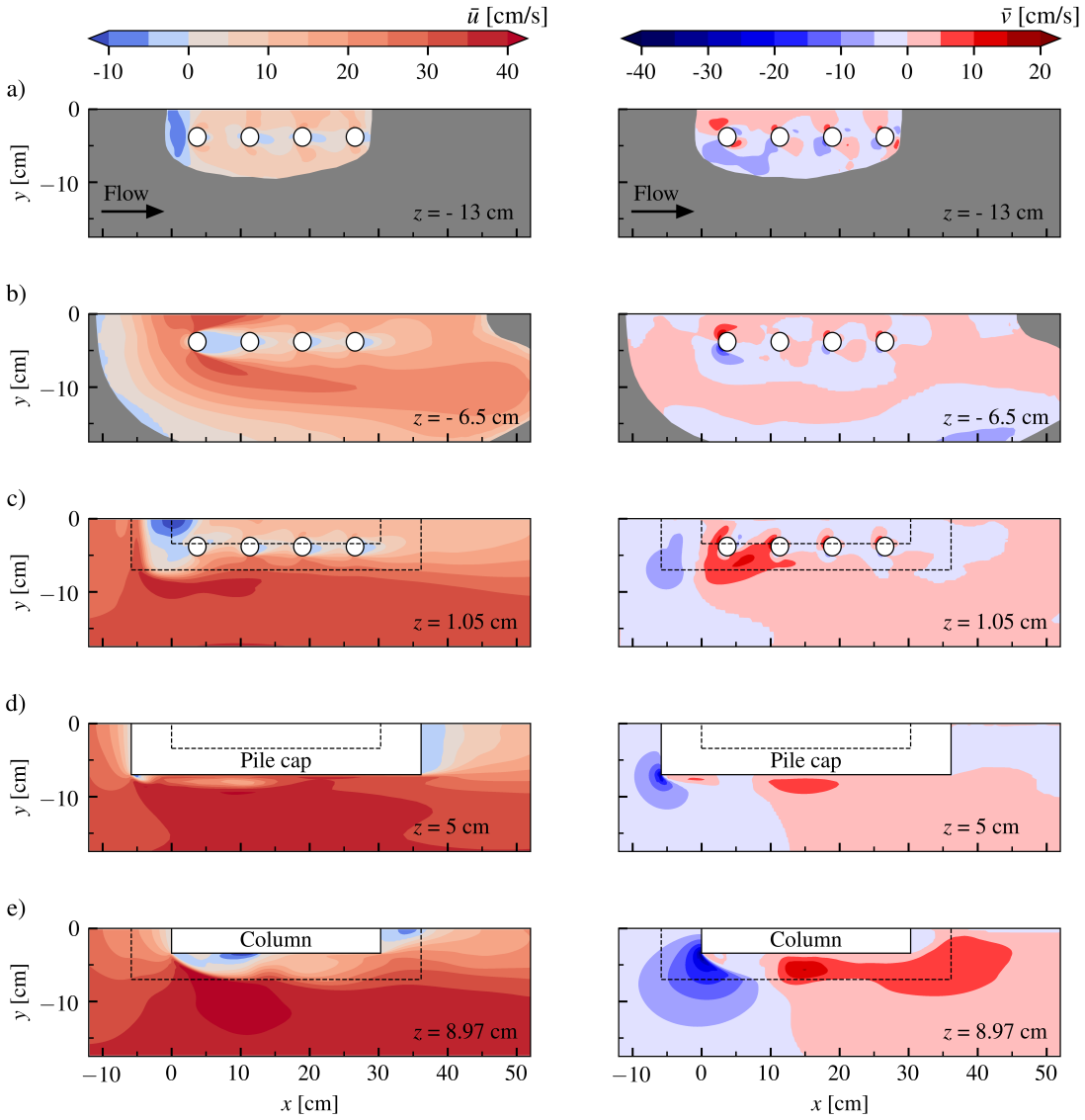

Figure 6.13: Contours of $\bar{u}$- (left) and $\bar{v}$- (right) velocities at horizontal planes: a) z = -13 cm, b) z = -6.5 cm, c) z = 1.05 cm, d) z = 5 cm and e) z = 8.97 cm, complex pier case I (present study).

A comparison between $\bar{u}$-velocity maps in Figure 6.13 (left) indicates that the maximum $\bar{u}$-velocity value increases from the lower z-level to the upper z-level considered for the present results presentation. Moreover, the corresponding maximum values were predicted at the pier sides for the planes above the channel bed level.

For the planes including the scour hole, z = -6.5 and -13 cm, negative $\bar{u}$-velocity values are observed at the upstream part of the scour hole, referring to the horse-shoe vortex system. At the plane z = -6.5 cm, the maximum $\bar{u}$-velocity value was predicted close to the upstream piles' position but at z = -13 cm, at a level near the piles' base or the scour hole bottom, the maximum value was obtained close to the third and fourth row of the piles (although with values only higher than that for the upstream ones) due to the formation of the horse-shoe vortex in front of the upstream piles.

At the plane z = 1.05 cm, a reverse flow region with a minimum negative value of about -0.34U_∞ was predicted after the lower upstream edge of the pile cap. At this plane, the maximum $\bar{u}$-velocity was numerically predicted to be about 1.05U_∞ along the pier sides, which is in good agreement with physical measurements of Beheshti & Ataie-Ashtiani (2016) (about 1.02U_∞). Moreover, at this plane, no reverse flow was predicted downstream of the pier, similar to that reported in the referenced experimental study as shown in Figure 6.14 a).

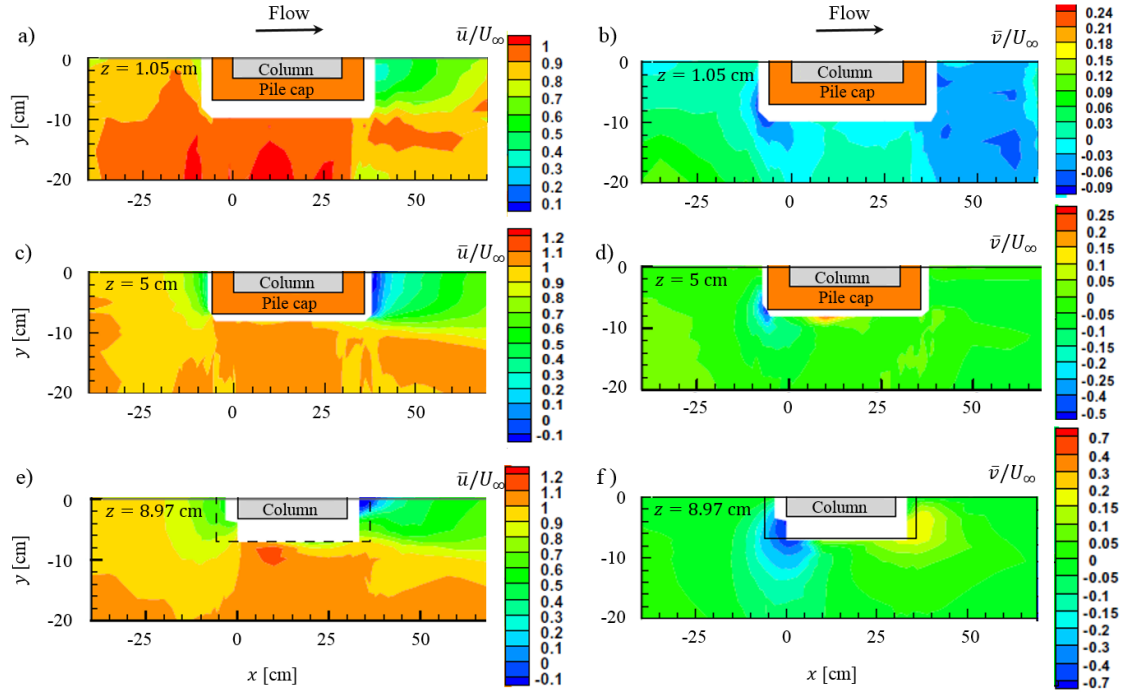

Figure 6.14: Contours of $\bar{u}$- and $\bar{v}$- velocities at the horizontal plane z = 1.05, 5 and 8.97 cm, complex pier case I (Beheshti & Ataie-Ashtiani, 2016).

At the plane z = 5 cm, the approach flow velocity decreases when approaching the pile cap. The flow is then deflected and accelerated sideways, resulting in a very small vortex being formed

immediately after the upstream side edges of the pile cap as illustrated in Figure 6.15 a). After that vortex, the corresponding $\bar{w}$-velocity map shows a recirculation in the vertical transverse plane (sudden change in sign of $\bar{w}$-velocity values) and since the corresponding $\bar{u}$-velocities are positive along the pile cap side, the recirculation moves downstream (Figure 6.10 shows clearly the vortex on the pile cap side face). At this plane, the maximum $\bar{u}$-velocity value was numerically obtained to be equal to $1.105U_\infty$, which is close to the experimental result (about $1.1U_\infty$ as shown in Figure 6.14 c)). Downstream of the pier, the flow separates at the downstream side edges of the pile cap and forms a reverse flow zone behind the pile cap. The corresponding minimum $\bar{u}$-velocity value was predicted to be about $-0.11U_\infty$, which is in agreement with the physical measurement of Beheshti & Ataie-Ashtiani (2016). Concerning the size of the reverse flow zone at the plane $z = 5$ cm, as shown in Figure 6.15 a), its longitudinal extension increases from the side edges of the pile cap until $y = 0$ what is also in agreement with the experimental reference data presented in Figure 2.5 b).

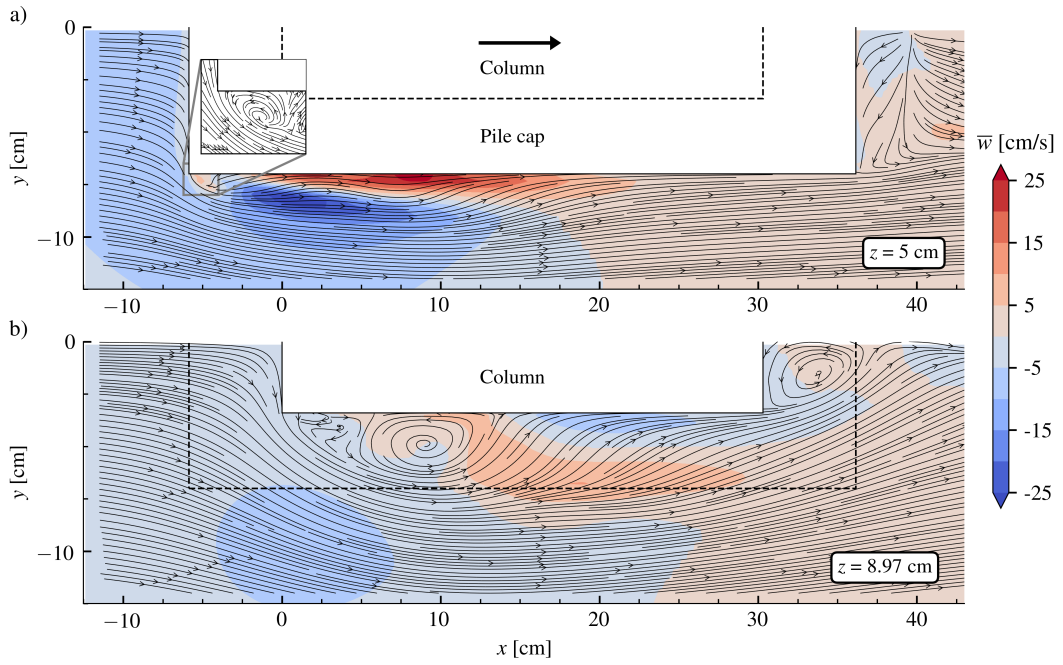

Figure 6.15: Time-averaged 2-D streamlines (obtained using $\bar{u}$- and $\bar{v}$- velocities) together with $\bar{w}$-velocity contour map around the pile cap and column at: a) $z = 5$ cm (pile cap) and b) $z = 8.97$ cm (column), complex pier case I (present study).

At the plane $z = 8.97$ cm, changes of $\bar{u}$-velocity upstream and downstream of the column follows a pattern similar to the one obtained for the corresponding zones at $z = 5$ cm. The 2-D

streamlines in this plane, as shown in Figure 6.15 b), indicates a recirculation pattern behind the column that is similar to that obtained for the infinite cylinder cases in Chapter 4 (Figure 4.7). The corresponding recirculation length, measured from the rear face of the column to the reattachment point on the symmetry line, was numerically obtained as about the column width and that is in reasonable agreement with the experimental measurements of Beheshti & Ataie-Ashtiani (2016) as shown in Figure 2.5 c). In addition, Figure 6.15 b) shows that the flow separates at the upstream side edges of the column and reattaches by its mid-length. In the corresponding separation zone, two vortices with opposite circulation directions are formed on each side of the column. Finally, at this plane, the maximum $\bar{u}$-velocity value was obtained to be about $1.23U_\infty$ and the corresponding value measured experimentally by Beheshti & Ataie-Ashtiani (2016) is about $1.2U_\infty$ as shown in Figure 6.14 e).

Concerning the $\bar{v}$-velocity maps, Figure 6.13 (right), the presence of the pier elements deflects the flow sideways. This deflection is stronger at the upper level (z = 8.97 cm), occurring close to the upstream side edges of the column. Downstream of the pier, overall, the flow converges back to the symmetry line ($y = 0$). The peak $\bar{v}$-velocity values were numerically predicted at points close to the pier elements where experimental results are not available as shown in Figure 6.14 (right). According to the present numerical results, the maximum absolute $\bar{v}$-velocity value at z = -6.5 cm (near the mid-height of the pile) is bigger than the values at the close upper (z = 1.05 cm) and lower (z = -13 cm) levels. Moreover, the numerically obtained pattern of $\bar{v}$-velocity contours at the elevation near the mid-height of the pile cap (z = 5 cm) is nearly similar to that for the plane above the pile cap (z = 8.97 cm), which is in agreement with the experimental observations of Beheshti & Ataie-Ashtiani (2016).

The horizontal distributions of the mean turbulent kinetic energy (K) over the height of the flow are presented in Figure 6.16. For the horizontal planes below the pile cap, the values of K close to the piles are smaller near the bottom bed, at z = -13 cm, than those for the upper levels (at z = -6.5 and 1.05 cm). At the plane z = -6.5 cm, Figure 6.16 b), K is notably high near the second pile and decreases moving downstream. In fact, as shown in Figure 6.11 h), the kinetic energy is generally higher all over the depth between the first and second alignment of piles, the specific location of the corresponding maximum value is changing over the pile's height. Concerning the

plane z = 1.05 cm, near the bottom face of the pile cap, a core with high values of the kinetic energy is observed around the upstream/first pile (Figure 6.16 c)) due to the strong reverse flow that exists immediately after the low upstream edge of the pile cap. Moving downstream, the values of K predicted on the outer side of the piles are larger than those on the inner side of the piles. At the plane z = 5 cm, Figure 6.16 d), the high level of K was predicted in the shear layer close to the side edges of the pile cap, while the corresponding high values at z = 8.97 cm (Figure 6.16 e)) were obtained along the column side and also in the zone behind the column. Overall, Figure 6.16 shows the locations with the highest values of the kinetic energy what indicates where the strongest flow fluctuations occur, in accordance with the turbulent kinetic energy definition.

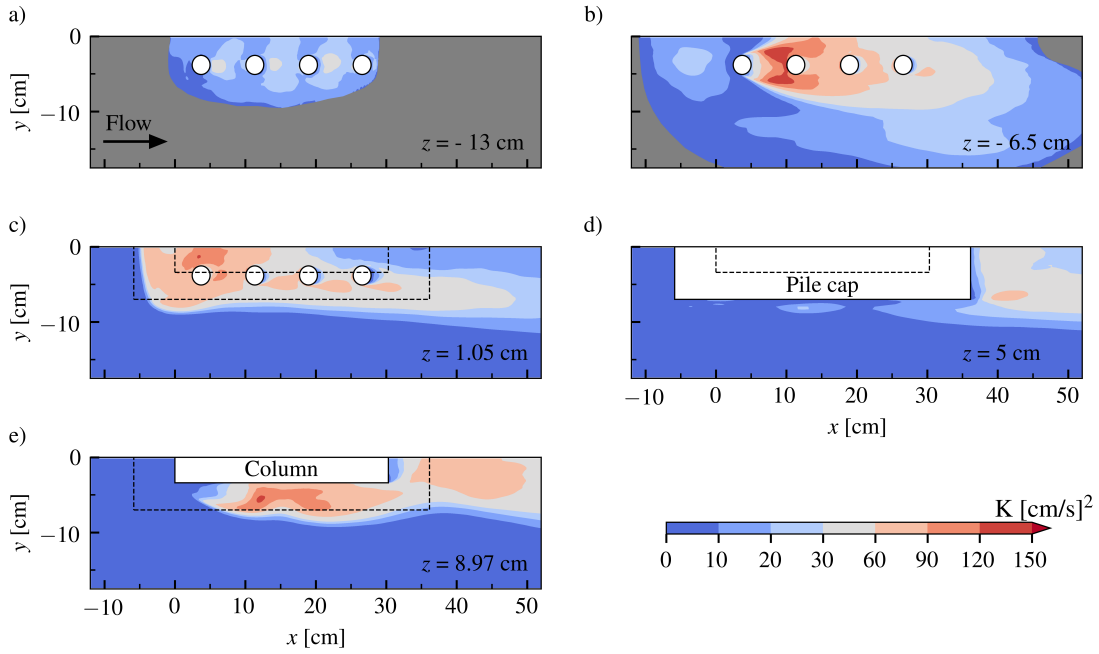

Figure 6.16: Contours of mean turbulent kinetic energy (K) at horizontal planes: a) z = -13 cm, b) z = -6.5 cm, c) z = 1.05 cm, d) z = 5 cm, e) z = 8.97 cm, complex pier case I (present study).

6.3 Complex pier case II: column and pile cap with round corners

6.3.1 Details of the test case and numerical model setup

Several numerical simulations were performed to investigate the flow characteristics (namely the flow vortices) around a specific complex bridge pier, referenced as case II in the Introduction

chapter, over the time development of the scouring process. The complex pier case II consists of a column with a pile cap supported by a 1×4 pile group for a situation when half of the pile cap height ($0.5h_{cap}$=2.9 cm) was positioned above the initial channel bed level ($z = 0$). The geometric characteristics of the complex pier case II are presented in Figure 6.17 a). Moreover, the geometry of the scour hole developed after two intermediate stages (t = 1 hour and 12 hours) and at the equilibrium stage (t = 11 days), taken from the experimental data of Ramos et al. (2016), is shown in Figure 6.17 b), c) and d).

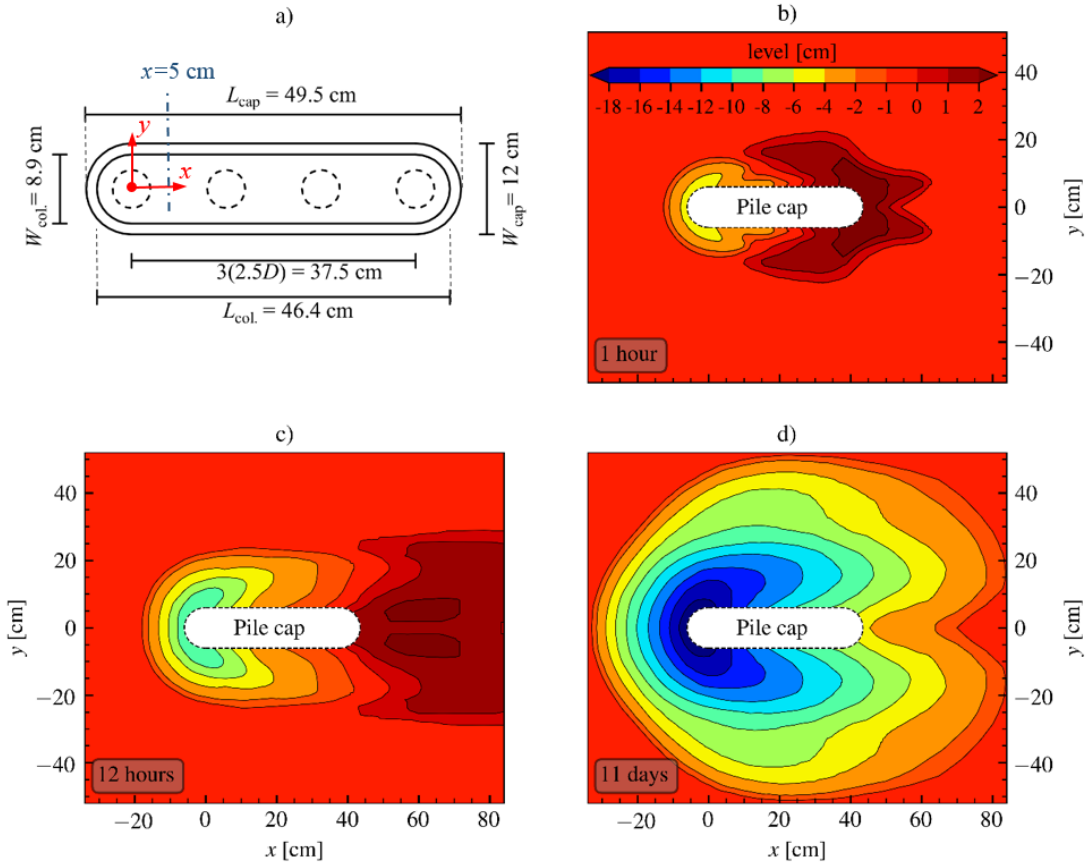

Figure 6.17: Geometric characteristics of the complex pier case II and the corresponding bed geometries developed after t = 1 hour, 12 hours and 11 days (taken from the experimental data of Ramos et al. (2016)).

Ramos et al. (2016) obtained the bed elevations around the complex pier case II by analyzing a number of photos taken from a horizontal platform above the water surface level. The corresponding experimental measurements did not cover the region below the pile cap since the camera could not capture any photo of it. For the present numerical study, the bed model in that region was generated using descriptions of Ramos obtained after a private communication. Moreover,

although a deposition dune would be expected to exist far downstream from the pier at t = 11 days, the corresponding bed levels were not reported by Ramos et al. (2016) and so the dune was neglected for the present numerical study.

In order to study the temporal evolution of the flow around the complex pier case II, numerical calculations were performed at the different stages of the local scouring process (t = 0, 1 hour, 12 hours and 11 days, in which t = 0 corresponds to the initial flat-bed condition) for the same flow conditions of the experiment conducted by Ramos et al. (2016). The approach flow depth h was equal to 0.18 m, the mean approach flow velocity U_∞ was 0.327 m/s ($\mathrm{Re}_h \sim 5.9 \times 10^4$ and Fr = 0.25) and the bed material was a uniform sand with mean diameter d_{50} = 0.86 mm.

The computational domain dimensions are $27.5W_{\mathrm{cap}} \times 15W_{\mathrm{cap}} \times (h + h')$ in longitudinal, transverse and vertical directions, respectively. Since h' denotes the bed model height, for the numerical test corresponding to t = 0, h' was considered as about one cell height (to model the bed roughness). That vertical length h' was increased for the other numerical tests regarding the corresponding maximum scour depth. The pier was positioned $7.5W_{\mathrm{cap}}$ downstream from the inlet section, in the symmetry plane of the domain, and the corresponding inflow conditions were obtained from a periodic open-channel flow at identical Re_h. The pier's surface is smooth but the bed surface was modeled as a rough surface with $k_s = 2.5d_{50}$. The free-slip condition was imposed on the water surface and finally, at the outlet section, zero pressure with convective boundary condition for the velocity components was used.

In all numerical tests, the time-step size was about 0.0015 s and the flow statistics were collected over 60 s (about 40000 time-steps) after removing the initial condition effects from the calculations. During the numerical simulations, the corresponding bed geometries in the flow domain were considered as a fixed boundary.

The computational mesh is approximately: 5.5 million cells (389×241×59) for the numerical test corresponding to t = 0, 5.9 million cells (408×249×58) for t = 1 hour, 7 million cells (408×249×69) for t = 12 hours and 11.6 million cells (501×249×93) for t = 11 days. Overall, the mesh is finer in the region close to the pier elements and bed surface and progressively coarser with the distance. The spatial increase of the grid cell size was performed with an expansion ratio of about 1.03, having in mind that the grid should not be too coarse where vortices are expected

to be formed. The grids in two representative sections (horizontal and vertical sections) are shown in Appendix C (Figure C.2 to Figure C.5) for all numerical tests related to the complex pier case II. The corresponding turbulence resolutions are graphically presented in Figure 6.18. In most of the grid cells, the unresolved part of the turbulent kinetic energy is less than 0.2. The cells that have values bigger than 0.2 are mostly near the inlet, outlet and top domain boundaries where the mesh is relatively coarse. It should be noted that in some near wall-cells, the turbulence resolution was also observed to be bigger than 0.2 what is due to the use of the wall model in the simulations (not fully-resolved LES). Overall, at least 84% of the active cells met the Pope's criterion (Pope, 2004), which is interpreted as the turbulence was well resolved at most of the grid cells.

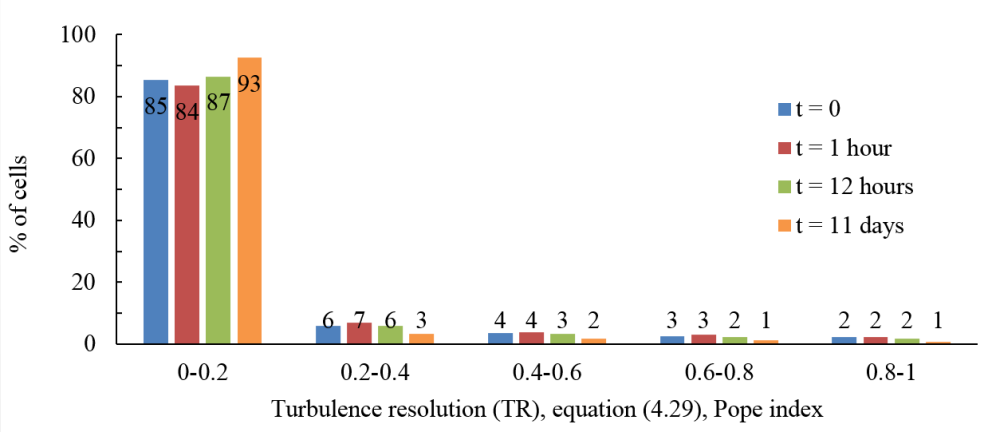

Figure 6.18: Percentage of the unresolved turbulent kinetic energy (TR) for all simulations corresponding to the complex pier case II, present study.

6.3.2 Results and discussion

6.3.2.1 Flow features in vertical planes

A sequence of the time-averaged streamlines topology upstream of the pier (at the vertical symmetry plane $y = 0$) is shown in Figure 6.19 for the bed geometries corresponding to $t = 0$, 1 hour and 12 hours. Concerning the equilibrium stage of the scour hole development process ($t = 11$ days), the streamlines pattern at the vertical plane $y = 0$ is shown in Figure 6.20. Furthermore, in order to clearly show details of the flow field in front of the pier's base, the corresponding contour maps of the time-averaged u- and w- velocity components are presented in Figure 6.21.

At the vertical plane $y = 0$, the approaching flow is deflected up and down in front of the column. The corresponding deflection point is observed at about $z = 14$ cm for the equilibrium stage (see Figure 6.20), while for the intermediate stages of the scour hole development process, that vertical flow deflection was predicted to occur at about $z = 15$ cm (not pictured in Figure 6.19). The downward flow in front of the column is deflected by the pile cap, resulting in a small vortex being formed on the top face of the pile cap at $y = 0$. The so-called bow wave (surface roller) was not numerically predicted in the present study as the top domain boundary was treated as a free-slip rigid lid. Overall, the present numerical results confirm the interpretations of Moreno (2016) about the flow structure in front of the column as shown in Figure 2.8.

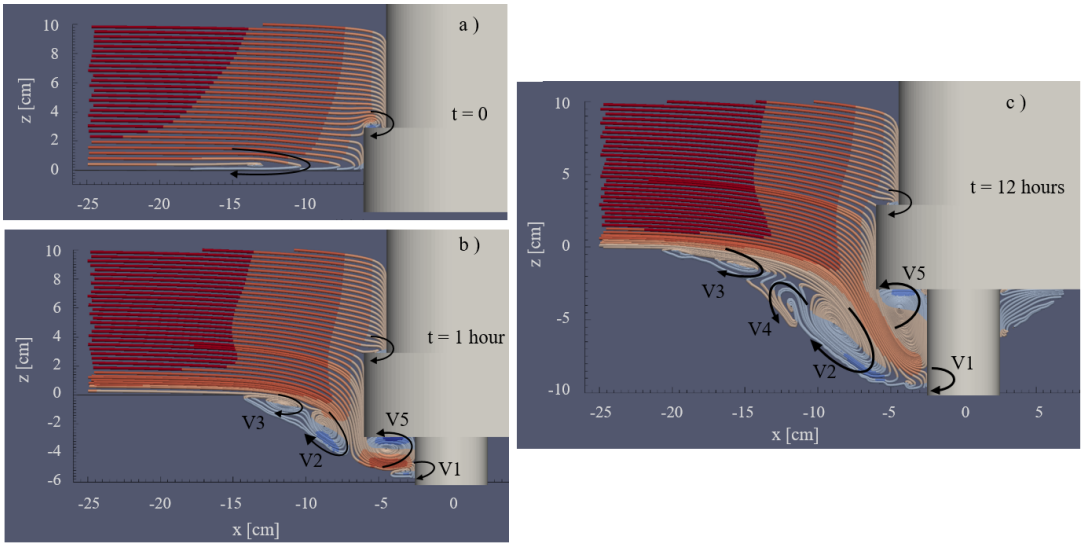

Figure 6.19: Time-averaged streamlines upstream of the pier at the vertical symmetry plane $y = 0$ for the bed geometries corresponding to: a) $t = 0$; b) $t = 1$ hour; and c) $t = 12$ hours, complex pier case II (it is to be noted that the mean approach water depth is 18 cm).

Concerning the pile cap, Moreno (2016) interpreted that the flow is deflected up and down in front of the pile cap, but the present numerical study indicates that the flow turns downward in that zone for the scoured bed cases as shown in Figure 6.21 b). At $t = 0$ (the flat-bed case) the maximum downward flow in front of the pile cap was numerically predicted near the channel bed level as about -0.16U_∞, a value that is smaller than that reported by Raudkivi (1986) for a single circular pier (about -0.4U_∞). The difference is due to the influence of the pile cap step (out of the column face), which prevents the downward velocity to have a greater increase. During the development of the scour hole, the maximum value of the downward flow significantly increases

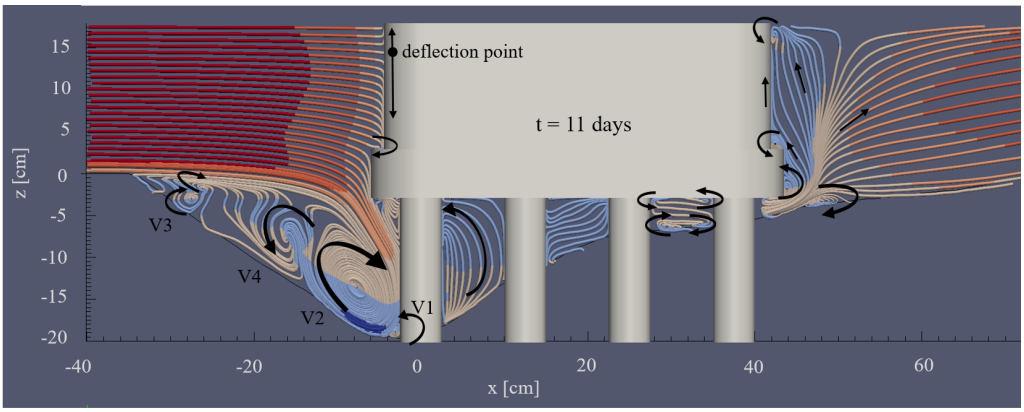

Figure 6.20: Time-averaged streamlines at the vertical symmetry plane $y = 0$ for the equilibrium stage of the scour hole development process, complex pier case II.

and moves closer to the lower upstream edge of the pile cap (below the initial channel bed level).

At $t = 0$, only one stretched vortex was numerically predicted upstream of the pier near the bed surface, while more complicated flow structures are observed in that zone with the development of the scour hole (see Figure 6.19 and Figure 6.20). In fact, at the flat-bed condition ($t = 0$), the vertical size of the horse-shoe vortex is so small. Then, the corresponding numerical prediction requires a more clustered grid in the zone near the bed to fully resolve the small flow vortices (dimensionless size of the grid cell height in that zone is about 30, based on the friction velocity estimated at the inlet section). For the other test cases, several vortices could be predicted upstream of the pier inside the scour hole, in accordance with the fact that the size of vortices increases with the scour depth.

According to the present numerical results, the flow is accelerated below the lower upstream edge of the pile cap and then vertically deflected by the first/upstream pile, resulting in an upward flow stronger than the downward flow at $t = 1$ hour and 12 hours (Figure 6.21). That is because, at those intermediate stages of the scour hole development process, the deflection point at the upstream face of the first pile occurs near the scoured bed surface. The vertically deflected flow is then diverted backwards by the pile cap and the bed, resulting in two vortices being formed below the bottom face of the pile cap (V5) and near the pile-bed junction (V1) as shown in Figure 6.19 b) and c). At the equilibrium stage of the scour hole process, $t = 11$ days, the accelerated flow below the pile cap is deflected by the mid-height of the first pile, resulting in a downward flow in front of the pile much stronger than the upward flow. The corresponding junction vortex

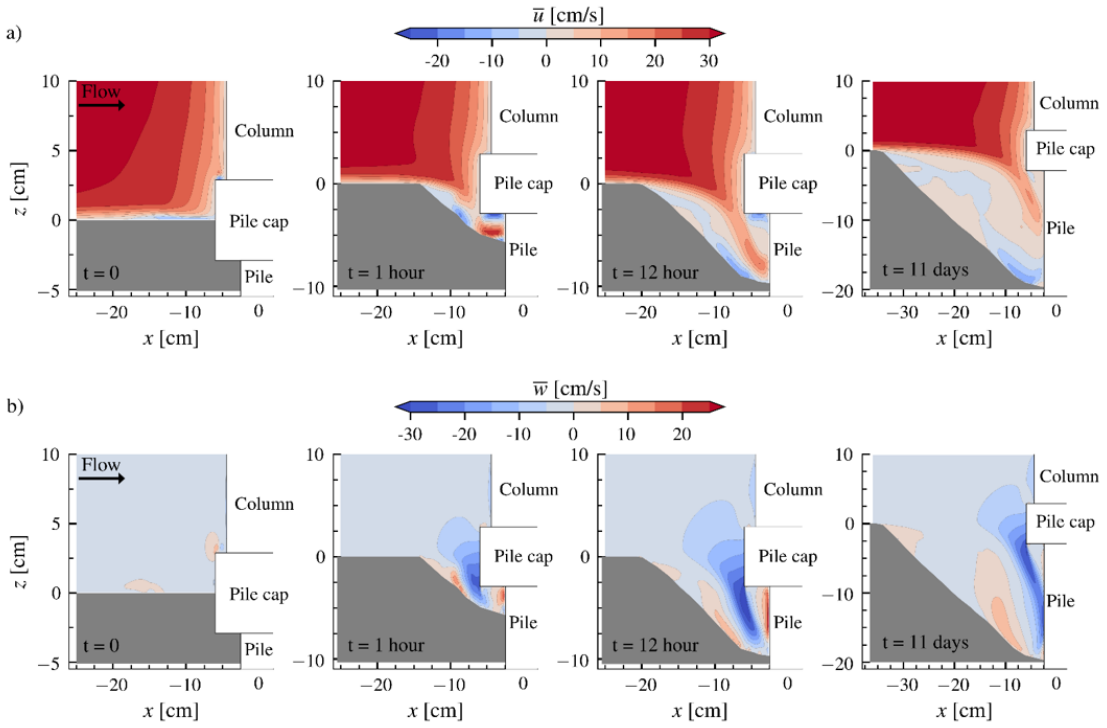

Figure 6.21: Contours of a) $\bar{u}$-velocity and b) $\bar{w}$-velocity upstream of the pier at the vertical plane $y = 0$ for the bed geometries corresponding to $t = 0$, 1 hour, 12 hours and 11 days, complex pier case II.

V1 is rotating counter-clockwise, as shown in Figure 6.20, which is the opposite direction of the corresponding ones formed at the intermediate stages of the scour hole (Figure 6.19). The main horse-shoe vortex was denoted by V2 in Figure 6.19 and Figure 6.20. At t = 1 hour, vortex V2 was completely formed upstream of the pile cap zone (upstream of V5), due to the small distance between the pile cap and the scoured bed surface, but its position moved towards the upstream pile with the time development of the scour hole process. The main vortex V2 is rotating clockwise for all the scoured bed configuration stages, similar to that reported for the single and compound pier cases, respectively, in Figure 5.11 and Figure 5.16. In addition to the vortices mentioned above, at the intermediate stages of the scour development process, the approach flow separates at the upstream edge of the scour hole and a clockwise vortex V3 is formed immediately after that edge. For the equilibrium stage, the flow structure in that zone is a bit more complex as two (small) vortices V3 (instead of one) with the same reported rotation direction are observed. At t = 1 hour, the vortex V3 is positioned directly upstream of V2 inside the scour hole but with the development of the scour hole, the vortices V2 and V3 distance from each other and that gives space to a vortex

V4 being formed between those vortices. According to the present results, the vortex V4 is closer to the main vortex V2 but in the opposite direction of V2.

Figure 6.20 also shows the flow structure behind the piles at the vertical symmetry plane y = 0. According to Ramos et al. (2016), scouring begins near the upstream face of the pile cap and after about t = 8 days, the scour hole completely uncovers the pile cap bottom. At t = 11 days, considered for this study, different flow structures were numerically predicted behind the piles due to the changes in the flow intensity and the bed geometry when moving downstream from the upstream pile.

Concerning the flow zone downstream of the pier, Figure 6.22 shows the time-averaged streamlines downstream of the pier at the vertical symmetry plane y = 0 for the bed geometries corresponding to t = 0, 1 hour and 12 hours (see Figure 6.20, for the corresponding zone at the equilibrium stage of the scour hole process).

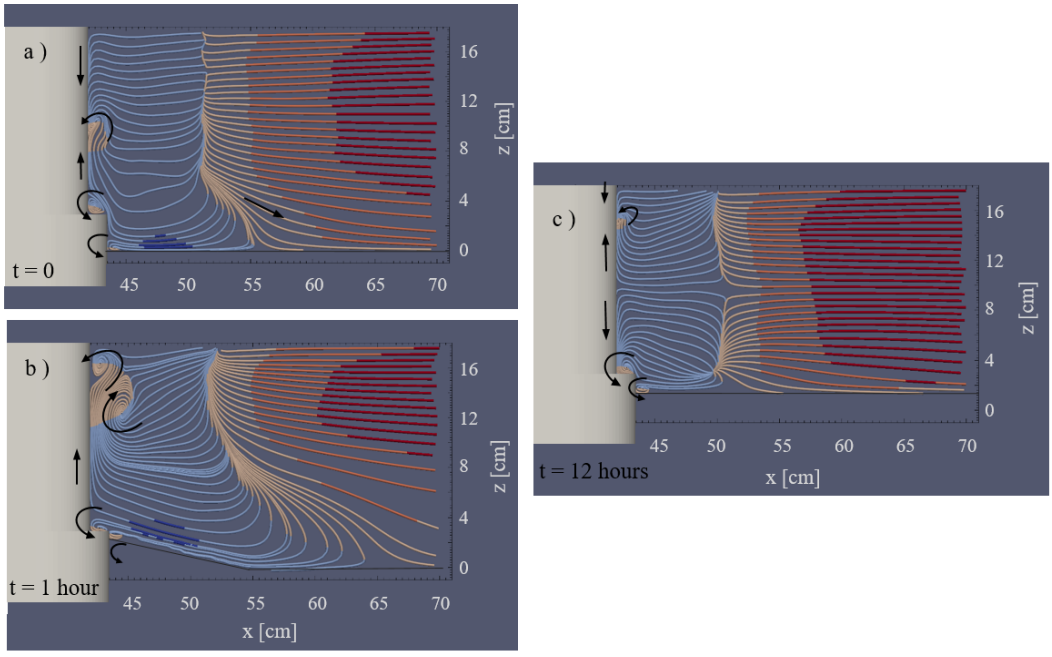

Figure 6.22: Time-averaged streamlines downstream of the pier at the vertical symmetry plane y = 0 for the bed geometries corresponding to: a) t = 0; b) t = 1 hour; and c) t = 12 hours, complex pier case II.

The reverse flow region (blue streamlines) was predicted behind the column and pile cap. At the flat-bed condition (t = 0) and the intermediate stages of the scour hole process (t = 1 hour and 12 hours), the reverse flow near the bed interacts with the pile cap and column, resulting in two vortices being formed: one on the top face of the pile cap and the other immediately behind the

pile cap (Figure 6.22). Above the pile cap position, behind the column, different flow structures were predicted at different stages of the scour process. Moving downstream, there is a downward flow towards the bed that facilitates sediment deposition at $t = 0$, as well as at $t = 1$ hour and 12 hours. At the equilibrium stage ($t = 11$ days), the referred downward flow is replaced by an upward flow induced from the region underneath the pile cap (Figure 6.20). The outflow from that region separates at the lower downstream edge of the pile cap and a counter-clockwise rotating vortex is formed near the bottom edge of the pile cap. Just downstream of that, in the eroded bed region, a clockwise rotational flow near the bed surface was predicted. The upward flow behind the pier, at $t = 11$ days, interacts with the rear face of the column and two counter-clockwise rotating vortices are formed: one close to the bottom rear edge of the column and the other near the water surface. Overall, the present numerical results, shown in Figure 6.20 and Figure 6.22, indicate that the flow structure is complex downstream of the pier and largely changes with the development of the scour hole.

Figure 6.23 and Figure 6.24 represent the time evolution of the streamlines (obtained from $\bar{v}$- and $\bar{w}$- velocity components) at transverse cross-section $x = 5$ cm, positioned in the gap between the first and second piles as shown in Figure 6.17 a). In fact, the transverse plane $x = 5$ cm represents most of the vortices which exist on the pier side. It is to be noted that notations of the vortices at $x = 5$ cm are different from those in the longitudinal vertical plane $y = 0$.

The corresponding streamline patterns indicate that, although $\bar{v}$- and $\bar{w}$- velocity values are generally smaller than the corresponding $\bar{u}$-velocity values in magnitude, the flow is deflected sideways at $x = 5$ cm (upstream part of the pier) for $t = 0$, 1 hour and 12 hours. But for the equilibrium scour hole ($t = 11$ days), a downward flow towards the scour hole is observed on the pier sides what is similar to the physical observations of Beheshti & Ataie-Ashtiani (2016) for the complex pier case I at the equilibrium stage.

Overall, the numerical simulations predicted several vortices near the column, pile cap and bottom bed surface at $x = 5$ cm. The number, size and position of the vortices change with the scour depth. According to the present numerical results, it is evident that the size of vortices near the bed increases with the scour depth. Details of the number of vortices and the corresponding positions are as follows:

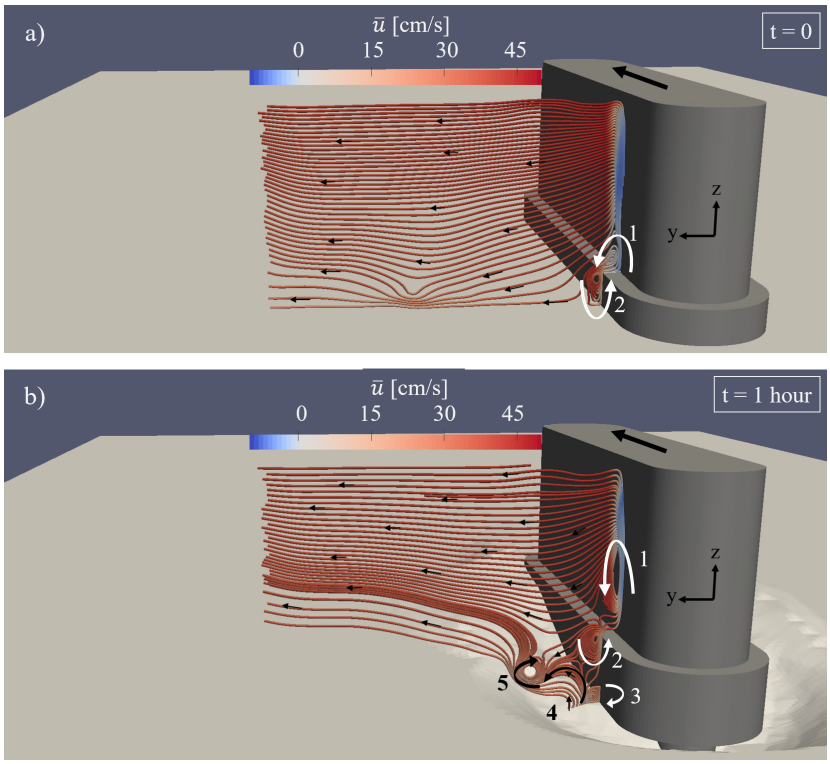

Figure 6.23: Time-averaged streamlines obtained from $\bar{v}$- and $\bar{w}$- velocity components at transverse cross-section x = 5 cm for: a) t = 0; and b) t = 1 hour, looking downstream (complex pier case II).

Above the channel bed level, two vortices (1 and 2, rotating in the same direction) were predicted near the top side edge of the pile cap for all cases. During the time development of the scour hole, a vortex (3) was formed close to the bottom side edge of the pile cap, but it disappeared at the equilibrium stage. In fact, with increasing the scour depth, vortex 4 (near the bed) and vortex 2 distance from each other, resulting in that vortex 2 becomes bigger and covers the most part of the pile cap side face at t = 11 days (Figure 6.24 b)). At the intermediate stages of the scour hole process, the so-called vortex 4 facilitates lift of the sediment particles from the bed surface and transport particles downstream together with vortices 5 and 6 as the corresponding $\bar{u}$-velocity values are positive. However, at the equilibrium stage, a backward flow (negative $\bar{u}$-velocity) was predicted inside the scour hole at x = 5 cm. Concerning vortex 6, it was created by enlarging the scour hole as shown in Figure 6.23 and Figure 6.24. It has to be noted that at t = 12 hours, the scour hole has uncovered below the pile cap at x = 5 cm. Although, the corresponding streamlines are apparent from Figure 6.24 a), an arrow was placed in this figure to show the corresponding vortex (7) which was predicted in that zone. At the equilibrium stage of the scour hole process,

vortex 7 was replaced by vortex 4. In fact, by enlarging the scour hole, vortex 4 becomes bigger and eventually covers the region below the pile cap at $x = 5$ cm.

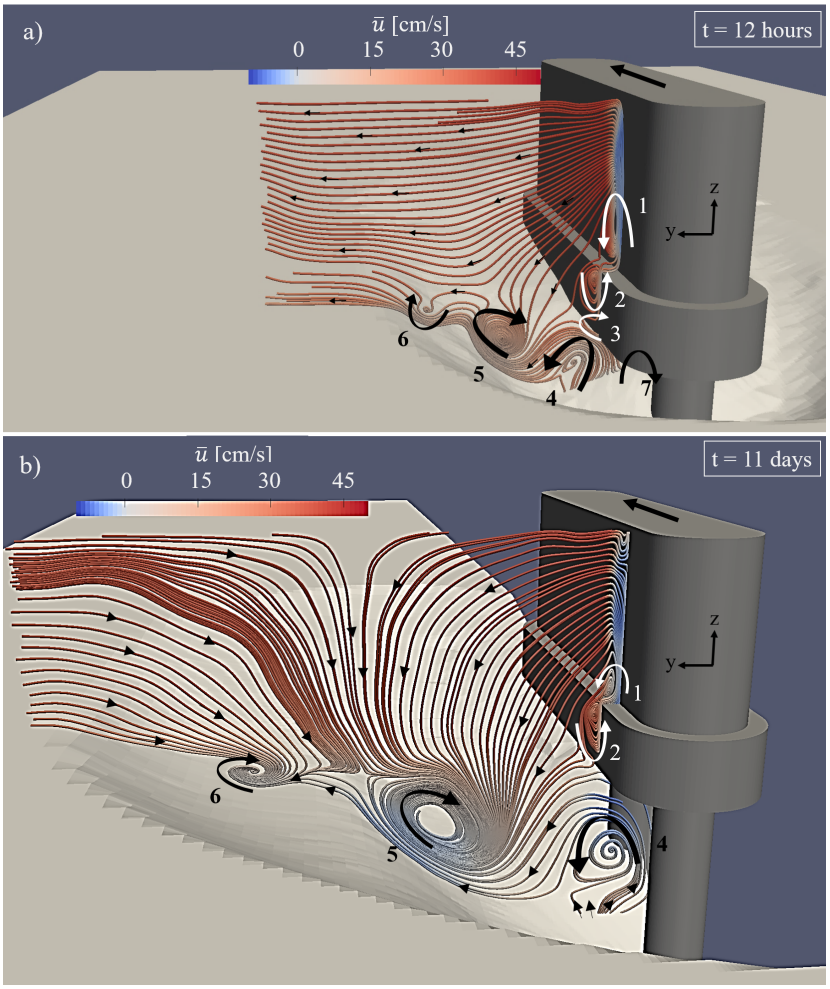

Figure 6.24: Time-averaged streamlines obtained from $\bar{v}$- and $\bar{w}$- velocity components at transverse cross-section $x = 5$ cm for: a) $t = 12$ hours; and b) $t = 11$ days, looking downstream (complex pier case II).

6.3.2.2 Flow features in horizontal planes

Contours of $\bar{u}$-, $\bar{v}$- and $\bar{w}$- velocity components over time development of the scour hole ($t = 0$, 1 hour, 12 hours and 11 days) are shown in Figure 6.25 and Figure 6.26, respectively, for two horizontal planes $z = 6$ and 2 cm. The horizontal plane $z = 6$ cm includes the column, while the plane $z = 2$ cm comprises the pile cap. It is noteworthy to recall that the top level of the pile cap is 2.9 cm above the initial channel bed level.

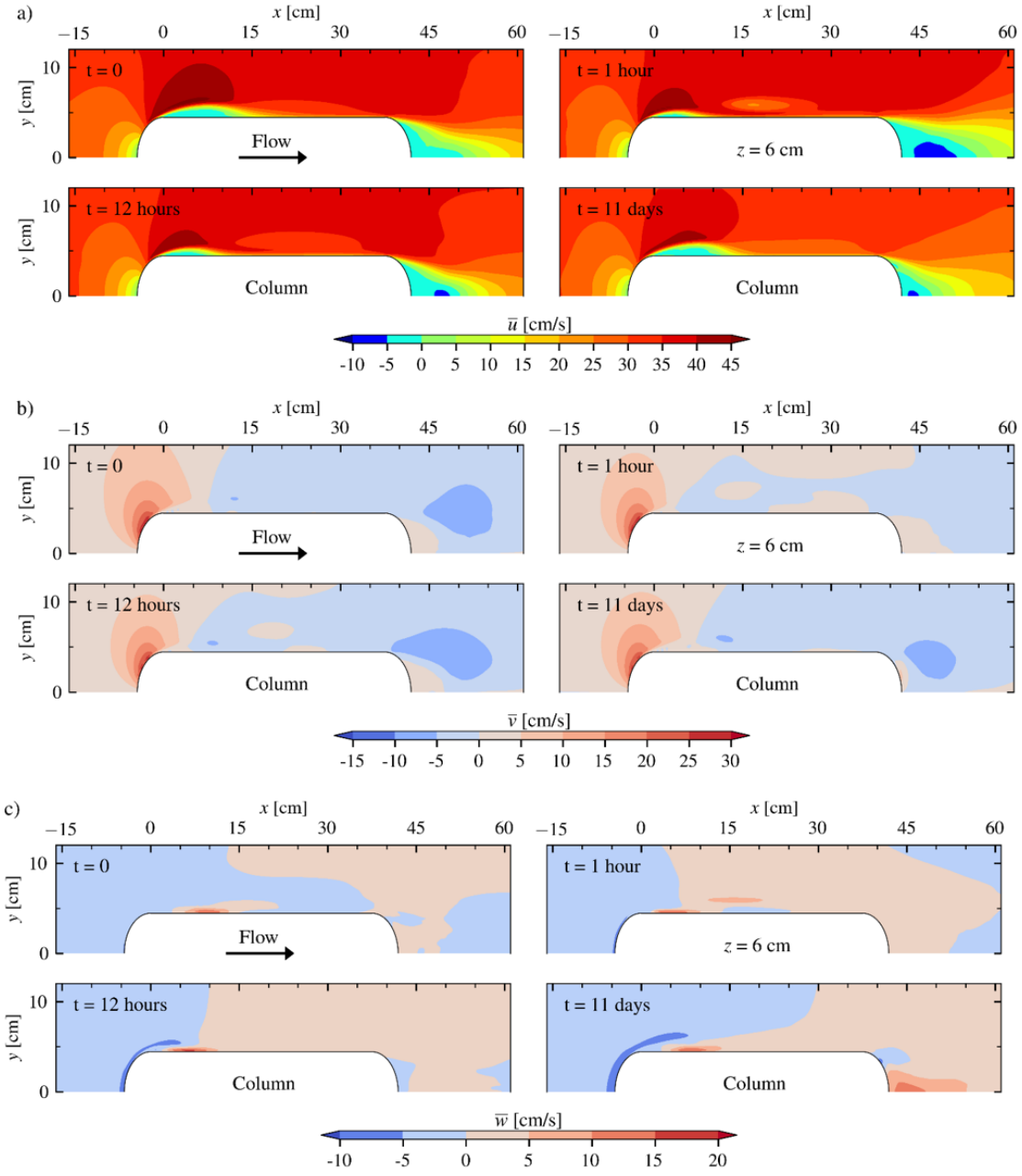

Figure 6.25: Time-averaged velocity contours at horizontal plane z = 6 cm for different stages of the scour hole process (t = 0, 1 hour, 12 hours and 11 days): a) $\bar{u}$-velocity; b) $\bar{v}$-velocity; and c) $\bar{w}$-velocity (complex pier case II).

Overall, $\bar{u}$-velocity values decrease when approaching the column and pile cap. In addition, as shown in Figure 6.25 a) and Figure 6.26 a), no significant change in $\bar{u}$-velocity map is observed at the upstream zone for different stages of the scour hole considered in this study. The $\bar{u}$-velocity increases at the sides of the pier elements (column side at z = 6 cm and the pile cap side at z = 2

cm) and that increase is bigger in extension and higher in magnitude at the upper level (z = 6 cm) than at the lower level (z = 2 cm). Further, the corresponding maximum values (predicted near x = 0) decrease with time development of the scour hole. A reverse flow region (negative $\bar{u}$-velocity values) was predicted along the column side face immediately after x = 0, which indicates the formation of a vertical vortex in that zone, having in attention that high positive $\bar{w}$-velocity values (upward flow) are observed at about x = 5 cm (see Figure 6.25 a) and c)). Concerning the pile cap, no reverse flow was predicted along its lateral sides at z = 2 cm, attributing to the round corners of the pile cap (compared to the sharp edges in the complex pier I) and also to the formation of a horizontal tube vortex (see vortex 2 in Figure 6.23 and Figure 6.24) immediately after the upstream corner edges (x = 0) of the pile cap. Downstream of the pier, the local flow is largely affected by the corresponding bed geometry. In contrast to the flat-bed case (t = 0), there is a deposition dune directly behind the pier at t = 1 hour, which moves downstream with time development of the scour. A comparison between $\bar{u}$-velocity contour maps downstream of the pier (for the considered horizontal planes) indicates that the longitudinal extension of the wake region behind the column and pile cap at t = 0 (flat-bed condition) is larger than at t = 11 days (equilibrium stage of the scour hole process). In fact, the wake region length at t = 11 days (particularly behind the pile cap) is affected by the outflow (upward flow induced) from the region underneath the pile cap.

The $\bar{v}$-velocity maps in Figure 6.25 b) and Figure 6.26 b) indicate that the pier elements deflect the approach flow sideways but, moving downstream, the deflected flow converges back to the symmetry line y = 0 (similar to other pier cases studied here). The maximum absolute values of the $\bar{v}$-velocities were predicted close to the upstream face of the column and pile cap (at a position about 45 degrees from the stagnation point); those maximum values slightly decreased over time development of the scour hole.

Concerning the $\bar{w}$-velocity, Figure 6.25 c) and Figure 6.26 c) show a downward flow region (negative $\bar{w}$-velocity) upstream of the column and pile cap, as well as partially on each side of the mentioned pier elements, at z = 6 and 2 cm. Overall, the maximum values of the downward velocities in front of the pile cap and column increase in extension and in magnitude over time development of the scour hole. Downstream of the pier at t = 0, 1 hour and 12 hours, the $\bar{w}$-velocities are negative in some regions, facilitating deposition of the sediment particles behind the

pier.

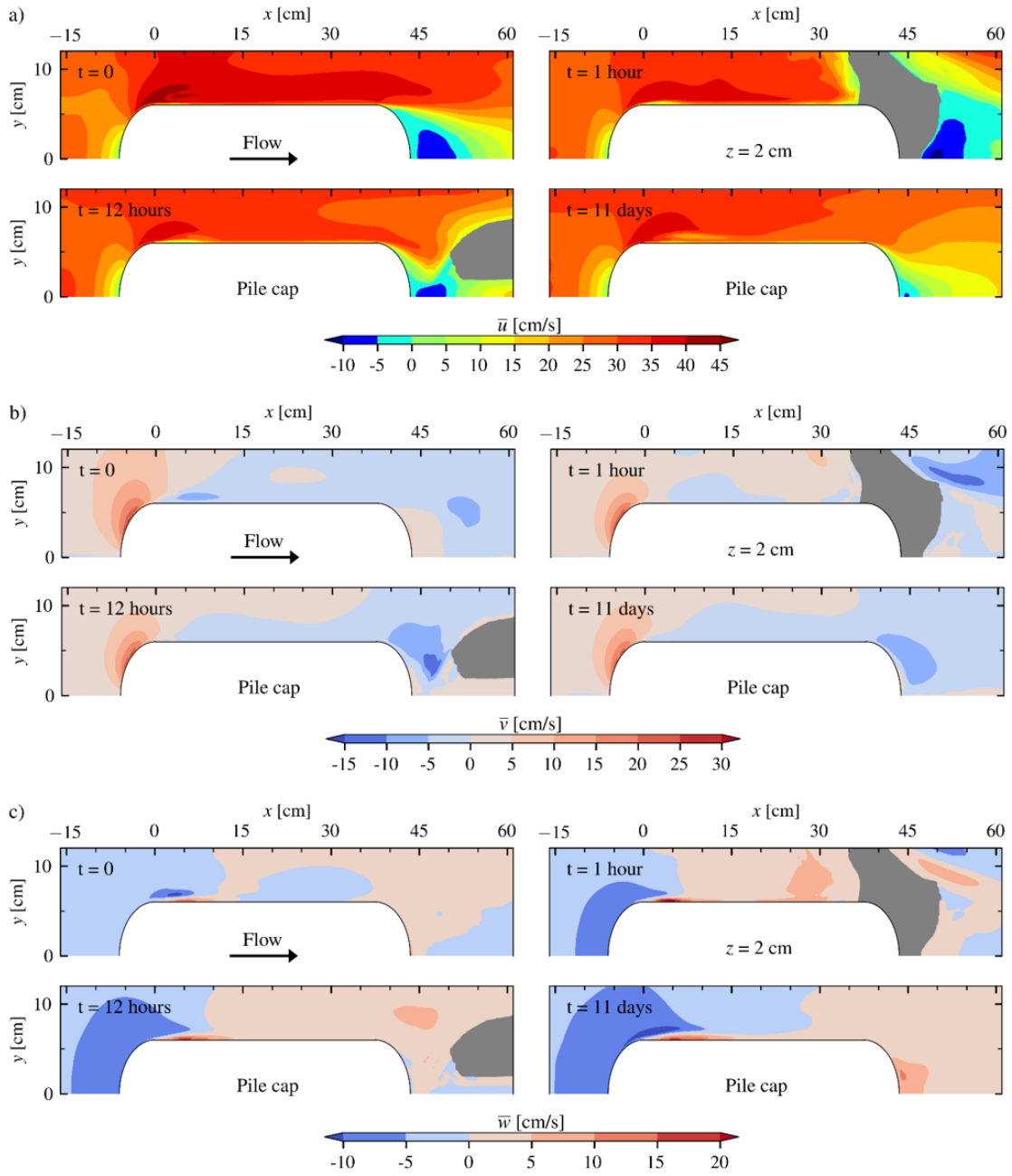

Figure 6.26: Time-averaged velocity contours at horizontal plane $z = 2$ cm for different stages of the scour hole process ($t = 0$, 1 hour, 12 hours and 11 days): a) $\bar{u}$-velocity; b) $\bar{v}$-velocity; and c) $\bar{w}$-velocity (complex pier case II).

Finally, Figure 6.27 represents the time-averaged velocity field at horizontal planes near the bottom of the scour holes developed after $t = 1$ hour, 12 hours and 11 days. One can clearly see that the flow near the bottom of the scour hole weakens, as the scour hole continues to evolve

towards the equilibrium stage at t = 11 days. Concerning the intermediate stages of the scour hole, t = 1 hour and 12 hours, a strong downward flow (negative $\bar{w}$-velocity) is observed at some distances from the upstream pile, while immediately after that (away from the upstream pile), the flow is upward. This flow pattern (change in the vertical velocity direction) represents the main horse-shoe vortex V2 that wraps around the upstream pile and sweeps bed material away from it.

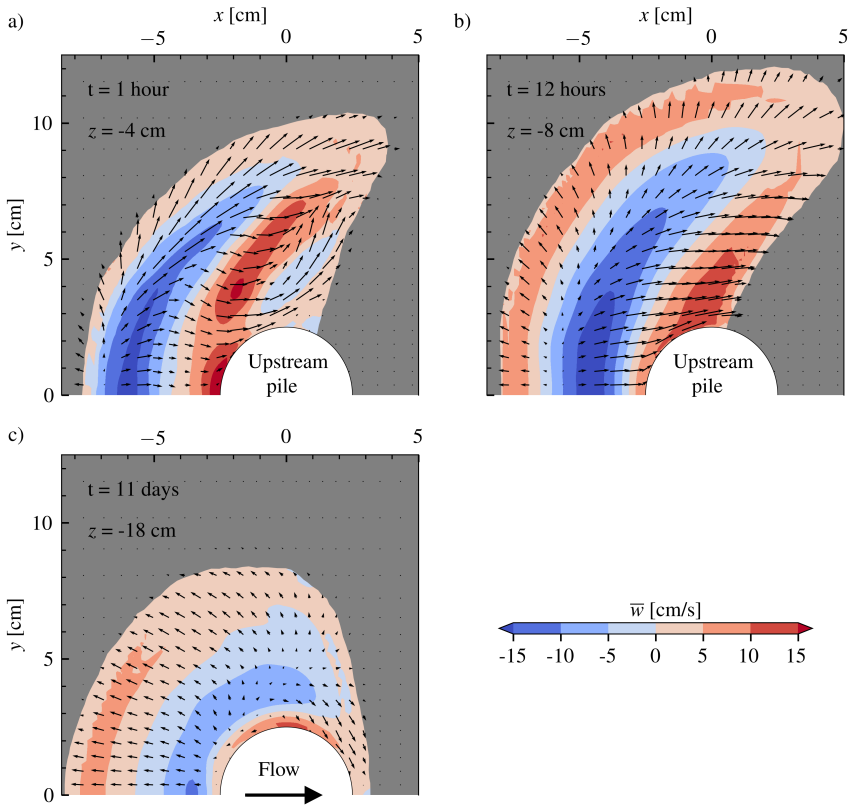

Figure 6.27: Details of the time-averaged flow field inside the scour hole (complex pier case II) at horizontal planes: a) z = -4 cm for t = 1 hour; b) z = -8 cm for t = 12 hours; and c) z = -18 cm for t = 11 days (the corresponding maximum scour depths are about 6, 10 and 20 cm, respectively). Color scale represents the time-averaged vertical velocity and vectors represent longitudinal and transverse components of the velocity (some vectors are hidden for visual clarity).

CHAPTER 7

Final Conclusions and Perspectives

7.1 Final conclusions

The main objective of this study was to propose/develop a numerical model to study the flow behavior around complex bridge piers in a simple, fast and accurate way. In this study, the numerical model was developed in three main steps. The model development was started by considering a simple case in the first step and then required features were added to the model in each new step. The accuracy of the numerical model was also evaluated in each step, by comparing the corresponding numerical results with available reference data. Finally, the numerical model was applied to study the flow features around two different complex bridge piers on the scoured bed. The main characteristics of the numerical model are summarized in the following:

- The numerical model uses a fractional-step method to solve the flow equations set, in which an implicit equation is solved to obtain the pressure values. An iterative method, the so-called successive over-relaxation method, was employed to solve the pressure equation due to its simplicity and efficiency in parallel computing. Parallelization of the numerical calculations was achieved by using Open Multi-Processing (OpenMP) that is based on the idea of using multiple processors on a shared memory computer architecture.

- The spatial discretization of the governing equations was done on a staggered grid system. The CD and QUICK schemes were selected to approximate the convection terms and only

the CD scheme was applied on the remaining spatial terms, having in mind that the convection terms become dominant at high Reynolds numbers. Concerning the convection terms, selecting each of those schemes led to different results (particularly the most important non-dimensional parameters of the flow around a cylinder at low Reynolds numbers). Moreover, further simulations at high Reynolds numbers showed that applying the CD scheme on the convection terms leads to instabilities, observed as spatial point-to-point oscillations upstream of a circular cylinder. Overall, the QUICK scheme was adopted for the bridge pier studies for stability reasons. It is to be noted that, those instabilities were not observed in the flat-channel case when using the CD scheme with a uniform grid system and periodic boundary conditions in the longitudinal direction.

- Concerning the temporal discretization, two semi-implicit schemes (AB-CN and RK-CN) were first considered in the solution in such a way that the convection terms were treated explicitly and diffusion terms implicitly. The stability limit of the RK-CN scheme is higher than that of the AB-CN scheme and therefore, the RK-CN scheme allows using a larger time-step size than the AB-CN scheme. A time-step size study was then performed according to the stability limit of each semi-implicit scheme. For that, 2-D unsteady flow around a square cylinder was predicted by means of AB-CN scheme for Δt = 0.001 s (CFL = 0.4) and by means of RK-CN scheme for Δt = 0.001, 0.002 and 0.0025 s (CFL = 0.4, 0.75 and 1.0). Both schemes led to similar time-averaged results for all the time-step sizes mentioned above. Nevertheless, in terms of the CPU time, the elapsed time for AB-CN calculations with Δt = 0.001 s was found to be nearly equal to the one due to RK-CN calculations with Δt = 0.0025 s. In fact, the number of inner iterations for solving the pressure Poisson equation increased with the time-step size. Therefore, increasing the time-step size (by employing the RK scheme) could not decrease the computational time (CPU time), based on the algorithms used in this study. Moreover, performed simulations showed that the implicit treatment of the diffusion terms uses most of the CPU time at each time step. Although the implicit treatment of the diffusion terms generally eliminates the numerical viscous stability restriction and allows using a larger time-step size than that with the explicit treatment, it might not result in significant gains in this study because of using a relatively coarse mesh near the

wall boundaries. Considering the above explanations, the fully explicit Adams-Bashforth (AB) scheme was finally adopted for the complex pier studies. The explicit scheme also avoids the requirement of the intermediate velocity boundary condition in the solution and that simplifies the calculations procedure.

- Modeling of the turbulent flow features was performed using the Large Eddy Simulation (LES) model. Although the Direct Numerical Simulation (DNS) method is known as the most accurate method for predicting the turbulent flows, the computational cost of the LES is much lower than the DNS. Moreover, the LES model was reported to be able to reasonably reproduce the flow structure around a bridge pier. The numerical results obtained in this study could also confirm the adequacy of the LES model in the bridge pier flow predictions.

- In the LES model, a filtering procedure is used to decompose each flow quantity into large-scale and small-scale components. The large-scales are calculated directly and the effect of the small-scales is modeled by using a subgrid-scale model. In this study, the standard Smagorinsky model with a constant coefficient was used as a subgrid-scale model that is computationally inexpensive compared to a dynamic approach. A sensitivity analysis on the Smagorinsky coefficient value indicated that changing the coefficient from 0.1 to 0.13 did not noticeably change the corresponding results. However, the numerical results were found to depend largely on how the spatial filter width is estimated for the solution, meaning that the grid quality is important for the present numerical model (LES model) since the spatial filter width is obtained based on the grid cell size.

- Accurate LES results require a very fine mesh near the wall boundaries, resulting in a high computational cost for the LES model. In order to overcome this issue, a wall model was applied at the near-wall region; by that, the number of computational grid cells was reduced and consequently, the numerical simulations were performed in a shorter time compared to the sole use of LES. For the bridge pier problems, the wall model enables to consider the roughness effect in order to estimate the wall friction velocity. The corresponding bed shear stress results, obtained in this study, were in fairly good agreement with the experimental ones for a single bridge pier on the eroded bed. Moreover, by using the wall model, most of the known flow structures around the bridge piers (namely near the wall boundaries)

could be properly predicted. Nevertheless, for a flat-bed case, a single stretched vortex was predicted upstream of the complex pier near the bed, while a more complicated flow structure was expected to be formed in that region. That shall be due to the corresponding grid cell size. In fact, the vertical size of the horse-shoe vortex system formed for the flat-bed condition is so small and it requires a more clustered grid in the zone near the bed (probably without using the wall model) to fully resolve the corresponding small dimension of the flow vortices. With the time development of the scour hole process, the size of those vortices increases and thus, the numerical model could predict several vortices upstream of the complex pier inside the scour hole.

- The numerical model uses a porosity method, the so-called FAVOR method, for the definition of the pier and bed geometries. This method requires a structured grid with orthogonal grid lines, which its generation is easier compared to a body-fitted grid. In this method, the position of the grid cell vertices with respect to the flow obstacles is determined in order to incorporate the geometry effects into the governing equations. The use of this method makes modeling of any complex geometry simple and fast; however, the method is affected by the resolution of the computational grid. Overall, the results presented in the numerical model validation section (5.3) could prove the adequacy and accuracy of the method.

Concerning the application of the numerical model, this study presented results beyond the background knowledge available for the studied complex bridge piers. Overall, the present numerical model enabled to characterize the most relevant flow features around the complex piers as follows:

- For the complex pier case I (column and pile cap with sharp corners and a pile group with 2 rows of 4 round piles) at the equilibrium scour hole, the column deflected the approaching flow vertically and sideways. A vortical flow (including two vortices with opposite circulation directions) was formed immediately after the upstream side edges of the column. Downstream of the vortical flow, a horizontal tube vortex was created on top of the pile cap surface along the column side. Moreover, the downward flow in front of the column interacted with the pile cap, resulting in a small vortex being formed above the pile cap. The pile cap also diverted the approaching flow in the vertical direction and around the pile cap sides.

A reversal flow zone occurred immediately after the lower upstream edge of the pile cap. In addition, the flow was separated at the upstream side edges of the pile cap and a small vortex was formed immediately after those edges. Due to the formation of the vortical flow along the column sides, the incoming flow directly above the pile cap was diverted towards the pile cap side faces, forming a horizontal tube vortex along the pile cap sides immediately after the small vortex mentioned above. Below the pile cap, although the incoming flow was largely modified by the upstream piles, the flow was also separated at the piles surface and created a reverse flow region behind the piles with variable sizes. The flow structure in the pile group zone was more complex than at the outer side zones as many vortices were predicted in the piles' zone. Further, the horse-shoe vortex system was numerically predicted in front and also at the lateral sides of the pile group, inside the scour hole. Downstream of the complex pier, a wake flow region was observed behind the column. Moreover, outflow from the pile group zone interacted with the flow above the pile cap, creating two vortices (rotating in the opposite directions) behind the pile cap. Finally, the peak values of the mean velocity components and of the turbulence intensities were predicted to occur in regions close to the complex pier elements, where no experimental results are available due to measuring instrument's limitations. This demonstrates the potential advantage of using a numerical tool (particularly the present numerical model) to investigate the flow field around the complex pier elements.

- For the complex pier case II, column and pile cap with round corners and a pile group with a single row of four piles, the approaching flow was vertically deflected in front of the column. The corresponding deflection point was observed at about z = 15 cm for the flat-bed condition and that position slightly moved downward (at about z = 14 cm) for the equilibrium stage of the scour hole process. A small vortex was predicted in front of the column on top of the pile cap surface, in which its vertical size decreased with the time development of the scour hole. In front of the pile cap, the flow pointed downward for the eroded beds. At the equilibrium stage of the scour hole, compared to the pier case I, the flow was not separated at the lower upstream edge of the pile cap. That is attributed to the geometry and position of the pile cap with respect to the initial channel bed level. In

fact, with the development of the scour hole, the flow was obstructed by the upstream pile and partially deflected vertically. At the intermediate stages of the scour hole development process, the upward flow in front of the upstream pile interacted with the pile cap bottom surface and created a reversal flow immediately after the lower upstream edge of the pile cap; while at the equilibrium stage of the scour hole, the upward flow in front of the upstream pile was not strong enough to form that reversal flow. The horse-shoe vortex system, consisting of several necklace-type vortices, was predicted inside the scour hole. The corresponding sizes and number of vortices increased with the scour depth. Along the column sides, a vortical flow was predicted after the upstream face of the column, while no reversal flow was predicted along the pile cap sides. This is attributed to the round nose of the pile cap, in contrast to the sharp edges of the pier case I, which did not allow the small separation zone to be formed along the pile cap sides. Below the pile cap position, different flow structures were predicted behind the piles. When compared to the pier case I, it can be concluded that the flow structure behind the piles is largely affected by the bed geometry, pile arrangement and pile cap position and hence, the corresponding flow pattern may change from one case to another. Downstream of the pier, a complex flow structure (completely different from that for a single pier) was predicted, as many vortices with different directions were observed in that zone. Moreover, the numerical results showed that the corresponding flow patterns change over the time development of the scour hole. At the equilibrium stage of the scour hole, compared to the pier case I, a reversal flow was predicted downstream of the pier close to the scoured bed surface, which was a consequence of the small distance between the lower downstream edge of the pile cap and the bed surface. Finally, according to the streamline patterns in the vertical symmetry plane, the longitudinal extensions of the reverse flow regions behind the column and the pile cap were smaller at the equilibrium stage of the scour hole than the corresponding ones at the beginning of the erosion process.

7.2 Perspectives for future works

The obtained numerical results are encouraging, and enable some recommendations regarding the model improvements and developments as follows:

- The present numerical model solves the governing equations within a single mesh-block with orthogonal grid lines. When a bluff body (e.g., bed layer) is immersed into the model domain, there are some unnecessary cells, which completely lie inside the body and only occupy the memory. In order to avoid those cells from the modeling, improvement of the numerical model to use multiple mesh-blocks is suggested.

- In this study, the top domain boundary for the bridge pier cases was modeled by using the rigid-lid approach, because the free surface changes were considered to be small in those cases. The numerical model would be applicable for broader cases (e.g., tidal flows) by employing a proper method to estimate the water surface changes. A simple method that is based on the concept of the fractional volume of fluid (VOF) is recommended.

- The present numerical model solves the space-filtered Navier-Stokes and continuity equations and provides details of the flow field around bridge piers with complex geometries on the eroded (but fixed) bed. This work was considered as a basis for a future broader analysis of the scour hole around complex bridge piers. Therefore, a sediment transport model can be implemented into the numerical model to predict the local pier scour in the following studies.

- The present numerical model uses OpenMP for parallel computing, which enables employing only all processors available on a single node/computer (this study: maximum 16 processors). It is clear that modeling of the local scour process requires more computational resources. Therefore, in order to make it feasible, the hybrid MPI+OpenMP is suggested for the parallelization of the computations. In this case, the model domain is subdivided into several sub-domains, each of it can be assigned to a node/computer by MPI and then, OpenMP can be used inside of each node/computer.

Bibliography

Alemi, M., & Maia, R. (2017). A comparative study between two numerical solutions of the Navier-Stokes equations. *Journal of Computational and Applied Research in Mechanical Engineering*, *6*(2), 1–12.

Alemi, M., & Maia, R. (2018). Numerical simulation of the flow and local scour process around single and complex bridge piers. *International Journal of Civil Engineering*, *16*, 475–487.

Ataie-Ashtiani, B., & Aslani-Kordkandi, A. (2012). Flow field around side-by-side piers with and without a scour hole. *European Journal of Mechanics, B/Fluids*, *36*, 152–166.

Ataie-Ashtiani, B., & Aslani-Kordkandi, A. (2013). Flow field around single and tandem piers. *Flow Turbulence Combustion*, *90*, 471–490.

Ataie-Ashtiani, B., Baratian-Ghorghi, Z., & Beheshti, A. A. (2010). Experimental investigation of clear-water local scour of compound piers. *Journal of Hydraulic Engineering*, *136*(6), 343–351.

Balaras, E. (2004). Modeling complex boundaries using an external force field on fixed Cartesian grids in large-eddy simulations. *Computers & Fluids*, *33*, 375–404.

Baykal, C., Sumer, B. M., Fuhrman, D. R., Jacobsen, N. G., & Fredsøe, J. (2015). Numerical investigation of flow and scour around a vertical circular cylinder. *Philosophical Transactions of the Royal Society A: Mathematical, Physical and Engineering Sciences*, *373*(2033).

Bayón-Barrachina, A., Valero, D., Vallès-Morán, F., & López-Jiménez, P. A. (2014). Comparison of CFD models for multiphase flow evolution in bridge scour processes. In *5th International Junior Researcher and Engineer Workshop on Hydraulic Structures*, August, (pp. 28–30). Belgium.

Bearman, P. W., & Obasaju, E. D. (1982). An experimental study of pressure fluctuations on fixed and oscillating square-section cylinders. *Journal of Fluid Mechanics*, *119*, 297–321.

Beaudan, P., & Moin, P. (1994). *Numerical experiments on the flow past a circular cylinder at sub-critical Reynolds number*. Report No. TF-62, Stanford University.

Beheshti, A. A., & Ataie-Ashtiani, B. (2010). Experimental study of three-dimensional flow field around a complex bridge pier. *Journal of Engineering Mechanics*, *136*(2), 143–154.

Beheshti, A. A., & Ataie-Ashtiani, B. (2016). Scour hole influence on turbulent flow field around complex bridge piers. *Flow, Turbulence and Combustion*, *97*(2), 451–474.

Biringen, S., & Chow, C.-Y. (2011). *An introduction to computational fluid mechanics by example*. John Wiley & Sons.

Breuer, M. (1998). Large eddy simulation of the subcritical flow past a circular cylinder: Numerical and modeling aspects. *International Journal for Numerical Methods in Fluids*, *28*, 1281–1302.

Breuer, M., Jovicic, N., & Mazaev, K. (2003). Comparison of DES, RANS and LES for the separated flow around a flat plate at high incidence. *International Journal for Numerical Methods in Fluids*, *41*(4), 357–388.

Breuer, M., Peller, N., Rapp, C., & Manhart, M. (2009). Flow over periodic hills - numerical and experimental study in a wide range of Reynolds numbers. *Computers and Fluids*, *38*(2), 433–457.

Cabot, W., & Moin, P. (2000). Approximate wall boundary conditions in the large-eddy simulation of high Reynolds number flow. *Flow, Turbulence and Combustion*, *63*, 269–291.

Catalano, P., Wang, M., Iaccarino, G., & Moin, P. (2003). Numerical simulation of the flow around a circular cylinder at high Reynolds numbers. *International Journal of Heat and Fluid Flow*, *24*, 463–469.

Chen, Q., Qi, M., Zhong, Q., & Li, D. (2017). Experimental study on the multimodal dynamics of the turbulent horseshoe vortex system around a circular cylinder. *Physics of Fluids*, *29*(1).

Chen, Z. (2011). *Wall modeling for implicit Large-Eddy Simulation*. Ph.D. thesis, Technische Universität München.

Choi, H., & Moin, P. (1994). Effects of the computational time step on numerical solutions of turbulent flow. *Journal of Computational Physics*, *113*, 1–4.

Coussement, A., Gicquel, O., & Degrez, G. (2012). Large eddy simulation of a pulsed jet in cross-flow. *Journal of Fluid Mechanics*, *695*, 1–34.

Dargahi, B. (1989). The turbulent flow field around a circular cylinder. *Journal of Experiments in Fluids*, *8*, 1–12.

Diab, R. (2011). *Experimental investigation on scouring around piers of different shape and alignment in gravel*. Ph.D. thesis, Darmstadt University of Technology.

Durão, D. F. G., Heitor, M. V., & Pereira, J. C. F. (1988). Measurements of turbulent and periodic flows around a square cross-section cylinder. *Experiments in Fluids*, *6*, 298–304.

Einian, M. (2012). *Large Eddy Simulation of flow around a finite square cylinder*. Ph.D. thesis, University of Saskatchewan, Canada.

Graf, W. H., & Istiarto, I. (2002). Flow pattern in the scour hole around a cylinder. *Journal of Hydraulic Research*, *40*(1), 13–20.

Griebel, M., Dornseifer, T., & Neunhoeffer, T. (1998). *Numerical simulation in fluid dynamics: A practical introduction*. Society for Industrial and Applied Mathematics.

Hasan, M. A. Z. (1989). The near wake structure of a square cylinder. *International Journal of Heat and Fluid Flow*, *10*(4), 339–348.

Hines, J. (2008). *A comparative study of the SIMPLE and fractional step time integration methods for transient incompressible flows*. Ph.D. thesis, University of Waterloo, Canada.

Hinsberg, N. P. V. (2004). *The visualisation of the unsteady separated wake flow around bluff-body cylinders (with rectangular cross-section) by means of Particle Image Velocimetry and Proper Orthogonal Decomposition*. Master thesis, Delft University of Technology.

Hirt, C. W., & Sicilian, J. M. (1985). A porosity technique for the definition of obstacles in rectangular cell meshes. In *4th International Conference on Numerical Ship Hydrodynamics*. Washington, DC.

Khosronejad, A., Kang, S., & Sotiropoulos, F. (2012). Experimental and computational investigation of local scour around bridge piers. *Advances in Water Resources*, *37*, 73–85.

Kim, J., & Moin, P. (1985). Application of a fractional-step method to incompressible Navier-Stokes equations. *Journal of Computational Physics*, *59*, 308–323.

Kim, S., Wilson, P. A., & Chen, Z.-M. (2015). Effect of turbulence modelling on 3-D LES of transitional flow behind a circular cylinder. *Ocean Engineering*, *100*, 19–25.

Kirkil, G., Constantinescu, S. G., & Ettema, R. (2008). Coherent structures in the flow field around a circular cylinder with scour hole. *Journal of Hydraulic Engineering*, *134*(5), 572–587.

Kirkil, G., Constantinescu, S. G., & Ettema, R. (2009). Detached Eddy Simulation investigation of turbulence at a circular pier with scour hole. *Journal of Hydraulic Engineering*, *135*(11), 888–901.

Kravchenko, A. G., & Moin, P. (2000). Numerical studies of flow over a circular cylinder at Re = 3900. *Journal of Physics of Fluids*, *12*(2), 403–417.

Kumar, A., & Kothyari, U. C. (2012). Three-Dimensional flow characteristics within the scour hole around circular uniform and compound Piers. *Journal of Hydraulic Engineering*, *138*, 420–429.

Le, H., & Moin, P. (1991). An improvement of fractional step methods for the incompressible Navier-Stokes equations. *Journal of Computational Physics*, *92*, 369–379.

Leonard, B. P. (1979). A stable and accurate convective modelling procedure based on quadratic upstream interpolation. *Computer Methods in Applied Mechanics and Engineering*, *19*(1), 59–98.

Link, O., Gobert, C., Manhardt, M., & Zanke, U. (2008). Effect of the horseshoe vortex system on the geometry of a developing scour hole at a cylinder. In *Fourth International Conference on Scour and Erosion*, (pp. 162–168).

Lourenco, L., & Shih, C. (1993). Characteristics of the plane turbulent near wake of a circular cylinder, a particle image velocimetry study. *(Beaudan and Moin (1994))*.

Lyn, D. A., Einav, S., Rodi, W., & Park, J.-H. (1995). A laser-Doppler velocimetry study of ensemble-averaged characteristics of the turbulent near wake of a square cylinder. *Journal of Fluid Mechanics*, *304*, 285–319.

Lysenko, D. A., Ertesvag, I. S., & Rian, K. E. (2012). Large-Eddy Simulation of the flow over a circular cylinder at Reynolds number 3900 using the OpenFOAM toolbox. *Flow Turbulence Combust*, *89*, 491–518.

Mahesh, K., Constantinescu, G., & Moin, P. (2004). A numerical method for large-eddy simulation in complex geometries. *Journal of Computational Physics*, *197*(1), 215–240.

Majander, P., & Siikonen, T. (2002). A comparison of time integration methods in an unsteady low-Reynolds-number flow. *International Journal for Numerical Methods in Fluids*, *39*(5), 361–390.

Mani, A., Moin, P., & Wang, M. (2009). Computational study of optical distortions by separated shear layers and turbulent wakes. *Journal of Fluid Mechanics*, *625*, 273–298.

Melville, B. W., & Coleman, S. E. (2000). *Bridge scour*. Water Resources Publications, LLC, Colorado, USA.

Melville, B. W., & Raudkivi, A. J. (1977). Flow characteristics in local scour at bridge piers. *Journal of Hydraulic Research*, *15*(4), 373–380.

Meyer, M., Hickel, S., & Adams, N. A. (2010). Assessment of Implicit Large-Eddy Simulation with a Conservative Immersed Interface Method for turbulent cylinder flow. *International Journal of Heat and Fluid Flow*, *31*, 368–377.

Minguez, M., Brun, C., Pasquetti, R., & Serre, E. (2011). Experimental and high-order LES analysis of the flow in near-wall region of a square cylinder. *International Journal of Heat and Fluid Flow*, *32*(3), 558–566.

Mittal, R., & Balachandar, S. (1996). Direct numerical simulation of flow past elliptic cylinders. *Journal of Computational Physics*, *124*, 351–367.

Moin, P. (1995). Large-Eddy Simulation of Backward-Facing step flow with application to coaxial jet combustors. Tech. rep., Stanford University.

Moreno, M. (2016). *Experimental study of local scour around complex bridge piers*. Ph.D. thesis, University of Porto, Portugal.

Moreno, M., Maia, R., & Couto, L. (2016). Prediction of equilibrium local scour depth at complex bridge piers. *Journal of Hydraulic Engineering*, *142*(11), 04016045.

Moser, R. D., Kim, J., & Mansour, N. N. (1999). Direct numerical simulation of turbulent channel flow up to Re=590. *Physics of Fluids*, *11*(4), 943–945.

Mueller, A. A. (2012). *Large Eddy Simulation of cross-flow around a square rod at incidence with application to tonal noise prediction*. Ph.D. thesis, University of Twente, Netherlands.

Muzzammil, M., & Gangadhariah, T. (2003). The mean characteristics of horseshoe vortex at a cylindrical pier. *Journal of Hydraulic Research*, *41*(3), 285–297.

Neumann, L. E., Šimůnek, J., & Cook, F. J. (2011). Implementation of quadratic upstream interpolation schemes for solute transport into HYDRUS-1D. *Environmental Modelling and Software*, *26*(11), 1298–1308.

Norberg, C. (1987). *Effects of Reynolds number and a low-intensity freestream turbulence on the flow around a circular cylinder*. Ph.D. thesis, Chalmers University of Technology, Gothenburg, Sweden.

Ong, L., & Wallace, J. (1996). The velocity field of the turbulent very near wake of a circular cylinder. *Experiments in Fluids*, *20*, 441–453.

Paone, T., Ferreira, R. M. L., Cardoso, A. H., & Armenio, V. (2016). Numerical investigation on the effect of suspended sediment load on flow field around a cylinder. In *Proceedings of the 13th International Symposium on River Sedimentation*, (pp. 1329–1335). Stuttgart, Germany.

Parnaudeau, P., Carlier, J., Heitz, D., & Lamballais, E. (2008). Experimental and numerical studies of the flow over a circular cylinder at Reynolds number 3900. *Jornal of Physics of Fluids*, *20*(8).

Piomelli, U., & Balaras, E. (2002). Wall-layer models for large-eddy simulations. *Annual Review of Fluid Mechanics*, *34*(1), 349–374.

Pope, S. B. (2004). Ten questions concerning the large-eddy simulation. *New Journal of Physics*, *6*.

Posa, A., & Balaras, E. (2014). Model-based near-wall reconstructions for immersed-boundary methods. *Theoretical and Computational Fluid Dynamics*, *28*(4), 473–483.

Pournazeri, S., Li, S. S., & Haghighat, F. (2014). Efficient non-hydrostatic modelling of flow and bed shear stress in a pier scour hole. *Canadian Journal of Civil Engineering*, *41*, 450–460.

Radice, A., & Tran, C. K. (2012). Study of sediment motion in scour hole of a circular pier. *Journal of Hydraulic Research*, *50*(1), 44–51.

Ramos, P. X., Bento, A. M., Maia, R., & Pêgo, J. P. (2016). Characterization of the scour cavity evolution around a complex bridge pier. *Journal of Applied Water Engineering and Research*, *4*(2), 128–137.

Rapp, C., & Manhart, M. (2011). Flow over periodic hills: An experimental study. *Experiments in Fluids*, *51*(1), 247–269.

Raudkivi, A. J. (1986). Functional trends of scour at bridge piers. *Journal of Hydraulic Engineering*, *112*, 1–13.

Rodi, W. (1997). Comparison of LES and RANS calculations of the flow around bluff bodies. *Journal of Wind Engineering*, *69-71*, 55–75.

Roosenboom, E. W. M. (2005). *Experimental analysis of the flow around a cylinder with a square cross-section*. Master thesis, Delft University of Technology.

Roulund, A., Sumer, B. M., Fredsøe, J., & Michelsen, J. (2005). Numerical and experimental investigation of flow and scour around a circular pile. *Journal of Fluid Mechanics*, *534*, 351–401.

Schindfessel, L., Creëlle, S., & De Mulder, T. (2015). Flow patterns in an open channel confluence with increasingly dominant tributary inflow. *Water (Switzerland)*, *7*(9), 4724–4751.

Sharma, A., & Eswaran, V. (2004). Heat and fluid flow across a square cylinder in the two-dimensional laminar flow regime. *Numerical Heat Transfer, Part A: Applications*, *45*(3), 247–269.

Shields, A. (1936). *Application of similarity principles and turbulence research to bed-load movement*. California Institute of Technology, Pasadena, CA.

Smagorinsky, J. (1963). General circulation experiments with the primitive equations. *Monthly Weather Review*, *91*(3), 99–164 (as cited by Breuer (1998)).

Sohankar, A., Davidson, L., & Norberg, C. (2000). Large Eddy Simulation of flow past a square cylinder: comparison of different subgrid scale models. *Journal of Fluids Engineering*, *122*, 39–47.

Sohankar, A., Norberg, C., & Davidson, L. (1998). Low-Reynolds-number flow around a square cylinder at incidence: Study of blockage, onset of vortex shedding and outlet boundary condition. *International Journal for Numerical Methods in Fluids*, *26*(1371), 39–56.

Stahlmann, A. (2013). *Experimental and numerical modeling of scour at offshore wind turbines*. Ph.D. thesis, Leibniz University of Hanover, Germany.

Sumer, B., & Fredsøe, J. (1997). *Hydrodynamics around cylindrical structures. Advanced Series on Ocean Engineering*. World Scientific.

Tafti, D. (1996). Comparison of some upwind-biased high-order formulations with a second-order scheme for time integration of the incompressible Navier-Stokes equations. *Computers & Fluids*, *25*(7), 647–665.

Tessicini, F., Iaccarino, G., Fatica, M., Wang, M., & Verzicco, R. (2002). Wall modeling for large-eddy simulation using an immersed boundary method. *Center for Turbulence Research, Annual Research Briefs*, (pp. 181–187).

Travin, A., Shur, M., Strelets, M., & Spalart, P. (1999). Detached-Eddy Simulations past a circular cylinder. *Flow Turbulence and Combustion*, *63*, 293–313.

Tremblay, F. (2001). *Direct and large eddy simulation of flow around a circular cylinder at subcritical Reynolds numbers*. Ph.D. thesis, Technische Universität München.

Trias, F. X., Gorobets, A., & Oliva, A. (2015). Turbulent flow around a square cylinder at Reynolds number 22000: A DNS study. *Jornal of Computers and Fluids*, *123*(22), 87–98.

Ünal, U. O., Atlar, M., & Gören, Ö. (2010). Effect of turbulence modelling on the computation of the near-wake flow of a circular cylinder. *Ocean Engineering*, *37*, 387–399.

Unger, J., & Hager, W. H. (2007). Down-flow and horseshoe vortex characteristics of sediment embedded bridge piers. *Experiments in Fluids*, *42*, 1–19.

Wang, M. (1999). LES with wall models for trailing-edge aeroacoustics. *Annual Research Briefs, Center for Turbulence Research*, (pp. 355–364).

Wang, M., & Moin, P. (2002). Dynamic wall modeling for large-eddy simulation of complex turbulent flows. *Journal of Physics of Fluids*, *14*(7), 2043–2051.

Werner, H., & Wengle, H. (1991). Large-Eddy Simulation of turbulent flow over and around a cube in a plate channel. In *8th Symposium on Turbulent Shear Flows*, (pp. 155–168). Springer Berlin Heidelberg.

Zhang, C., Lan, H., Ye, Y., & Estrade, B. D. (2005). Parallel SOR iterative algorithms and performance evaluation on a Linux cluster. In *International Conference on Parallel and Distributed Processing Techniques and Applications, {PDPTA}*, (pp. 263–269). Las Vegas, Nevada, USA.

Zou, L., Lin, Y.-F., & Lam, K. (2008). Large-Eddy Simulation of flow around cylinder arrays at a subcritical Reynolds number. *Journal of Hydrodynamics*, *20*(4), 403–413.

APPENDIX A

This appendix presents details of the flow field around an infinite-length circular cylinder at $Re_D = 4 \times 10^4$, obtained by using the immersed-boundary method, present study.

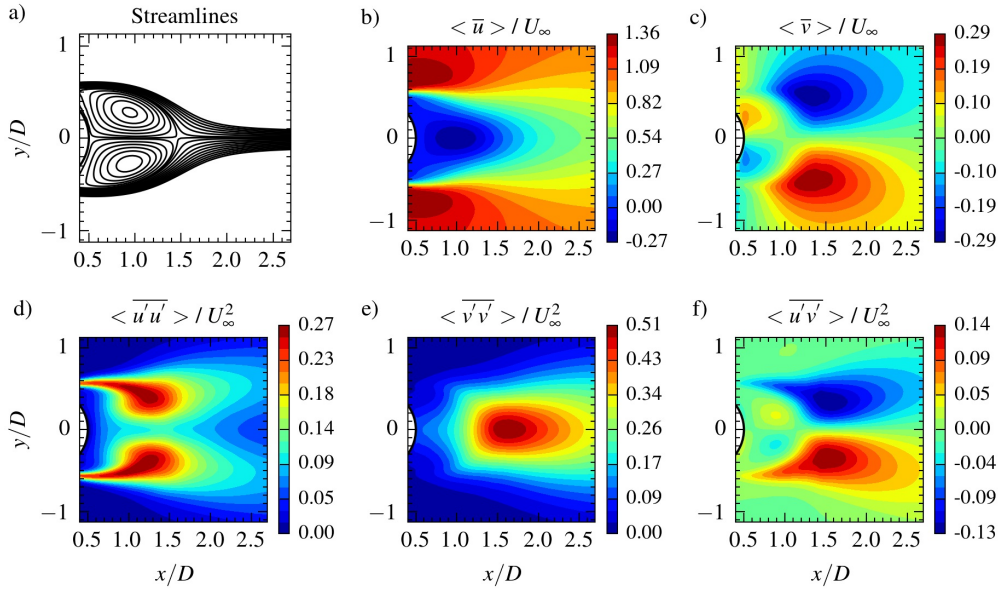

Figure A.1: Time- and vertically- averaged flow features behind an infinite-length circular cylinder at $Re_D = 4 \times 10^4$, immersed-boundary method, present study.

Table A.1: Overview of some numerical and experimental studies on the infinite-length circular cylinder.

Ref.	$\overline{C}_D$	St	$\frac{L_r}{D}$	$\left(\frac{<\bar{u}>}{U_\infty}\right)_{min}$	$\left(\frac{\lvert<\bar{v}>\rvert}{U_\infty}\right)_{max}$	$\left(\frac{<\overline{u'u'}>}{U_\infty^2}\right)_{max}$	$\left(\frac{<\overline{v'v'}>}{U_\infty^2}\right)_{max}$	$\left(\frac{\lvert<\overline{u'v'}>\rvert}{U_\infty^2}\right)_{max}$
1	1.13	0.204	0.95	-0.27	0.29	0.27	0.51	0.14
				(1,0)*	(1.27,±0.5)*	(1.17,±0.43)*	(1.62,0)*	(1.5,±0.35)*
2	1.14	0.19	0.9	-0.25	0.28			0.14
				(0.87,0)*	(1.22,±0.49)*			(1.4,±0.38)*
3	1.19	0.2		-0.26		0.35		0.17
4 *a*	1.17	0.19	0.9			0.26	0.56	0.14
b	1.14	0.2	1.1			0.25	0.53	0.14

1: Present numerical results for Re_D = 40000 (immersed-boundary method); 2: Experimental results of Ünal et al. (2010) for Re_D = 41300; 3: LES model's results presented by Kim et al. (2015) for Re_D = 41300; 4: DES model's results obtained by Travin et al. (1999) for Re_D = 50000 (two numerical grid definitions were used: *a* corresponds to a coarser grid than that for *b*); *: Location (x/D, y/D) of the assessment/measuring point (origin at the cylinder center).

APPENDIX B

This appendix presents four figures on completing Chapter 5.

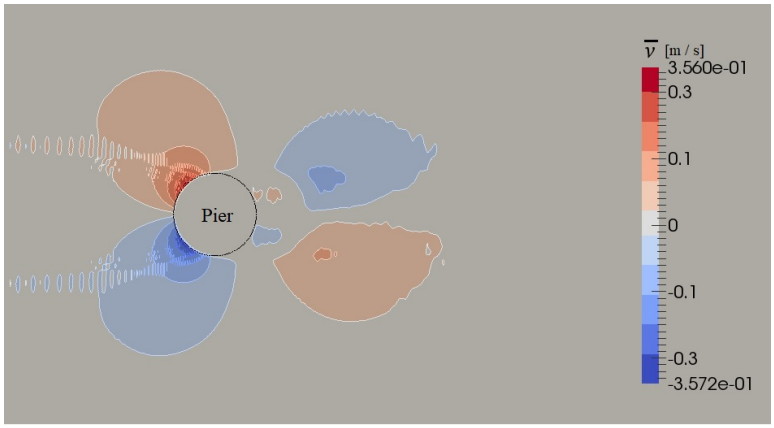

Figure B.1: Visualization of the instabilities upstream of a circular cylinder in a Cartesian grid system for a case when applying the CD scheme on approximation of the convection terms, present study.

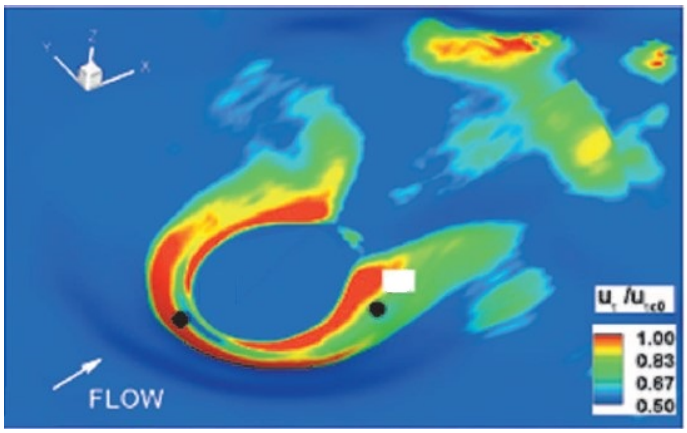

Figure B.2: Distribution of the time-averaged friction velocity, normalized by the critical value for sediment entrainment on the flat-bed (Kirkil et al., 2008).

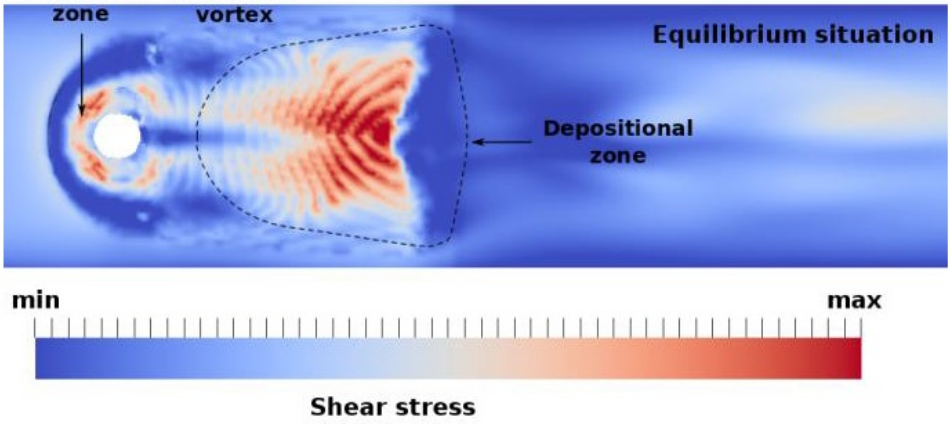

Figure B.3: Time-averaged bed shear stress distribution around a single circular pier (Bayón-Barrachina et al., 2014).

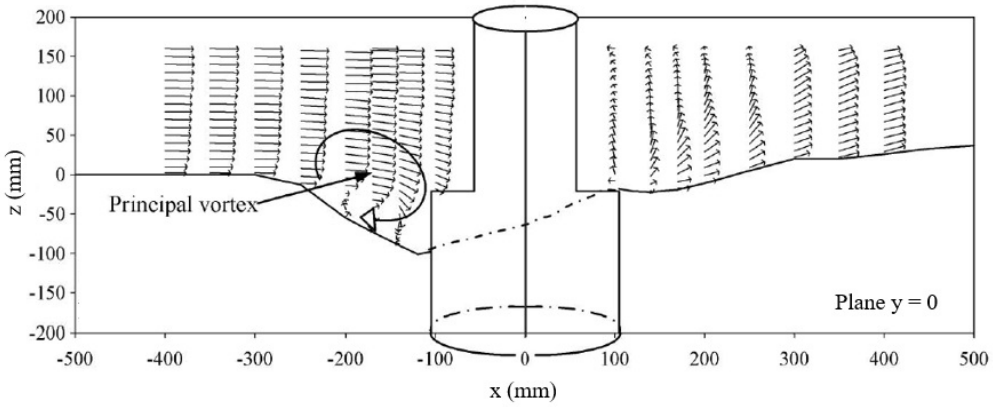

Figure B.4: Velocity vectors at the vertical symmetry plane $y = 0$, compound pier case (Kumar & Kothyari, 2012).

APPENDIX C

This appendix presents computational meshes used in the present study for modeling the complex pier case I and II.

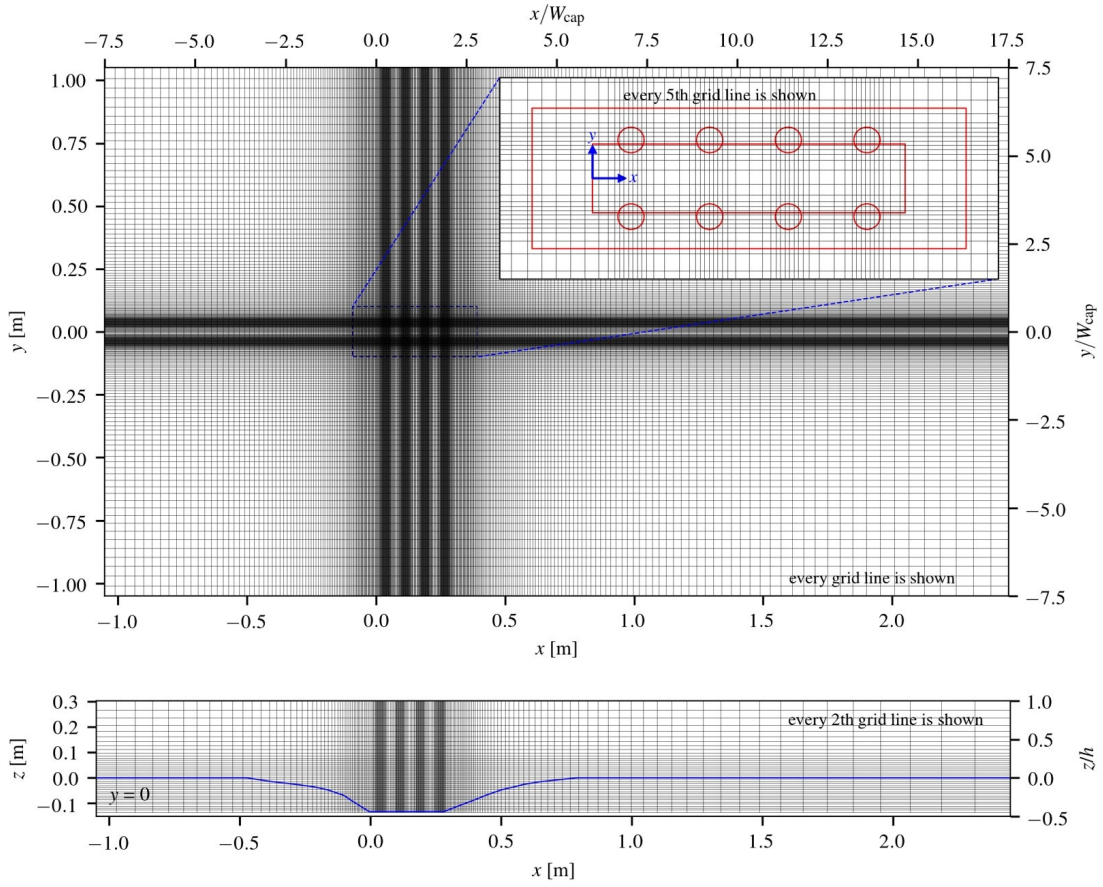

Figure C.1: Computational mesh in a horizontal (top) and a vertical plane (bottom), complex pier case I.

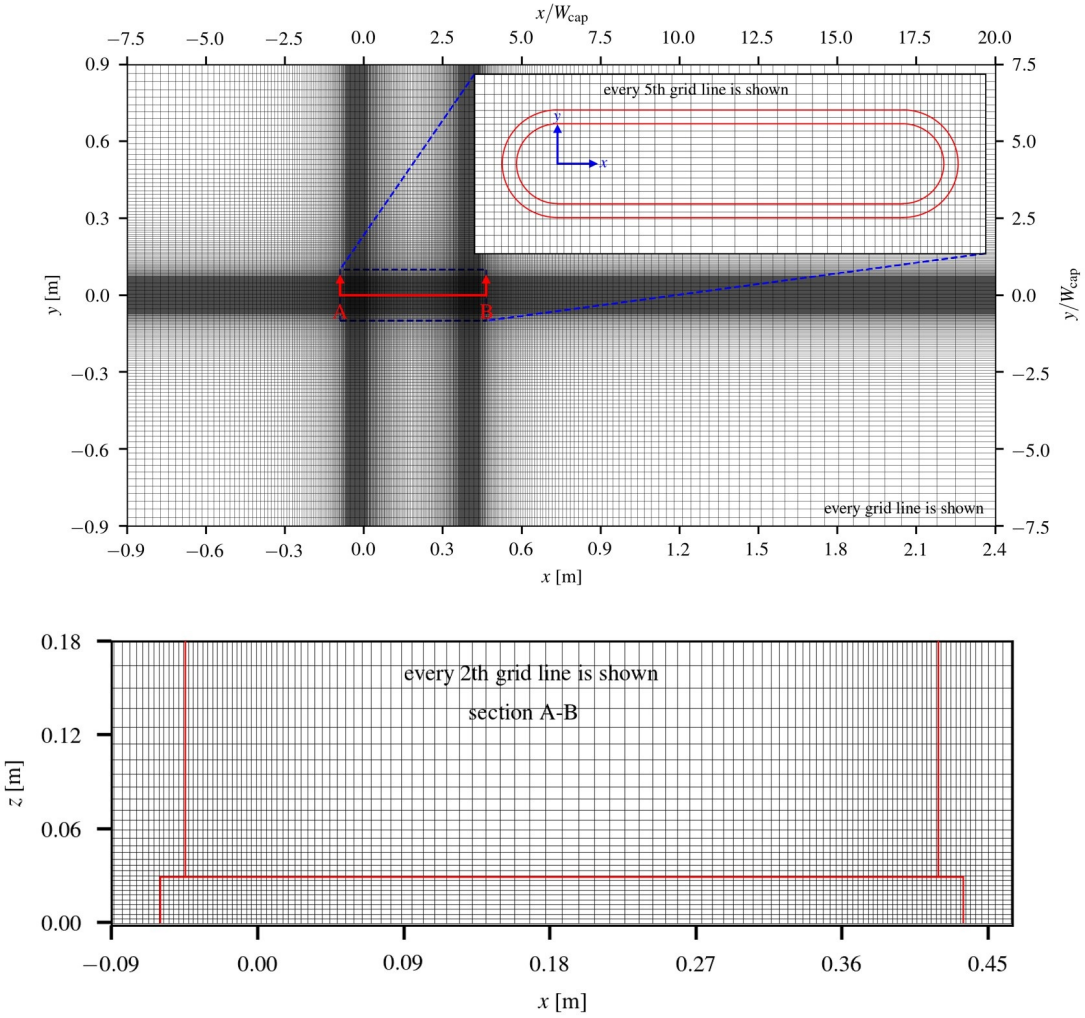

Figure C.2: Computational mesh in a horizontal (top) and a vertical plane (bottom) at the numerical test corresponding to $t = 0$, complex pier case II.

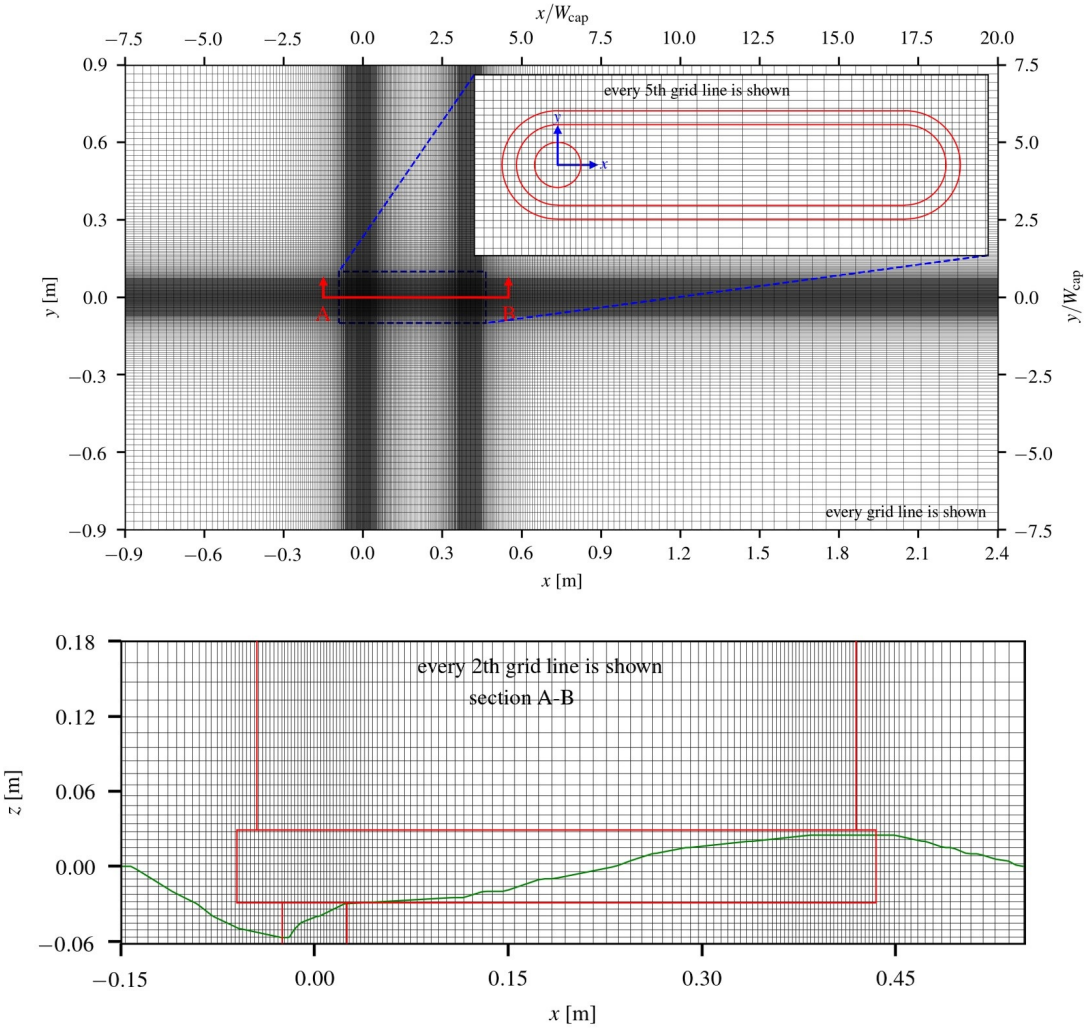

Figure C.3: Computational mesh in a horizontal (top) and a vertical plane (bottom) at the numerical test corresponding to t = 1 hour, complex pier case II (note that only the upstream pile was modeled as the other piles do not interact with the flow at t = 1 hour).

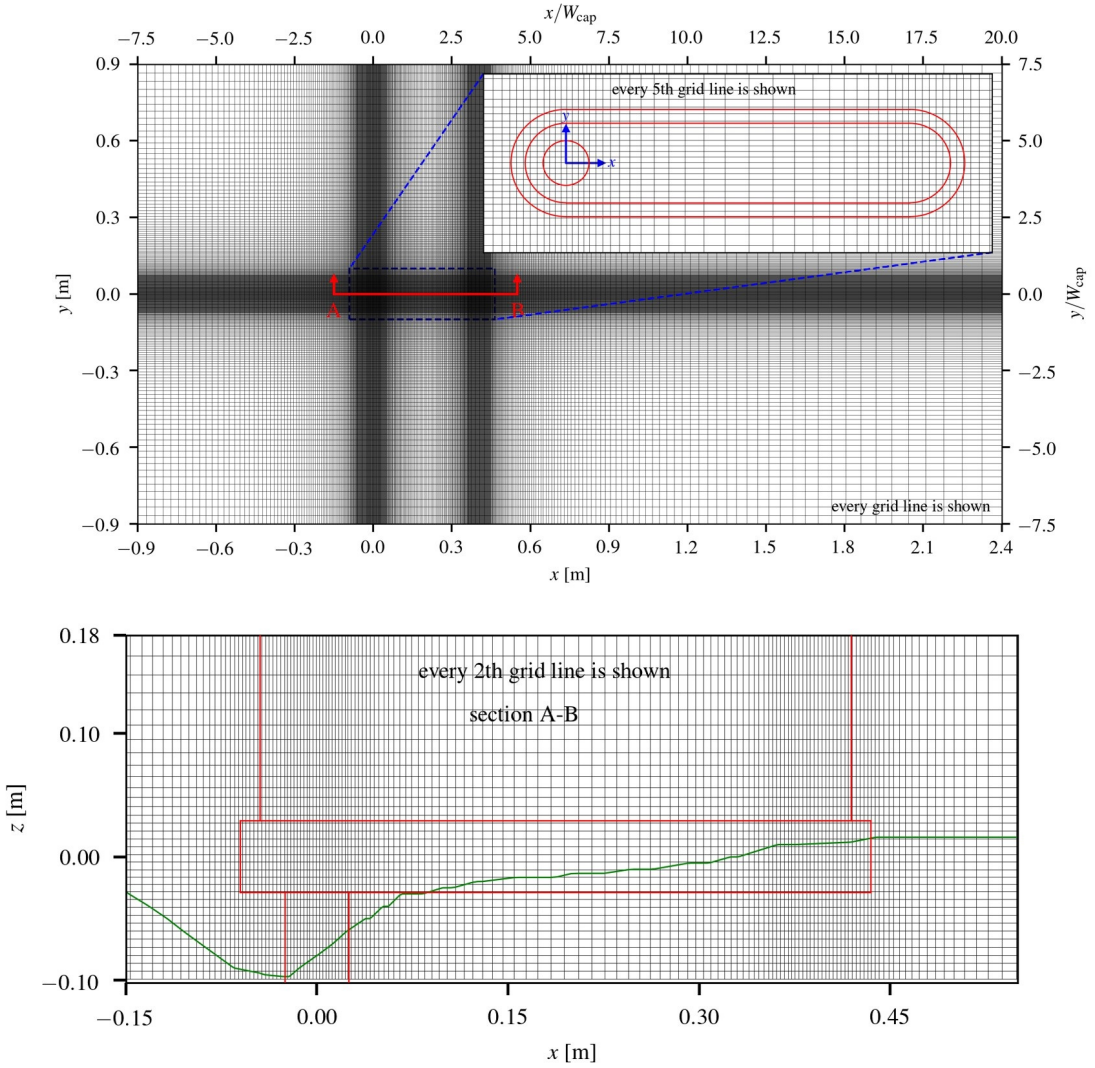

Figure C.4: Computational mesh in a horizontal (top) and a vertical plane (bottom) at the numerical test corresponding to t = 12 hours, complex pier case $\overline{\Pi}$ (note that only the upstream pile was modeled as the other piles do not interact with the flow at t = 12 hours).

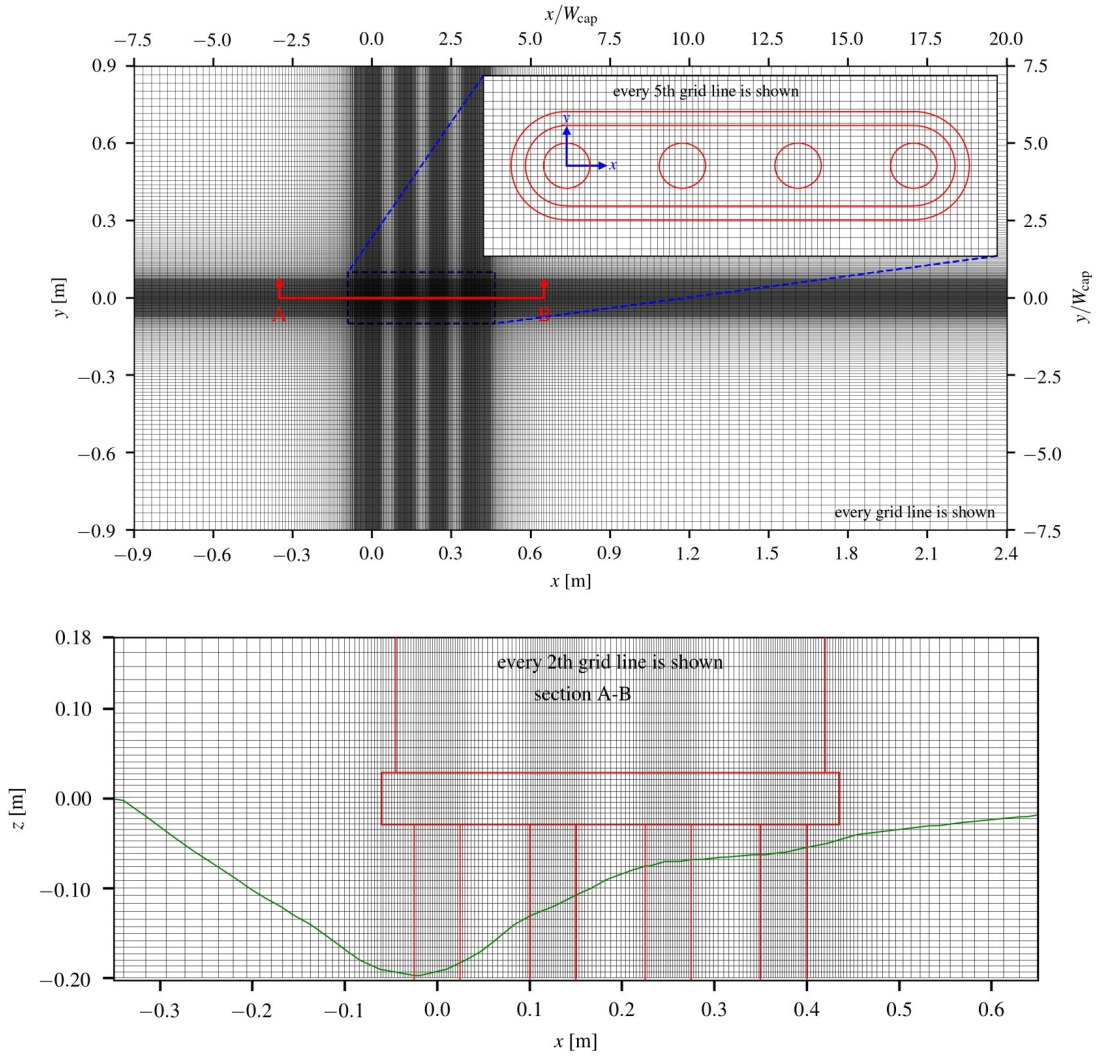

Figure C.5: Computational mesh in a horizontal (top) and a vertical plane (bottom) at the numerical test corresponding to t = 11 days, complex pier case II.